Constructing Contractile Ensembles: How Cells Build Units of Force Generation

By

Aidan Fenix

Dissertation

Submitted to the Faculty of the
Graduate School of Vanderbilt University
in partial fulfillment of the requirements
for the degree of

DOCTOR OF PHILOSOPHY

In

Cell and Developmental Biology

December 15, 2018

Nashville, Tennessee

Approved:

Dylan T. Burnette, Ph.D., Advisor

David M. Miller, Ph.D., Committee Chair

Matthew J. Tyska, Ph.D.

Irina Kaverina, Ph.D.

Jason R. Becker, M.D.

Acknowledgements

First and foremost, I would like to thank my mentor Dr. Dylan T. Burnette. I do not possess the literary prowess to accurately portray the depth of mentoring and training I've received. Undoubtedly, the work presented here would not be possible without the training, guidance, inspiration, and creativity received from Dylan. Being mentored by Dylan for the past 5 years has truly been an honor. Dylan is directly responsible for all the skills in my scientific repertoire. Most notable among the technical skills Dylan has passed on is his knowledge, skill, and creativity in all aspects of microscopy. In a long line of scientists harnessing the power of microscopy, dating back to Van leeuwenhoek and Robert Hooke, Dylan's mentoring has blossomed my own passion for observing biological processes and striving to understand them. In addition to supporting the technical aspect of my training, Dylan has also always pushed me to share my science whenever possible, and supported my career aspirations. This includes supporting numerous conference attendances, and most notably, a two-month training course at the MBL at Wood's Hole. Finally, and in my opinion, most importantly, Dylan has always not merely entertained, but supported and assisted with, often crazy and far-fetched scientific ideas. The ability to freely propose and discuss ideas, and receive positive feedback, at any time of the day (or night), on any topic (related to our work or not), has been the most rewarding aspect of my training, and given me the confidence to be a successful investigator of my own. I hope to be as good a mentor as Dylan has been to me, and his scientific curiosity, passion, and creativity have been, and will continue to be an inspiration to me as I continue on my scientific career. Historically, when a trainee

has reached a new level in their career, their advancement is tied to the prestige of the person who elevates them. I am proud to receive my scientific spurs from Dylan Burnette.

It is a truth universally acknowledged, that a scientist is in want of funding. The wonderful and enlightening experiments which have the potential to increase knowledge and enrich our lives can only be performed from the generous contributions of people and organizations who support the scientific endeavor. I have been extremely fortunate in my short career to be supported financially by my advisor, Vanderbilt University, the American Heart Association, the National Institutes of Health, and the MBL at Wood's Hole. Hopefully, through the work, outreach, teaching, and awareness efforts of scientists around the world, we can secure funding for all those with curiosity and the drive to pursue science.

In addition to my advisor, the entire Burnette lab has made my time at Vanderbilt a truly wonderful experience. Every day I am inspired by lab-mates, who share a passion and curiosity for biological phenomenon. At the beginning, Nilay Taneja was the only other graduate student in the lab, and it was a wonderful, productive time for us both. Nilay's wealth of knowledge on a wide range of subjects and hard-work are a daily inspiration. Later, another graduate student, Abigail Neininger joined the lab, and her personality and background has truly enriched both my work and that of the entire lab. Karen Hyde then joined the lab, and in her short time in the lab I have learned much from her expertise and approach to science and life. I am truly fortunate to have had the opportunity to work with these individuals, who have enriched my life, and who in addition to colleagues, I consider friends.

In addition to the Burnette lab there are many colleagues, peers, departments, cores, individuals, and friends who have supported, inspired, and taught me throughout my graduate career, and were simply a joy to interact with and work with. My work would not be possible without vast contributions from; my thesis committee, the Cell Imaging Shared Resources (CISR) core at Vanderbilt, the Department of Cell and Developmental Biology which has been a fantastic department to be a part of, and the Epithelial Biology Center (EBC). In addition, I have had the fortune of working closely with the Matthew Tyska lab, whom many members I have formed friendships with, and who have been instrumental in aspects of my work (especially for allowing me to "borrow" materials).

In particular, I would also like to extend a special thank you to Dr. Matthew J. Tyska and Dr. Robert (Bob) Coffey who have consistently supported my graduate career. Despite their busy schedules, Matt and Bob have always taken the time to write numerous letters of recommendations, read our manuscripts, or simply discuss interesting science. I am truly fortunate to work closely with such great scientists and people and I be enriched by their knowledge and scientific style.

I would also like to thank those who make the work everyone at Vanderbilt does possible on a day to day basis. These especially include the administrative staff of the Department of Cell and Developmental Biology and the BRET office. Though it seems I only contact them when I have an issue, they are always happy to help and resolve an issue. In addition, often overlooked positions, such as those involved the Vanderbilt Building Services, who among many things, ensure a cleanly and functioning work space.

Last, and certainly not least I would like to thank my family and friends who have supported me throughout my graduate career. My loving parents, John and Kathy Fenix, have been extremely supportive of my career choice, despite the fact that I haven’t always been clear about what I actually do. Hopefully this document is tangible proof I have been somewhat productive for the last 5 years. A constant source of love, support, entertainment, and learning, I hope to be as good a parent as they have been to me. I have also had good luck to live in the same city as my sister, Kelsey Fenix during my graduate career. It has been great to have a constant friend during my studies, and her hard work and success in her own career are a constant source of pride and inspiration. I have also had the fortune to have a core and consistent group of intelligent, hard-working, funny, and enjoyable group of friends throughout my career. I am excited for their bright futures.

Finally, I would like to thank my loving girlfriend, Diana Wanner. I had the fortune of meeting this impressive young woman towards the end of my graduate career. An intelligent, hard-working, and caring individual, she is a constant source of inspiration both inside and outside the lab. Finishing a PhD has certainly been a stressful time, and Diana has been both understanding, supportive, and helpful throughout these trying times. I consider myself extremely fortunate that she will be joining me in Seattle, WA for my post-doc, and I am beyond excited for the adventures we will share together, along with our crazy and loving poodle, Maggie. I am so very lucky to have found such a wonderful partner to share the journey of life together.

There are truly too many people to thank, and I apologize to all those who I have missed. It is a testament to those at Vanderbilt University, and specifically the

Department of Cell and Developmental Biology that 5 pages of acknowledgements are not enough.

Without further ado, I take you on a journey to understand, at the most basic level, how cells generate the forces required for movement. It may not be glorious, but like the great adventures of captains and crews from the age of discovery, it represents a journey undertaken to understand the wonderful unknown. This journey is deeply personal, yet similar stories of discovery are legion, and we take comfort in the camaraderie of the scientific endeavor. I invite you to settle in and immerse in our shared journey.

TABLE OF CONTENTS

Page

Chapters

LIST OF FIGURES

Figure Page

ABBREVIATIONS

Non-muscle myosin II	NMII
Non-muscle myosin II filament	NMII-F
Structured Illumination Microscopy	SIM
Single particle tracking photo-activated localization microscopy	sptPALM
Human pluripotent induced stem cell derived cardiac myocytes	hiCMs
Muscle Stress Fiber	MSF
β cardiac myosin II	βCMII
Electron microscopy	EM
Knockdown	KD
Knockout	KO
Short interfering RNA	siRNA
Green Fluorescent Protein	GFP
Small molecule inhibitor of formin homology domain 2	SMIFH2
Morpholino	MO
Hours post fertilization	hpf
Gene Names	*Italics*

Chapter I

Introduction

Force generation in living systems

Force generation is a fundamental property of life, from the microscopic to the macroscopic levels. Nowhere is this more readily apparent than the force dependent phenomenon of movement. The ability to move affects every living organism. Obvious examples include the thrilling chase of hunter and prey, and the powerful but graceful movements of a ballerina. Less obvious, but no less important is the subtle, determined growth of a plants intricate network of life-provide roots, and the digestive processes of a stationary, filter feeding sponge. Beneath the level of detection of the human eye, these desperate movements are just as prevalent, where “molecular motors” drive movement required for life sustaining processes. Whip-like cilia powered by kinesin and dynein motors allow single cell eukaryotes to swim and hunt prey, and eukaryotic cells in complex tissues to establish left-right asymmetry. The muscles of the hunter and ballerina are power by the contraction of myosin and actin. These macroscale and molecular movements have fascinated humanity from the beginning, as ancient cave paintings of hunting scenes by our ancestors can confirm. More recently, a series of elegant experiments by Italian scientists Caldani and Galvani in the late 1700s and early 1800s highlights our fascination with force generation and movement. These experiments demonstrated electricity could excite and cause the movement of muscle of a cadaver, experiments which inspired aspects of Mary Shelley’s Frankenstein (Hill, 2012). Over 200 years later, how force generation occurs still fascinates scientists and non-scientists alike.

Actin and Myosin II Based Force Generation

Force generation at the cellular level is critical for eukaryotic development, homeostasis, and the progression of force dependent diseases such as cancer (Babbin et al., 2009; Ma and Adelstein, 2014b; Samuel et al., 2011; Tullio et al., 1997; Xia et al., 2012). Molecular motors coordinate with cytoskeletal elements, such as actin filaments, to drive force dependent processes such as cell migration, cell division, and muscle contraction (Even-Ram et al., 2007; Gupton and Waterman-Storer, 2006; Huxley, 1969; Mabuchi and Okuno, 1977; Sandquist et al., 2006; Spudich, 2014; Straight et al., 2003). These seemingly diverse processes are all driven by forces generated by the same contractile machinery: actin and myosin II (Fenix and Burnette, 2018; Hartman and Spudich, 2012; Vicente-Manzanares et al., 2009b).

Actin and myosin II represent two of the longest studied proteins in modern science. German scientist, Willy Kuhne, discovered the first myosin II complex in 1864 (Hartman and Spudich, 2012; Kuhne, 1864). Almost a century later, the great Hungarian scientist, Albert Szent-Gyorgyi (who shared the 1937 Nobel Prize for the discovery of Vitamin C) in a series of elegant papers, isolated actin and myosin (separately) from skeletal muscle and demonstrated the contractile ability of the isolated proteins (Szent-Gyorgyi, 1943a; Szent-Gyorgyi, 1943b). Dr. Szent-Gyorgyi described the contraction of actin and myosin threads as, “perhaps the most exciting experience of my research career.” (Szent-Gyorgyi, 1963) Building upon these critical early observations, advances in technology have exponentially increased our understanding of these proteins at the genetic, structural, and functional level, though there remains much to discover. Specifically, how cells build the complex and highly ordered actin and myosin II machinery required to generate the observed force generation Dr. Szent-Gyorgi so passionately described.

Myosin II

Myosins represent a superfamily of proteins which hydrolyze ATP and bind to actin (Hartman and Spudich, 2012). Myosin motors are directly involved in a diversity of process including muscle contraction, molecular transport, endocytosis, stress fiber assembly, and cell differentiation (Vicente-Manzanares et al., 2009b). For the purposes of this work, we will focus on “conventional” myosin molecules, referred to as myosin II. Myosin II was the first discovered myosin, isolated from skeletal muscle samples (Hartman and Spudich, 2012; Szent-Gyorgyi, 1943a; Szent-Gyorgyi, 1943b). Subsequently, multiple myosin IIs, encoded by separate genes have been discovered (Hartman and Spudich, 2012). While these myosin II genes show high sequence homology and protein structure, they have diverse tissue localizations and biological roles. Cardiac myosin IIs and skeletal myosin IIs drive the heart beat and skeletal muscle contraction, respectively (Resnicow et al., 2010; Yamauchi-Takihara et al., 1989). Smooth muscle myosin II is involved in involuntary contraction such as esophageal contraction (Eddinger and Meer, 2007). So called, “non-muscle myosin IIs” (NMII) localize to most tissues and are involved in a number of developmental, homeostatic, and disease associated process (Fenix and Burnette, 2018; Vicente-

Manzanares et al., 2009b). Here, we will focus on NMIIs, as they are the most relevant for this work, and the most thorough characterization has been performed using these myosins.

NMII is the major molecular motor responsible for generating contractile forces within non-muscle cells (Vicente-Manzanares et al., 2009b). To carry out its wide variety of cellular functions, NMII assembles into filaments capable of generating force. A single NMII molecule is a hetero-hexamer composed of 2 heavy chains, 2 essential light chains, and 2 regulatory light chains (Figure 1-1) (Vicente-Manzanares et al., 2009b). The N-terminal motor domains of the myosin II heavy chains contain both the actin binding and ATPase activity (Adelstein et al., 1971; Vicente-Manzanares et al., 2009b). C-terminal electrostatic interactions of the rod domains from multiple NMII molecules creates a bipolar filament, positioning the N-terminal motor domains on opposite sides of the filament (Figure 1-1) (Fenix and Burnette, 2018; Vicente-Manzanares et al., 2009b). The motor domains of each NMII molecule in a filament can bind and contract actin filaments, but the number of NMII molecules added to a NMII filament is limited (Billington et al., 2013; Pollard, 1975). Thus, the actin binding and force generating capabilities of a single NMII filament is limited.

At the genetic level, there are three paralogs of NMII, each encoded by their own gene; NMIIA (*MYH9*), NMIIB (*MYH10*), and NMIIC (*MYH14*) (Fenix and Burnette, 2018; Vicente-Manzanares et al., 2009b). These proteins are strikingly similar, with over > 90 percent sequence homology. Despite this similarity however, these proteins have been shown to show diverse and non-redundant roles in both development and homeostasis (Vicente-Manzanares et al., 2009b). In addition, the small areas of divergence have recently been shown to be crucial for regulation (Juanes-Garcia et al., 2015). At the structural level, these proteins are also very similar. Rigorous *in vitro* characterization has shown all NMII molecules form bipolar filaments of similar size and number of molecules (Billington et al., 2013). Fascinatingly, recent work has shown the existence of NMII “co-filaments”, which contain multiple paralogs of NMII (Beach et al., 2014; Shutova et al., 2014). For the purposes of this work, we will focus on NMIIA and NMIIB, as they are highest expressed paralogs in our model systems discussed below.

The importance of NMIIA and NMIIB can be visualized by their dramatic effects when perturbed in model organisms, and their contribution to human disease. Germline NMIIA KO mice fail to gastrulate (Conti et al., 2004). Germline NMIIB KO mice die *in utero* due to heart failure (Tullio et al., 1997). Patients containing mutations in NMIIA present with a class of disorders referred to as May-Hegglin disorders (Costa et al., 2000; Hussein et al., 2013). These patients display a platelet disorder resulting in excessive bleeding which can cause headaches, muscle weakness, intracranial bleeding, blindness, and deafness. A mutation in NMIIB was also recently discovered in a patient who was non-ambulatory, non-verbal, and required a gastrostomy tube (Tuzovic et al., 2013). Collectively, these *in vivo* studies highlight the need to understand how NMII filaments coordinate with actin filaments to generate force within cells.

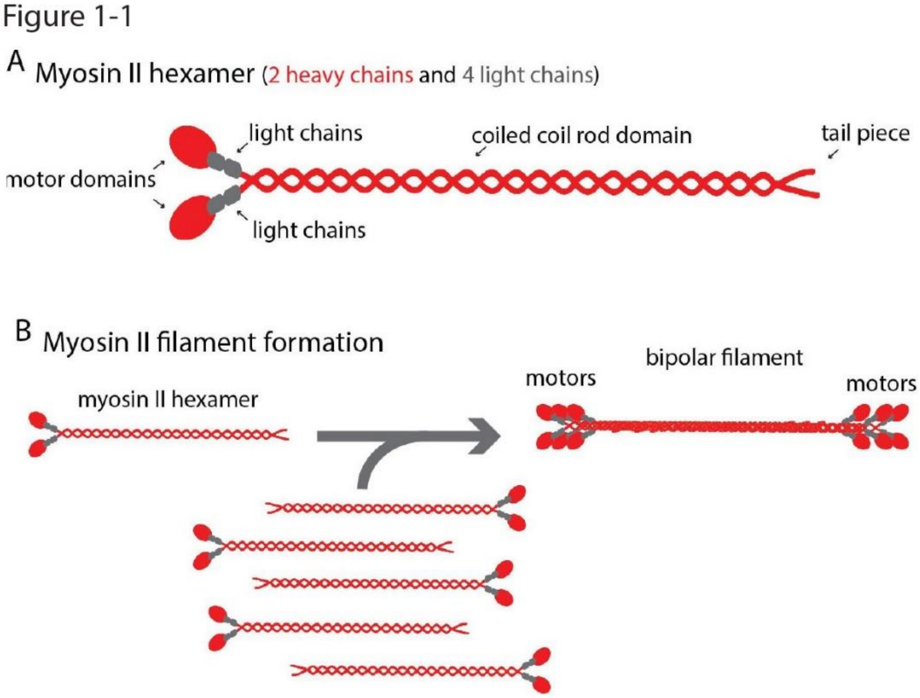

Figure 1-1: Myosin II filament formation
A) Schematic of a single NMII molecule and a NMII filament. Heavy and light chains are colored red and gray, respectively. Motor and rod domains are denoted by arrows. B) Bipolar filaments arise from non-covalent electrostatic rod domain binding.

Actin

Actin is a protein found throughout eukaryotes, and contains three paralogs, which are structurally and genetically very similar, but contain distinct tissue localizations and functions (Dominguez and Holmes, 2011). Actin subunits (G-actin) polymerize to form the larger F-actin structure (Dominguez and Holmes, 2011) (Figure 1-2). For this work, unless stated, when actin is mentioned we are referring to the F-actin structure. Actin filaments are polar, containing a “plus” end and “minus” end (Figure 1-2) (Pollard, 2016; Pollard and Borisy, 2003). Myosin II filaments bind to F-actin and “walk” towards the plus ends (Pollard, 2016). This allows the bipolar myosin II filaments (Figure 1-1) to contract and pull on actin filaments resulting in force generation. In addition to myosin II, there are hundreds of actin binding proteins which affect the structure, dynamics, and function of actin inside cells (Breitsprecher and Goode, 2013; Pollard, 2016; Pollard and Borisy, 2003). One class of proteins, actin polymerizing factors, nucleates distinct actin filament populations.

Figure 1-2

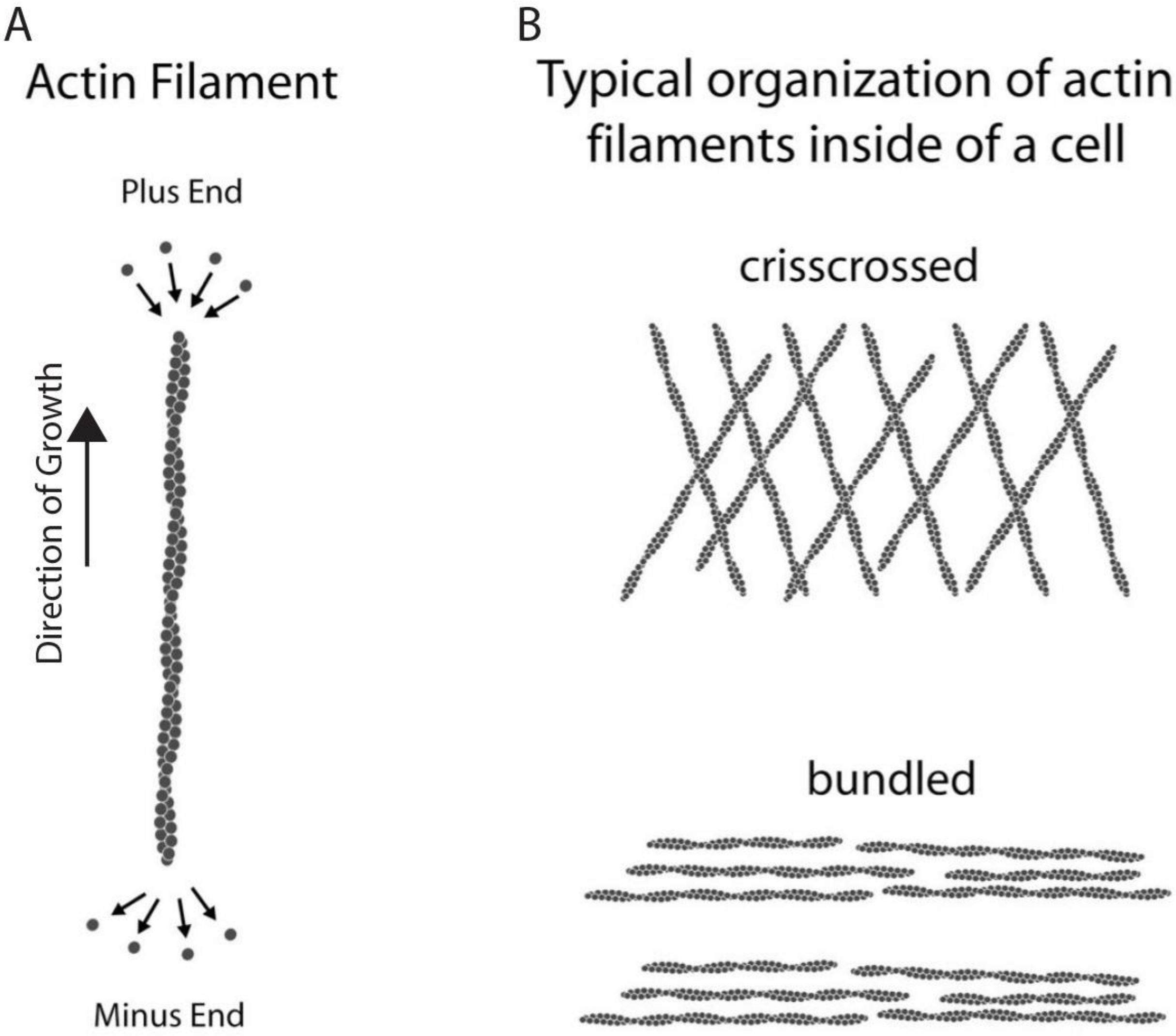

Figure 1-2: Actin filament assembly
(A) G-actin (single dots) can be added to both the minus end and plus end of actin filaments. Addition (and subtraction) of g-actin is favored at the plus end and the f-actin filament (chain of dots), will grow in the direction of the plus end. (B) Two major organization of f-actin. Crisscrossed or branched actin (top) is often found at the leading edge of cells and nucleated by the Arp2/3 complex. Bundled (bottome) actin is often found in structures such as ventral stress fibers, and is nucleated by formins.

In general, actin polymerizing factors are represented by the Arp2/3 complex, and formin proteins (Breitsprecher and Goode, 2013; Pollard, 2007). The Arp2/3 complex nucleates branched actin filaments (f-actin filaments growing off the side of existing f-actin filaments) and is often found at the leading edge of crawling cells (Figure 1-2) (Breitsprecher and Goode, 2013; Pollard, 2007). Despite this known role, the Arp2/3 complex likely has more diverse and as of yet undiscovered roles inside cells. While the Arp2/3 complex leads to branched actin, formins nucleate unbranched actin filaments (Figure 1-2) (Breitsprecher and Goode, 2013; Pollard, 2007). Formin-mediated actin filaments can be found in structures such as filopodia and actin emanating from focal adhesions. In addition to other actin binding proteins, the Arp2/3 complex and formins are instrumental in creating the diverse actin structures found within crawling cells (see below).

Actin, along with microtubules and intermediate filaments, is considered a major component of the “cytoskeleton”. Given this nickname, it is not surprising actin is required for cell shape and structure. Diverse actin structures contribute to the wonderful diversity of cell shapes honed for specific tasks. Below, we will focus on one of these specific tasks, cell migration, which has been instrumental in understanding the actin cytoskeleton.

Cell migration as a model system

Cell migration, the process of a cell moving from one place to another has fascinated scientists for generations, and is absolutely required for development, homeostasis, and the progression of devastating disease states such as cancer metastasis (Vicente-Manzanares et al., 2009b). Cells can move as single units (i.e., during the immune cell response to a wound), or collectively with many cells (i.e., during gastrulation, the process which establishes the basic body plan) (De Pascalis and Etienne-Manneville, 2017; Mayor and Etienne-Manneville, 2016). Cells can also move in both 2 dimensions on a relatively flat surface, or in more complex 3 dimensional environments (De Pascalis and Etienne-Manneville, 2017). For the purposes of this work, we will focus on 2 dimensional (2D) cell migration of single cells as a model system to study contractile unit assembly (Figure 1-3).

For decades, scientists have been plating cells on 2D substrates to observe how cells crawl, and more recently with the advent of immunofluorescence, how subcellular structures are regulated during cell migration. Though a 2D substrate mimics certain topologies found *in vivo*, such as an epithelial wound, extracellular matrix fibrils, and bone, they have recently come under criticism for not representing an *in vivo* like, or 3D environment (Petrie and Yamada, 2012). Despite this criticism, work on 2D crawling cells has revealed a plethora of structures, such as focal adhesions and actin stress fibers, which the latest and highest resolution *in vivo* microscopy techniques are now confirming to exist *in vivo* (Figure 1-3) (Harunaga and Yamada, 2011; Liu et al., 2018).

One structure which 2D studies on crawling cells have been particularly rewarding to study has been the actin cytoskeleton (Figure 1-3). Crawling cells contain a number of actin based structures which each have their own molecular composition and modes of regulation (Tojkander et al., 2012). The lamellipodium is a thin, protrusive region at the leading edge of crawling cells, containing both branched and unbranched actin filaments. Actin polymerization coupled with focal adhesions drive the membrane protrusion (Krause and Gautreau, 2014; Swaminathan and Waterman, 2016). Behind the lamellipodium is the lamella, which contains transverse actin arcs and dorsal stress fibers (Figure 1-3) (Tojkander et al., 2012). Dorsal stress fibers extend from focal adhesions on the bottom of the cell, to the actin arcs on top of the cell and are devoid of NMII (Figure 1-3) (Burnette et al., 2014a; Hotulainen and Lappalainen, 2006; Tojkander et al., 2012). Actin arcs, found on top of the cell, contain NMII, and are required for efficient cell migration and the shape of migrating cells (Figure 1-3) (Burnette et al., 2014a; Hotulainen and Lappalainen, 2006; Tojkander et al., 2012). Ventral stress fibers are large actin structures containing NMII and adhesions at either end (Figure 1-3) (Tojkander et al., 2012).

While these structures have been well characterized in a variety of cell types and culture systems, much remains to be understood concerning their diverse modes of regulation and function in cells. While readily apparent in cultured cells, recent work utilizing rapidly advancing microscopy techniques has confirmed the existence of these actin stress fiber populations in a variety of *in vivo* contexts (e.g., during wound healing and immune response), and functional assays (e.g., T-cell target engulfment) (Chen et al., 2014; Liu et al., 2018; Small, 1998). At the moment, it appears “simple” crawling cells will continue to be an informative model system for cell motility and the regulation of actin structures. For the purpose of this discussion, we will focus on actin arcs as a model to study NMII filament stack assembly, and later, as a model to inform our studies investigating sarcomere assembly in cardiac myocytes.

Figure 1-3

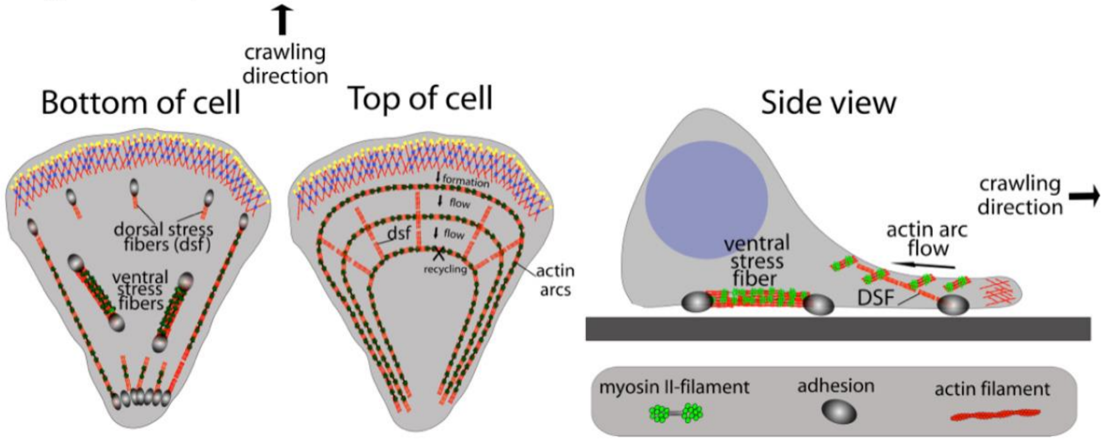

Figure 1-3: Cartoon Schematic depicting major actin structures in migrating cells (A) Bottom (left) and Top (right) views of a crawling cell. Lamellipodia (yellow puncta) contains both branched and f-actin filaments. Dorsal stress fibers arise from adhesions (gray structures), and ventral stress fibers are in the middle of the cell and contain myosin II and are anchored at each end by adhesions. On top of the cell, actin arcs containing myosin II are connected to dorsal stress fibers which couple actin arcs to the adhesions. (B) Side-view of the typical shape of a crawling cell. Contractile actin arcs pull on dorsal stress fibers resulting in a relatively flat leading edge.

Actin Arcs

Actin arcs were first discovered in 1983 by Julian Heath (Heath, 1983). These structures were characterized as being parallel to the leading edge of cells and undergoing retrograde flow from the leading edge towards the cell body (Heath, 1983). Though first discovered in chick fibroblasts, these structures were subsequently described in a number of diverse cell types (Burnette et al., 2011; Henson et al., 2015; Medeiros et al., 2006; Murugesan et al., 2016; Tojkander et al., 2012). Decades of subsequent work has revealed the intricate mechanisms regulating actin arc dynamics and regulation (Tojkander et al., 2012). Actin arcs undergo retrograde flow towards the cell body at ~200nm/s in most non-muscle cell types (Ponti et al., 2004). Actin arc formation requires NMIIA, the Arp2/3 complex, the formins dia1 and dia2, and tropomyosin 4 (Burnette et al., 2014a; Hotulainen and Lappalainen, 2006; Murugesan et al., 2016; Shutova et al., 2017; Tojkander et al., 2012; Tojkander et al., 2011). Despite a wealth of knowledge, the function of actin arcs remained elusive until relatively recently.

In 2011, (Burnette et al., 2011) used live-cell microscopy to show actin arcs couple to focal adhesions at the leading edge of cells. The coupling between focal adhesions and actin arcs ensured a net protrusion of the leading edge of cells and efficient cell migration (Burnette et al., 2011). Subsequent work from this group used a recently developed super-resolution microscopy technique (structured illumination microscopy), to show actin arcs are on the dorsal surface (top) of the cell (Burnette et al., 2014a). Loss of actin arcs via NMIIA KD and NMII inhibition (via the inhibitory molecule blebbistatin) resulted in a loss of actin arcs, and interestingly, loss of the stereotypical “flat” shape of cells at the leading edge (Burnette et al., 2014a). Thus, actin arcs are required for shaping crawling cells. In addition, this work showed that NMIIA stack assembly occurred via the growth of small bundles of NMIIA filaments on actin arc structures (Burnette et al., 2014a). This observation was in direct contrast to the major model of NMIIA stack formation, known as the Network Contraction Model (Burnette et al., 2014a; Verkhovsky et al., 1999a).

Non-muscle myosin II filament and stack assembly

The organization of NMII filament stacks was first reported in a series of elegant papers by Gary Borisy and colleagues in the 1990’s (Svitkina et al., 1997; Verkhovsky and Borisy, 1993; Verkhovsky et al., 1995). Borisy’s group adapted an electron microscopy (EM) technique termed platinum replica EM to facilitate the exquisite visualization of the cytoskeleton’s architecture within motile rat fibroblasts and fish keratocytes (Svitkina et al., 1997; Verkhovsky and Borisy, 1993; Verkhovsky et al., 1995). Key findings from these studies revealed a ‘non-sarcomeric” organization of NMII filaments at the protruding edge of cells in which NMII filaments were arranged in splayed out arrays apparently connected by their motor domains, and NMII filament stacks toward the cell center (Figure 1-4) (Verkhovsky and Borisy, 1993; Verkhovsky et al., 1995). These observations led to the “Network Contraction” Model (Figure 1-4) to explain how the actin and NMII architecture in cells was formed (Verkhovsky et al., 1999a). The Network Contraction Model posits that tension generated by NMII organizes the unaligned actin architecture found at the leading edge, into the more organized and aligned actin filaments found further back in the lamella (Figure 1-4) (Verkhovsky et al., 1999a). One of the key predictions of the Network Contraction model is that NMII filaments in the splayed configuration would come together as they pull on actin filaments (Figure 1-4). For ~20 years, the Network Contraction Model has become the textbook model for actin stress fiber assembly and myosin II stack assembly. Indeed, the Network Contraction Model is still being promoted as the major model of NMII stack formation (Svitkina, 2018). In Chapter III of this work, we investigate the discrepancy noted by (Burnette et al., 2014a) with the Network Contraction Model using a combination of super-resolution microscopy, live-cell imaging, and crawling cells as a model system. We provide evidence for a new model of NMIIA stack assembly we refer to as the “Expansion” model of NMIIA stack assembly which directly contradicts the Network Contraction Model (see Chapter III).

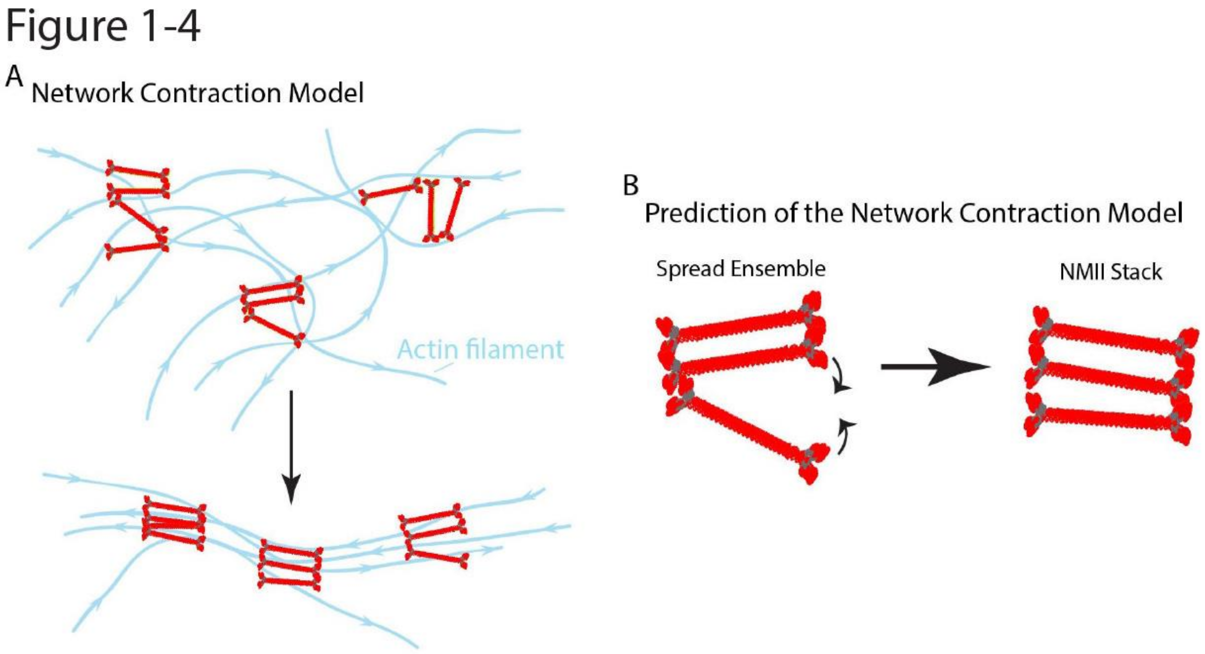

Figure 1-4: Network Contraction Model
A) Network contraction model redrawn from Figure 5 of Verkhovsky et al. 1999. Myosin II filaments and actin filaments are red and blue, respectively. Arrow indicates the transition between splayed myosin and actin filament arrays and aligned arrays. B) A key prediction of the Network Contraction model is that spread myosin II filaments in small clusters move together (curved arrows).

Observations on the similarities between non-muscle and muscle contractile systems

Our studies investigating NMIIA filament stack assembly revealed detailed physical and molecular regulatory mechanisms. Despite this, no study is exhaustive and much work remains to elucidate the mechanisms by which cells assemble NMIIA stacks. These include, but are not limited to the roles of actin bundling proteins (e.g., α-actinin), and post-translational modifications (e.g., phosphorylation). While these studies are on-going in the Burnette lab, a major observation led us to investigate the mechanisms of muscle myosin II stack assembly in cardiac myocytes.

Structurally, both NMII and cardiac myosin II (CMII) form bipolar structures with their motor domains on opposite sides of the filament (Figure 1-5). Similar to NMII in non-muscle crawling cells, CMII forms filaments and filament stacks in cardiac myocytes (Figure 1-5). Indeed, initial descriptions of NMII filaments in crawling cells referred to their organizations as “non-sarcomeric” at the leading edge, and “sarcomeric” in the cell body (Verkhovsky and Borisy, 1993; Verkhovsky et al., 1999a). Furthermore, both NMII and CMII share a fundamental function, to contract actin filaments in order to generate force. These similarities led us to test the mechanisms of CMII stack assembly in cardiac myocytes. Furthermore, we drew upon our results from studies investigating NMIIA stack assembly to establish a conceptual frame work, and to guide our initial experiments in order to test the mechanisms leading to CMII stack assembly.

Figure 1-5

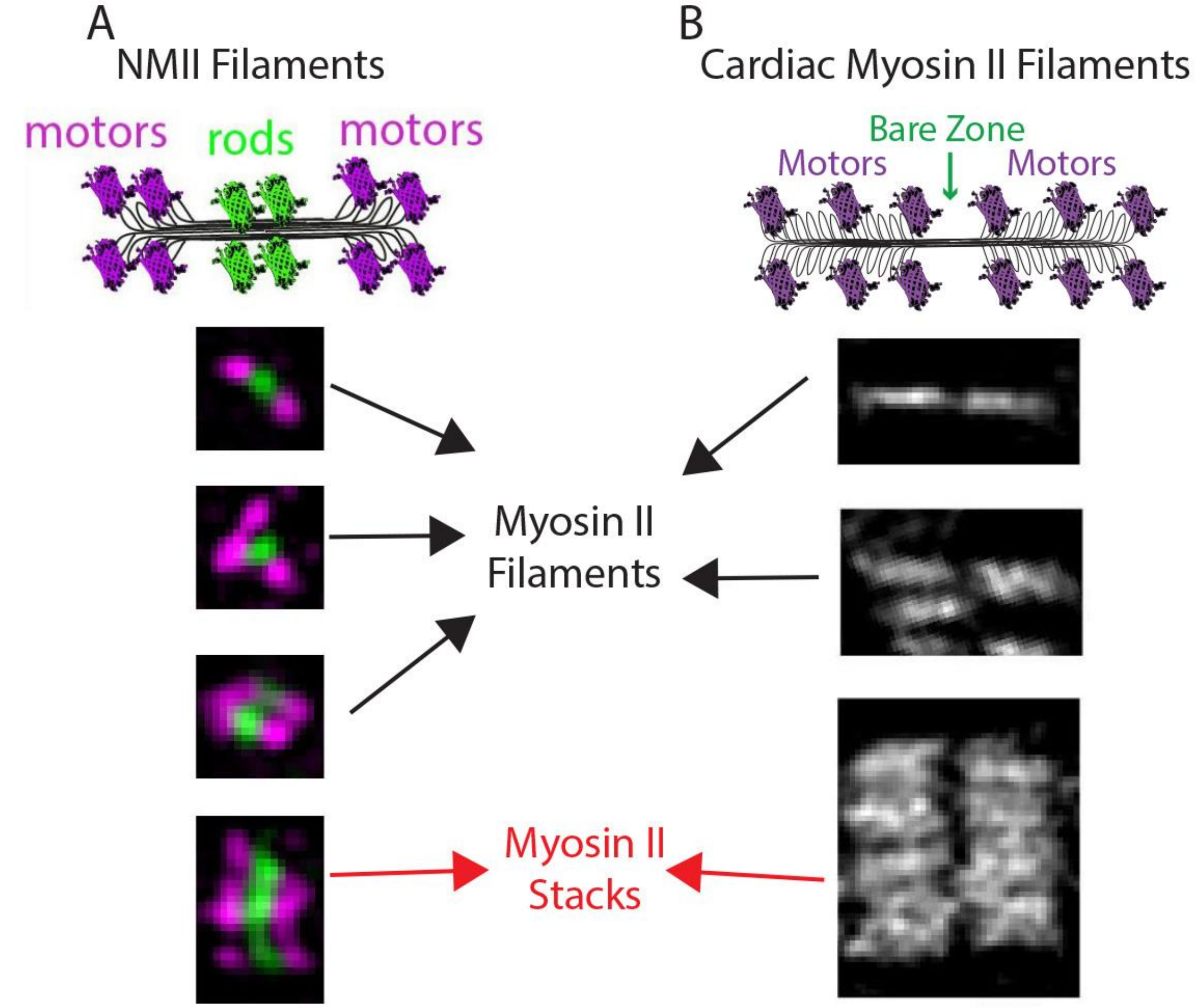

Figure 1-5: NMII filament stacks resemble Cardiac Myosin II Stacks
(A) Motor and rod domains of NMIIA filaments (black arrows) and a NMIIA filament stack (red arrow). (B) Motor domains of cardiac myosin II filaments (black arrows) and filament stack (red arrow).

Sarcomere structure and assembly in cardiac myocytes

Cardiac myocytes represent a major cell type within the heart, comprising ~50% of the cells within the heart. Cardiac myocytes “beat” (i.e., contract) in response to electrical signals passed through specialized gap junctions (e.g., intercalated discs). The coordinated contraction of cardiac myocytes results in the beating of the heart, and blood flow throughout the body (Hill, 2012). The complex mechanisms of cardiac myocyte contraction – while fascinating – are highly dependent on a variety of stimuli, and not directly relevant to this work. Detailed reviews of these mechanisms are reviewed elsewhere (Hill, 2012). Instead, here we focus on how the structures leading to the coordinated contraction of cardiac myocytes are assembled in live cells.

The fundamental unit of force generation within cardiac myocytes is the sarcomere. At its core, a sarcomere is composed of “thick” myosin II filaments, and “thin” actin filaments (Figure 1-6) (Au, 2004). One sarcomere is measured from Z-line to Z-line, which contain α-actinin 2 (Figure 1-6). The thick myosin II filaments “walk” towards the plus ends of actin filaments embedded in the Z-lines, resulting in a contraction of the sarcomere (Z-lines coming closer together, “sarcomere shortening”) and force generation (Huxley and Niedergerke, 1954a; Huxley and Niedergerke, 1954b). Multiple sarcomeres aligned adjacently with one another form a larger structure referred to as a myofibril. The proper establishment of cardiac sarcomeres and myofibrils during development and their subsequent maintenance is critical for heart function. Indeed, disorganized sarcomeres are a hallmark of both dilated and hypertrophic cardiomyopathies in humans (Harvey and Leinwand, 2011; Ho, 2010; Hughes, 2004; Hughes and McKenna, 2005; Ribeiro et al., 2015; Watkins et al., 2011).

While the sarcomere has been well characterized using static high-resolution microscopy (e.g., snapshots from electron microscopy) as well as molecular and biochemical techniques, we do not know how the molecular components of the sarcomere are dynamically assembled/disassembled or how this changes during disease.

Figure 1-6

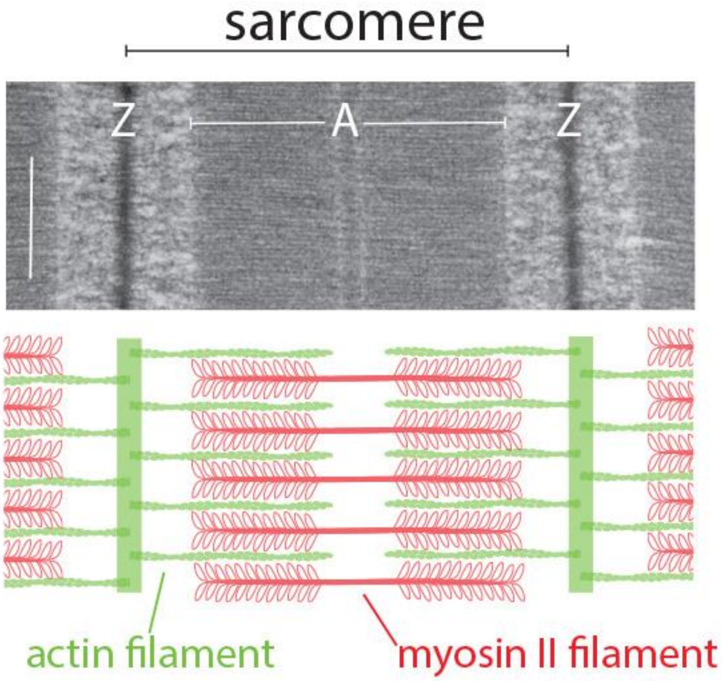

Figure 1-6: Structure of the Sarcomere
Electron microscopy (EM) of adult mouse heart (above) and cartoon representation of sarcomere (below). One sarcomere is measured from Z-line to Z-line (white Zs in EM image). Bipolar myosin II filaments (red) pull on actin filaments (green) causing sarcomere shortening and force generation. Note highly ordered structure of sarcomere in EM image.

Previous studies in cultured myocytes have shown the presence of actin bundles called “stress fiber-like structures” similar in appearance to classic stress fibers (Dlugosz et al., 1984). These stress fibers were often found to be close to the edge of the myocyte with sarcomeres existing further from the edge (Rhee et al., 1994). These studies proposed that the stress fibers served as a template for the formation of sarcomeres (Figure 1-7) (Dlugosz et al., 1984; Rhee et al., 1994; Sanger et al., 2005). The original model that proposed this was called the Templating Model (Dlugosz et al., 1984), and was proposed before it was known these stress fibers contained both non-muscle and sarcomeric proteins (Figure 1-7) (Rhee et al., 1994). Beyond non-muscle myosin IIB (NMIIB), which is present in non-muscle cells, stress fibers in muscle cells contain muscle specific proteins, such as α-actinin, tropomyosin, troponins, and tropomodulin (Almenar-Queralt et al., 1999; Rhee et al., 1994; Sanger et al., 2005). Each of these proteins have non-muscle paralogs, which likely serve similar functions (Bryce et al., 2003; Colpan et al., 2013; Cote, 1983; Gunning et al., 2015; Lim et al., 1986; Sjoblom et al., 2008). Partly in response to the presence of muscle specific proteins in stress fibers, the Templating Model was modified to the “Pre-Myofibril Model” (Figure 1-7) (Rhee et al., 1994; Sanger et al., 2005). Even though these models have different names and are often presented as mutually exclusive, they are very similar in their predictions (Figure 1-7). Specifically, both models posit an actin bundle that appears structurally similar to a stress fiber will acquire a row of sarcomeres over time to become a “myofibril” (Dlugosz et al., 1984; Rhee et al., 1994; Sanger et al., 2005) (Figure 1-7). There is a vast amount of localization data in fixed cardiomyocytes to support these models. However, there is very little dynamic data in live cells that suggests stress fibers give rise to sarcomeres. The strongest dynamic support comes from imaging fluorescently tagged α-actinin 2 in myocytes. Time montages from chick skeletal myotubes showed small puncta of α-actinin 2 adding to pre-existing Z lines (McKenna et al., 1986). Subsequently, a time montage was used to show a similar phenomenon occurring in chick cardiomyocytes (Dabiri et al., 1997).

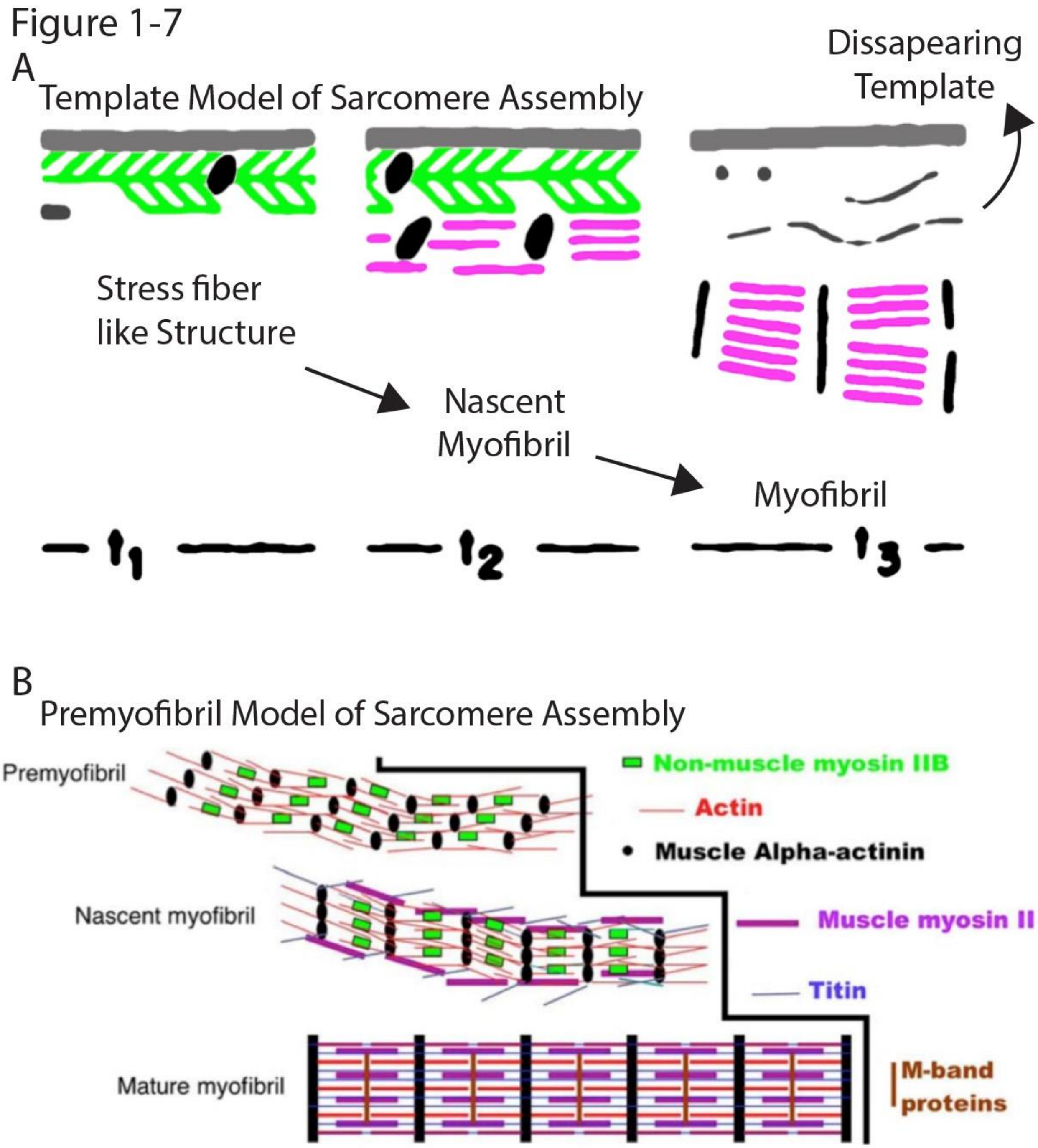

Figure 1-7

(A) Template Model of sarcomere assembly. This model predicts that stress fiber like structures, staining continuously for actin will, over time, transition to a nascent myofibril and eventually a myofibril. Key predictions include the ideas that the stress fiber like structures will acquire muscle specific proteins as the mature, and the stress fiber template will disappear as the myofibril is assembled. Cartoon is a reproduction of the original Template Model. (B)

Premyofibril Model of sarcomere assembly. Similar to the Template Model, the Premyofibril envisions a precursor structure (premyofibril) transitioning to a myofibril over time. The premyofibril contains muscle and non-muscle paralogs of proteins, the latter of which is lost over time. This model, while very similar to the Template Model, disputes the idea that the premyofibril is a template, as it doesn't "disappear" over time. Cartoon is a reproduction from the original Premyofibril Model.

Some *in vivo* data support the Template/Pre-Myofibril Model, while others do not. In strong support of the Template/Pre-Myofibril Model, static images of chick heart tissue have essentially revealed every structure described in primary cultured chick cardiomyocytes (Du et al., 2008). The presence of NMIIB-containing stress fibers in the cardiomyocytes was particularly clear (Du et al., 2008). NMIIB germline knockout (KO) mice were also reported to have fewer and disorganized sarcomeres via EM (Tullio et al., 1997). On the other hand, several studies have called into question the role of stress fibers in sarcomere assembly. First, several studies examining cardiomyocytes within mouse or chick heart tissue did not find stress fibers containing NMIIB (Ehler et al., 1999; Kan et al., 2012; Ma et al., 2009). In addition, a conditional KO mouse that removes NMIIB genetically at P9 apparently still had striated sarcomere structures (Ma et al., 2009). Finally, a conditional heart KO of the other major paralog of NMII, NMIIA, was also reported to have no apparent defects in heart formation (Conti et al., 2004; Conti et al., 2015). Taken together, the lack of clear data showing stress fibers in cardiomyocytes and inconsistencies for a role of NMII in sarcomere assembly calls into question whether the Template/Pre-Myofibril Model is a viable construct for understanding sarcomere assembly (Sanger et al., 2005; Sparrow and Schock, 2009).

There is further data to suggest that a mechanism other than that described in the Template/Pre-Myofibril model could be driving sarcomere assembly. This alternative model—called the “Stitching Model”—is based on the idea that parts of a sarcomere are assembled independently and then brought together (i.e., stitched) (Holtzer et al., 1997; Lu et al., 1992; Sanger et al., 2005). In support of the Stitching Model, studies in *Drosophila* have shown the presence of small myosin filaments following knockdown (KD) of separate Z-line components (Rui et al., 2010). This data suggests that myosin filaments can assemble independently of Z-lines. Indeed, there are also electron micrographs that appear to show stacks of myosin II filaments (i.e., A-bands) without detectable actin filaments in skeletal muscle (Holtzer et al., 1997; Lu et al., 1992; Sanger et al., 2005). Examination of electron micrographs also supports the idea that bodies containing Z-line components and actin filaments—called “I-Z-I” bodies—could also exist in skeletal muscle without apparent myosin II filaments (Holtzer et al., 1997; Lu et al., 1992; Sanger et al., 2005). Based on this data, it was proposed that stitching could occur through sequential assembly by adding new I-Z-I bodies and myosin II filaments (Holtzer et al., 1997; Lu et al., 1992; Sanger et al., 2005).

Despite these proposed models, dynamic and mechanistic data surrounding sarcomere assembly is severely lacking (Sparrow and Schock, 2009). This is mainly due to the lack of a tractable model system to study this process. An ideal model system would be amenable to live-cell imaging, protein transfection, and siRNA mediated knockdown. Fortunately, due to recent advances in stem cell technologies, such a system is now theoretically available. In Chapters III and IV of this work, we develop and utilize a model system to study the mechanisms and dynamics of sarcomere assembly.

Chapter II

Non-muscle myosin IIA filament stack assembly

Fenix, AM., Taneja, N., Butter, CA., Lewis, J., Van Engelenburg SB., Ohi, R., Burnette, DT. (2016). *Mol Biol Cell*, 27(9)

Introduction

Forces generated by the molecular motor non-muscle myosin II (NMII) are essential for cell migration and cytokinesis (Gardel et al., 2010; Ma et al., 2012; Straight et al., 2003; Vicente-Manzanares et al., 2009a). Mutations in NMII isoforms lead to an array of human diseases, and changes in NMII activity during processes relying on precise regulation of cell migration and cytokinesis lead to developmental defects and disease progression (Beach et al., 2011; Hamdan et al., 2014; Hu et al., 2002; Kelley et al., 2000; Ma and Adelstein, 2014a; Seri et al., 2000; Tullio et al., 1997; Tuzovic et al., 2013; Vasquez et al., 2014; Vicente-Manzanares et al., 2009a). Furthermore, increased cellular contractility – which is primarily driven by NMII – is increasingly being recognized as an emergent property of tumor cells (Samuel et al., 2011). Highlighting this, overexpression of the NMIIA isoform is correlated with increased metastasis and poor patient prognosis in a variety of cancers (Ma et al., 2003; Xia et al., 2012). Despite the biological importance of, and wealth of genetic data surrounding NMIIA associated diseases, how NMIIA based contractile units form inside of cells is a surprisingly poorly understood process. This lack of understanding precludes a thorough understanding of NMIIA related disease states, and prevents potential therapeutic strategies.

A single NMII molecule is a hetero-hexamer composed of 2 heavy chains, 2 essential light chains, and 2 regulatory light chains (Vicente-Manzanares et al., 2009a). The N-terminal motor domains of the heavy chains contain both the actin binding and ATPase activity (Adelstein et al., 1971; Vicente-Manzanares et al., 2009a). In vitro biochemical and structural studies have elegantly shown that C-terminal electrostatic interactions of the heavy chains create bipolar filaments, positioning the N-terminal motor domains on opposite sides of the filament (Figure 2-1) (Pollard, 1975; Ricketson et al., 2010). In this orientation, the motor domains of NMII bipolar filaments can grab onto and contract actin filaments to generate force. Importantly, a single NMII bipolar filament contains multiple NMII molecules, each of which can bind to and contract actin filaments (Billington et al., 2013). The number of NMII molecules added to a NMII filament (NMII-F) is limited by steric hindrance however, and thus actin binding and force generating capabilities of a single NMII-F are limited (Billington et al., 2013; Pollard, 1975). Thus, in order to increase the scale of force generation, cells organize NMII-Fs into larger arrays referred to as “stacks” (Figure 2-1) (Svitkina et al., 1997; Verkhovsky and Borisy, 1993; Verkhovsky et al., 1995). The mechanism of NMII stack formation has eluded previous efforts. This is in part due to the relatively small size (~300nm in width) of NMII-Fs, resulting in structurally dynamic information being difficult to achieve utilizing conventional imaging modalities (i.e., diffraction limited microscopy), and because they do not readily form *in vitro*. Thus, current models surrounding NMII stack formation are based on fixed snapshots utilizing electron microscopy, which lack dynamic information (Verkhovsky et al., 1999b).

To address these issues, we have taken advantage of recently developed live-cell ‘super-resolution’ imaging techniques to investigate the dynamic mechanism of NMII stack formation. Interestingly, we found that at the leading edge of crawling cells, NMII stacks predominantly form via an expansion and concatenation of smaller NMII filaments, which is in contrast to the current models of NMII stack formation (Verkhovsky et al., 1999b). This expansion was dependent on NMII motor activity, and actin filament availability. Intriguingly, NMII expansion and concatenation also underlies the formation of the contractile ring in dividing cells. Thus, we present a new model of NMIIA stack formation that underlies the formation of contractile units in distinct cellular processes and cell types.

Results

We used the flat, leading edge of motile U2-OS cells (human osteosarcoma) as a model system to define the structural dynamics underlying NMII-F stack formation. NMII-Fs comprised of the NMII isoform, NMIIA, are formed at the leading edge of cells and then move away from the edge in a process called retrograde flow, making room for new NMIIA-Fs to form (Hotulainen and Lappalainen, 2006; Vallenius, 2013; Verkhovsky et al., 1995). This continuous treadmill allowed us to monitor NMIIA-F formation using high-resolution, wide-field fluorescence time-lapse microscopy (Figure 2-1). Examination of this data revealed that newly formed NMIIA-Fs increased in intensity over time (Figure 2-1). This was consistent with NMIIA molecules being added to the NMIIA-F. The increase in intensity was followed by a growth in size of the NMIIA-F (Figure 2-1). Conventional fluorescence imaging was not able to resolve the underlying structural changes during the expansion of NMIIA-Fs however. Thus, we turned to structured illumination microscopy (SIM) (Gustafsson et al., 2008), which has a resolution (~110 nm) can separate the motor and rod domains in a NMIIA-F (Burnette et al., 2014b).

To study the structure of NMIIA-Fs during expansion, we visualized motor and rod domains with SIM using two different localization methods. First, we exogenously expressed NMIIA heavy chain fused to mEmerald on the N-terminus and mApple on the C-terminus (Burnette et al., 2014b). This construct allowed us to image the motor and rod domains, respectively (Figure 2-1). We also localized endogenous NMII-Fs with antibodies specific to the NMIIA rod domain and myosin regulatory light chain (RLC) (Figure 2-S1). RLC is positioned in the neck region of NMIIA and was not distinguishable from a fluorescent protein tag on the N-terminus of the heavy chain using SIM (Figure 2-S1). Importantly, our data revealed similar NMIIA-F organizations as previously described by electron microscopy studies (Shutova et al., 2012; Verkhovsky and Borisy, 1993). Thus, we could use the relative localization of motor and rod domains to group together structurally similar NMIIA-Fs.

We defined the structure of an individual NMIIA-F by measuring the number of discrete “motor-groups” that could be resolved by SIM (Figure 2-1 and 2-S1). We use the term “motor-groups” because each contained multiple NMIIA motor domains, which was required for detection, as our SIM microscope did not have single molecule imaging sensitivity. In fixed cells, we found the majority (71.1 +/- 11.0%) of individual NMIIA-Fs at the leading edge fell into one of four structural categories: 2-motor-group, 3-motor-group, 4-motor-group and >4-motor-group NMIIA-Fs. Morphologies of the remaining ~30% of NMIIA-Fs were difficult to define mainly because they overlapped with other NMIIA-Fs. Of the individually resolvable NMIIA-Fs, 2-motor-group NMIIA-Fs were the most common (35.0 +/- 1.7 %), and had one motor-group on each side of the rod domains (Figure 2-1, 1 and 3;). Interestingly, the second most common organization was an asymmetric 3-motor-group NMIIA-Fs (25.2 +/- 1.4%), which had two motor groups on one side of the rod domains and one on the other side (Figure 2-1, 2). In contrast, 4-motor-group NMIIA-Fs (19.8 +/- 1.6 %) were relatively symmetrical with two motor groups on each side of the rod domain (Figure 2-1).

Several of the NMIIA-F organizations above have been reported by electron microscopy (EM) studies of fixed cells (Shutova et al., 2012; Verkhovsky and Borisy, 1993; Verkhovsky et al., 1995). Notably, EM has shown the existence of the 3-motor-group NMIIA-Fs in both crawling cells, and *in vitro* in a variety of salt and ATP concentrations (Billington et al., 2013; Verkhovsky et al., 1995). Importantly, this EM data shows that in the 3-motor-group orientation, NMII molecules of the same 3-motor-group filament are “linked” via interacting motor domain groups, which is consistent with our fluorescence data. However, there was still the possibility the 3-motor-group NMIIA-F in our SIM data was not a single unit, but two distinct filaments. Previous EM studies yielded inherently 2D views of NMII-Fs and the lateral and axial resolution of our 3D SIM data (~110 and ~250 nm respectively) may not be able to resolve two NMIIA-Fs close together, which also may result in an over-estimation of the percentage of 3-motor group filaments in our cells. Therefore, we turned to 3D PALM (Betzig et al., 2006; Brown et al., 2011) of U2-OS cells expressing NMIIA fused to mEOS2 on its N-terminus (i.e., motor). Our image strategy yielded an average single molecule localization precision of $\boldsymbol{\mu}_x$ = 11 +/- 5 nm and $\boldsymbol{\mu}_z$ = 20 +/- 11 nm, respectively (Figure 2-S1), which afforded us higher spatial resolution than SIM to test if the 3-motor-group filaments indeed had 3 groups of motors, as opposed to 4 if they were composed of two distinct filaments. We observed the groups of motors in the 2-motor-group NMIIA-Fs were similar in dimension to those previously shown by 2D PALM (Burnette et al., 2014b) (Figure 2-1 and 2-S2). Importantly, 3D PALM revealed isolated 3-group localization clusters, spaced by similar dimensions as 2-motor group clusters. Each motor-cluster visualized by 3D-PALM displayed a unimodal X,Y, and Z distribution, consistent with previous EM evidence and the interpretation of our SIM data (Figure 2-1 and 2-S2).

Figure 2-1

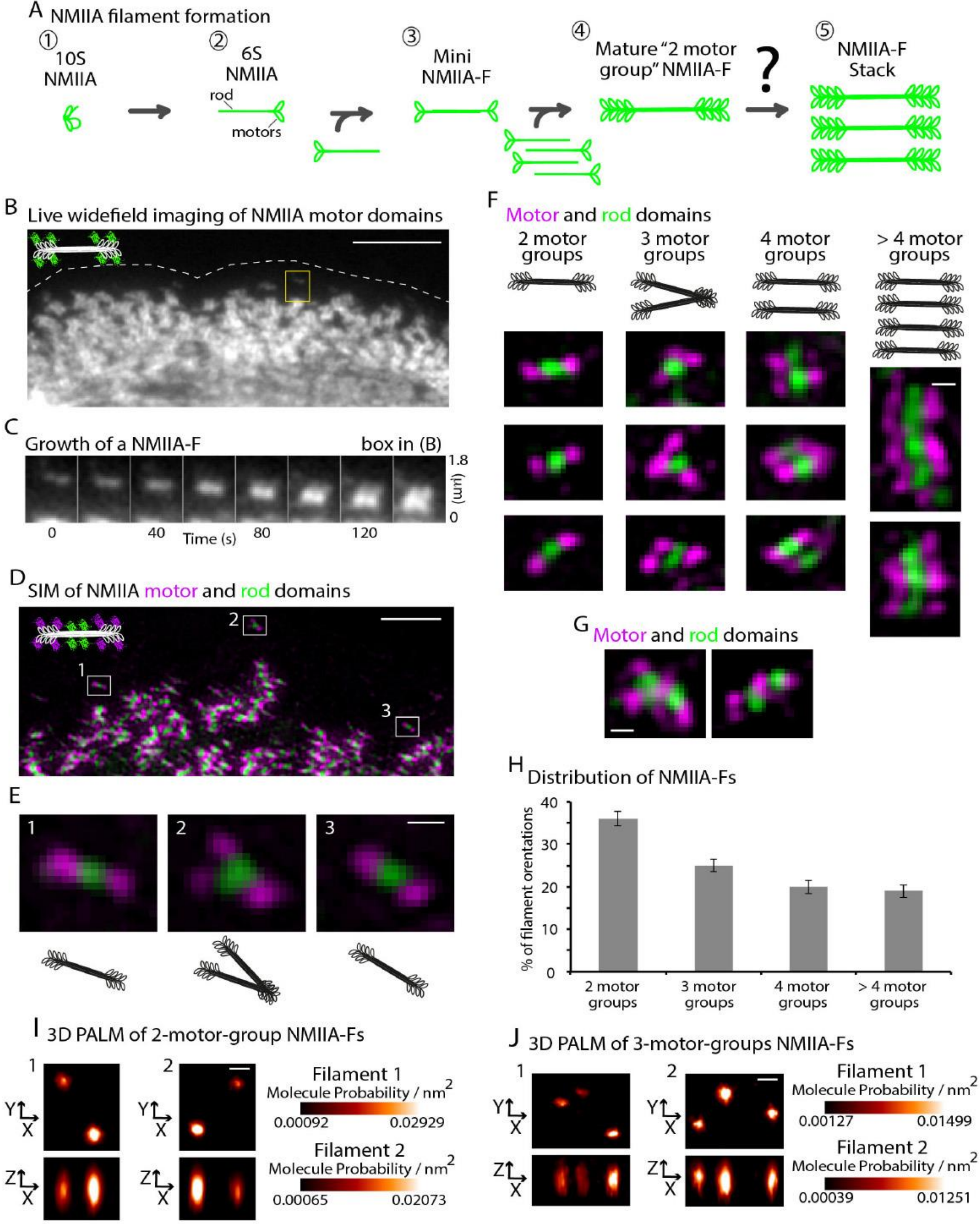

Figure 2-1: Organization of NMIIA-Fs at the leading edge.

A.) Classic model of the formation of a 2-motor-group NMIIA-F. An auto-inhibited NMIIA molecule (1) becomes polymerization competent (2) after phosphorylation of its regulatory light chain. Two polymerization competent NMIIA molecules then form a mini NMIIA-F (3) through electrostatic interactions of their rod domains. Addition of more NMIIA molecules to the mini-filament drives the growth of a 2-motor-group NMIIA-F (4). Steric hindrance limits the number of molecules that can be added to 2-motor-group NMIIA-F (Billington et al., 2013). Note a smaller number of myosins than the ~15 on each side of the filament are drawn for simplicity. Importantly, how larger contractile arrays (i.e., stacks) containing more myosins capable of generating more contractile forces is not understood (5). B) Time-lapse widefield epi-fluorescent recording of the motor domains, NMIIA-(N-terminal)-mEGFP, at the leading edge of a U2-OS cell. C) Representative montage shows the NMIIA-F in the box expanding into a stack. D) SIM of U2-OS cell expressing NMIIA heavy chain fused to mEmerald-N-terminal (magenta) and mApple-C-terminal (green). E) High mag views of boxes 1, 2, and 3 show a 2, 3 and 2-motor-group NMIIA-F, respectively. F) Representative examples of 2, 3, 4, and >4-motor-group NMIIA-Fs. G) Representative images of the ~30% of filaments which were too close (i.e., overlapping) for analysis. H) Percent of endogenous NMIIA-Fs (RLC and NMIIA antibodies) in a 2, 3, 4, or >4-motor-group organization at the edge of the cell. N= 246 total NMIIA-Fs from 37 cells over 3 experiments. I) X/Y and Z/Y views of 2-motor-group NMIIA-Fs imaged with 3D PALM. J) X/Y and Z/Y views of 3-motor-group NMIIA-Fs imaged with 3D PALM. Molecular probability refers to the cumulative probability per unit volume (nm^3) of all single molecules (mEOS2-NMIIA) detected within any given motor group (cluster of single molecule localizations). Our certainty for the location of each probe in a given image frame is dependent upon the number of photons detected for each mEOS2 molecule and the background parameters of the specimen and camera (Betzig et al., 2006). Scale bars: (B), 5 μm; (D), 2 μm; (E-G), 200 nm; (I-J), 100 nm. Error bars in (H) represent standard error of the mean (SEM).

The 3-motor-group filaments were the basis of previously proposed models of NMII stack formation (Verkhovsky et al., 1999b). Previous studies have proposed a spatial and temporal relationship between "open" NMII-Fs like the 3-motor-group and "closed" NMII-Fs like the 2-motor-group NMII-Fs to explain how actin filament networks are contracted (i.e., actin filaments being moved closer together) (Verkhovsky et al., 1999b). The "network contraction" model predicts a 3-motor-group NMIIA-F would transition to a 2-motor-group NMIIA-F similar to a pair of scissors closing (Figure 2-2) (Verkhovsky et al., 1999b). In theory, the two motor groups on the larger side of the 3-motor-group would pull different actin filaments together. Whether this type of transition occurs inside of cells or contributes to NMIIA-F expansion was unknown. Therefore, we turned to live-cell SIM to monitor the structural and dynamic changes during NMIIA-F stack formation.

We imaged NMIIA motor domains and found 2-motor-group NMIIA-Fs unfolded to become 3-motor-group NMIIA-Fs (Figure 2-2). Surprisingly, only a small percentage (5.3 +/- 2.5%) of 3-motor-group NMIIA-Fs went back or "collapsed" to being a 2-motor-group NMIIA-F, as the "network contraction" model has predicted (Figure 2-2B). The vast majority (85.8 +/- 4.1%) of newly formed NMIIA-F expanded (Figure 2-2). This data indicated the 2, 3, and 4-motor-groups represented distinct structural steps underlying the formation of NMIIA-F stacks. We next wanted to explore the physical mechanisms underlying stack formation.

By increasing our sampling rate to 15 second-intervals, we were able to detect transitional structures between 2 to 3 and 3 to 4 motor-group NMIIA-Fs (Figure 2-2). New motor-groups did not simply appear next to preexisting motor-groups. Instead, a preexisting motor-group extended (Figure 2-2) before the appearance of a new motor-group (Figure 2-2). This data led us to hypothesize, that a subset of NMIIA molecules were moving away from one side of the 2-motor-group NMIIA-F. We also detected this type of extension during the transition between a 3-motor-group to 4-motor-group NMIIA-F (Figure 2-2). In addition, rod domains extended and this occurred with the extension of the first motor-group of a 2-motor-group NMIIA-F (Figure 2-2).

We next used photo-conversion of NMII-A-mEOS2 (Burnette et al., 2014b), labeled on the N-terminal motor domains, to test if NMIIA molecules within filaments were spreading out in space as the extension of the motor-groups revealed by SIM (Figure 2-2) suggested. EOS is a green fluorescent protein, which can be photo-converted to red by exposure to UV light (Wiedenmann et al., 2004). Using this method, we converted NMIIA-mEOS2 at the edge of cells and thus specifically marked NMIIA molecules that were incorporated into NMIIA-Fs (Figure 2-2). A subset of NMIIA-mEOS2 molecules were not converted and allowed us to monitor the expansion of stacks in the green channel (Figure 2-2). Note that the converted pool of NMIIA-mEOS2 also spread out during expansion (Figure 2-2), which is consistent with NMIIA molecules within a NMIIA-F spreading out in space. An alternative interpretation of this result is that converted NMIIA-mEOS2 molecules are being removed from NMIIA-Fs or photo-converted in the cytoplasmic pool and then being added to expanding stacks. While this seems unlikely, as we did not detect incorporation of red-labeled NMIIA-mEOS2 in NMIIA-F outside of the region of conversion during the short time frame of the experiment, we still wanted to confirm NMIIA molecules could change position within individual NMIIA-Fs using another method. In addition, it is important to point out that, as this was done on a wide-field (i.e., diffraction limited) microscope, we can only confidently detect expansion of the larger NMIIA filaments, such as the ones shown in Figure 2-2.

To further test if NMIIA molecules could move within a NMIIA-F, we monitored the precise movements of single molecules of NMIIA-mEOS2 (N-terminal motor domain) within NMIIA-Fs using single particle tracking photo-activated localization microscopy (sptPALM) (Betzig et al., 2006; Manley et al., 2008) (Figure 2). sptPALM allows for the precise localization and tracking of a single molecule, which has been photo-converted from green to red. Using sptPALM, we converted single NMIIA-mEOS2 molecules within NMIIA-Fs at the leading edge of cells, to test if individual NMIIA molecules could spread out in space within a NMIIA-F. To measure this, we drew a mask around the perimeter of a diffraction-limited image of the unconverted mEOS2 molecules (i.e., green channel) within a NMIIA-F for every image in the acquisition. We then tracked the movement of a single converted NMIIA-mEOS2 molecule within this NMIIA-F. Any molecule that moved a diffraction-limited distance (i.e., 250nm) within the NMIIA-F mask, was counted as moving. Indeed, sptPALM data revealed 32.8 +/- 4.3% of single NMIIA-mEOS2 molecules changed their position within their respective NMIIA-F (Figure 2-I). Interestingly, of the moving single NMIIA-mEOS2 molecules, our analysis revealed all but one moved relatively closer to the leading edge by moving slower than the respective expanding NMIIA-F (Figure 2-2). Taken together, our SIM, photo-conversion, and PALM results show the creation of stacks from NMIIA-Fs involved NMIIA molecules spreading out from pre-existing 2-motor-group NMIIA-Fs. We next asked if NMIIA-F stacks formed by other mechanisms.

In vitro experiments have shown rabbit skeletal myosin II can align into stack like orientations in the presence of actin filaments. Mathematical modeling suggested this could arise as a result of distinct myosin II filaments coming closer together by contracting actin filaments (i.e., concatenation) (Stachowiak et al., 2012). To test if concatenation occurs inside of a living cell, we quantified how many NMIIA-Fs moved together (Figure 2-2). We found ~10% of NMIIA-Fs concatenated with other NMIIA-Fs, and this was independent of whether the NMIIA-Fs were expanding (Figure 2-2). Concatenation was defined as two separate NMIIA-Fs aligning their rod domains within 4 pixels (160 nm) of each other (Figure 2-2). Thus, while concatenation did occur at a low rate at the leading edge, most NMIIA-F stacks arose from expansion. However, our data does not preclude network contraction and/or concatenation, as dominant mechanisms of NMIIA-F dynamics in parts of the cell other than the leading edge where NMIIA-F densities were too high for us to resolve individual NMIIA-Fs.

Figure 2-2

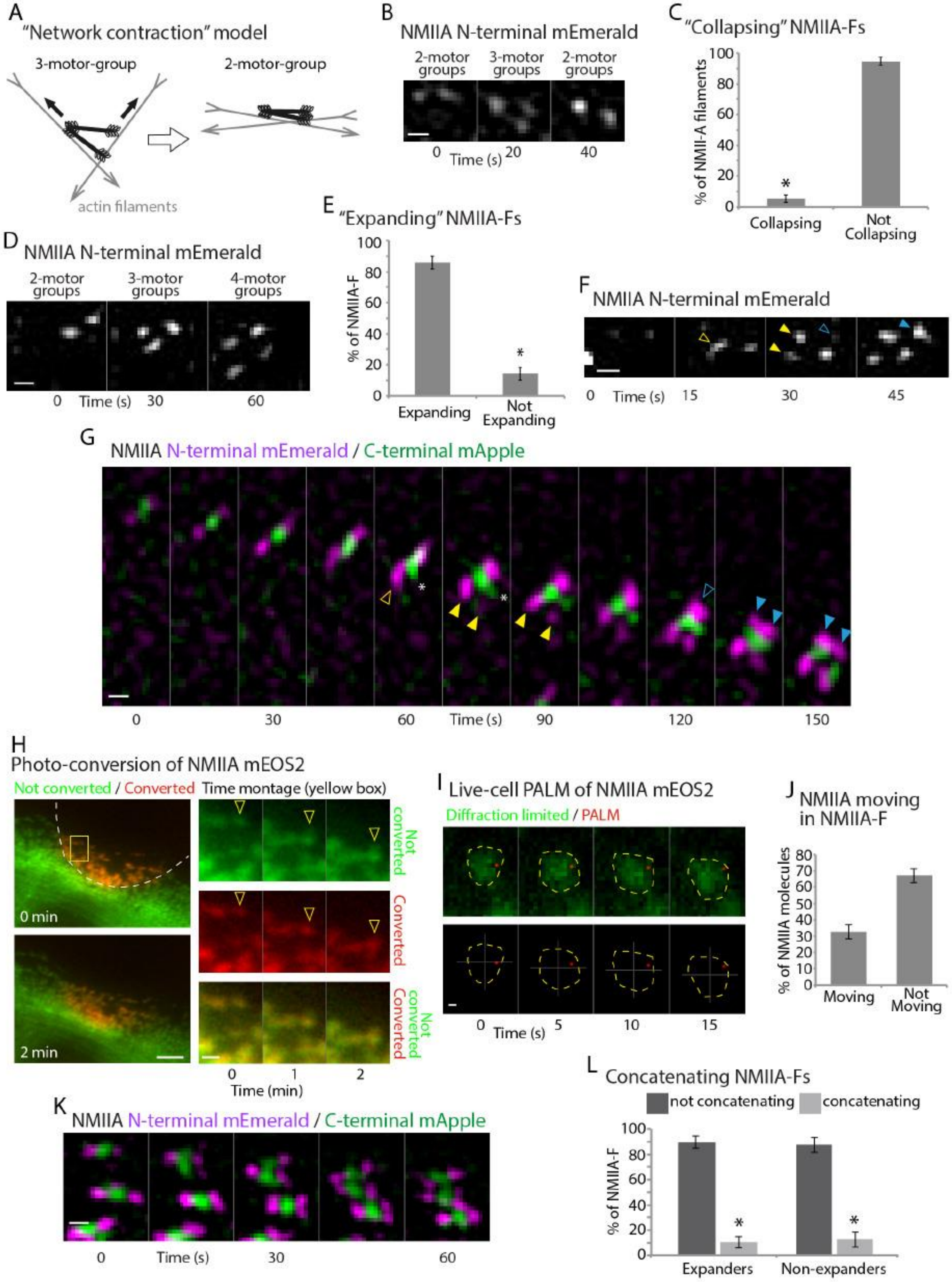
A
"Network contraction" model
3-motor-group
2-motor-group
actin filaments
B
NMIIA N-terminal mEmerald
2-motor groups
3-motor groups
2-motor groups
0
Time (s)
20
40
C
"Collapsing" NMIIA-Fs
% of NMII-A filaments
100
80
60
40
20
0
*
Collapsing
Not Collapsing
D
NMIIA N-terminal mEmerald
2-motor groups
3-motor groups
4-motor groups
0
Time (s)
30
60
E
"Expanding" NMIIA-Fs
% of NMIIA-F
100
80
60
40
20
0
*
Expanding
Not Expanding
F
NMIIA N-terminal mEmerald
0
Time (s)
15
30
45
G
NMIIA N-terminal mEmerald / C-terminal mApple
*
*
0
30
60
Time (s)
90
120
150
H
Photo-conversion of NMIIA mEOS2
Not converted / Converted
Time montage (yellow box)
0 min
2 min
Not converted
Converted
Not converted Converted
0
1
2
Time (min)
I
Live-cell PALM of NMIIA mEOS2
Diffraction limited / PALM
0
Time (s)
5
10
15
J
NMIIA moving in NMIIA-F
% of NMIIA molecules
80
70
60
50
40
30
20
10
0
Moving
Not Moving
K
NMIIA N-terminal mEmerald / C-terminal mApple
0
Time (s)
30
60
L
Concatenating NMIIA-Fs
not concatenating
concatenating
% of NMIIA-F
100
80
60
40
20
0
*
*
Expanders
Non-expanders

Figure 2-2: NMIIA-Fs expand into stacks.

A) Cartoon of the network contraction model showing a 3-motor-group NMII-F transitioning to a 2-motor-group NMII-F by walking towards the barbed ends of actin filaments adapted from Figure 7 of (Verkhovsky et al., 1999b). B) Time montage from a live-cell SIM acquisition of NMIIA-(N-terminal)-mEmerald showing a 2-motor-group NMIIA-F expanding into a 3-motor-group and collapsing to a 2-motor-group NMIIA-F. C) Percent of collapsing (i.e, network contracting) NMIIIA-Fs. D) Time montage of NMIIA-(N-terminal)-mEmerald showing a 2-motor-group NMIIA-F expanding into a 3-motor-group and then to a 4-motor-group NMIIA-F. E) Percent of 2-motor-group NMIIA-Fs that expand. F) Time montage of NMIIA-(N-terminal)-mEmerald from a higher temporal resolution acquisition showing intermediate structures during NMIIA-F expansion. Yellow arrowhead denotes transition between 2-motor-group (open) and 3-motor-group NMIIA-F (closed). Open blue arrowhead denotes transition between 3-motor-group and 4-motor-group NMIIA-F (closed blue arrowhead). G) Time montage from a dual-color acquisition of NMIIA-(N-terminal)-mEmerald/(C-terminal)-mApple showing rod domains expand concurrent with the initial asymmetric expansion of the motor domains (asterisks). H) Photo-converted (red) and unconverted (green) NMIIA-mEOS2 at 0 and 2 minutes after conversion of the leading edge (white dotted line). Time montage from yellow box shows the unconverted (green), converted (red), and overlay. Arrowheads denote expanding NMIIA-F. Note the converted NMIIA-mEOS2 (red) spread out during expansion. I) Time montage showing unconverted NMIIA-mEOS2 (green) and a single converted NMIIA-mEOS2 molecule (red) localized with sptPALM. Yellow dotted line shows boundary of NMIIA-F and crosshairs denote the centroid of the NMIIA-F. The molecule moved 353 +/- 25 nm within the NMIIA-F. Average velocity of converted NMIIA-mEOS2 molecules was 0.75 +/- 0.25 μm/min (~12.5 nm/s). J) Quantification of the number of molecules, which moved in NMIIA-Fs. K) Montage showing a concatenation of expanding NMIIA-Fs into a larger stack. L) Quantification of the percentage of concatenation events 2 μm from the edge. For C, E, and l, N= 211 NMIIA-Fs from 32 cells over 5 independent experiments. For I-J, N= 18 NMIIA molecules from 11 cells over 3 independent experiments. * denotes $P < 0.001$. Scale bars in the low mag and montage of (H), 5 and 1 μm, respectively. All other scale bars, 200 nm. Live-cell 3-D SIM data were acquired by taking 4 images with 125 nm Z steps and creating a maximum projection of each time-point.   All images are oriented with the leading edge towards the top. Error bars in (C), (E), (J), and (L) indicate SEM.

We next wanted to test the molecular mechanisms driving NMIIA-F stack formation. Our data shows that both expansion and concatenation involves the movement of NMIIA-Fs, and movement of NMII-Fs in crawling cells is dependent on NMII motor activity (Wilson et al., 2010). Therefore, we tested if motor activity is required for stack formation by inhibiting the ATPase activity of the NMII motor domain using increasing concentrations of blebbistatin (Straight et al., 2003) (Figure 2-3). Cells treated with 5 μM and 50 μM blebbistatin showed an increased percentage of 2-motor-group NMIIA-Fs compared to control cells (Figure 2-3), while the percentage of 3, 4, and >4-motor-group NMIIA-Fs decreased (Figure 2-3.). Using a low concentration of blebbistatin, 500 nM, we observed the percentage of larger NMIIA-F groups (4 and >4-motor-groups) declined (Figure 2-3), 3-motor-group NMIIA-F percentage remained similar (Figure 2-3), and 2-motor-group NMIIA-F percentage increased, with respect to control cells (Figure 2-3). Thus, NMIIA-F expansion was dependent on NMII motor activity (i.e., either binding to or generating force on actin filaments). Furthermore, even in low concentrations of blebbistatin, NMIIA-Fs could expand, but not to the same extent of cells that maintain full contractile potential.

The decrease in 4 and >4-motor-groups suggested NMIIA-F stack formation was inhibited by blebbistatin. Therefore, we directly quantified stack lengths by measuring the length of the rod domains as localized with a NMIIA specific antibody (Figure 2-3). Consistent with the measured decrease in 4 and >4-motor-group filaments, we found that stack lengths decreased with increasing amounts of blebbistatin. We also inhibited Rho-associated kinase (ROCK) with 10 μM Y-27632 (Uehata et al., 1997), which indirectly reduces NMII contractility, and found a similar decrease in stack lengths as 50 μM blebbistatin (Figure 2-3). Interestingly, the ability to form NMIIA-Fs (e.g., 2-motor-groups) was less sensitive to NMII ATPase inhibition than NMIIA stack expansion. For example, we found 5 μM blebbistatin did not significantly reduce the density of NMIIA-Fs even though it did reduce overall NMIIA-F stack lengths. (Figure 2-3). Importantly, we found the widths of NMIIA-Fs (i.e., motor-group to motor-group across the rod domain) to be similar in all experimental conditions. This is not surprising as the width of NMIIA filaments *in vitro* are also extremely similar (Billington et al., 2013).

To further test if motor activity is required for NMIIA-F stack formation, we expressed either wild type or a N93K mutant NMIIA-mEGFP in a human fibroblast-like cell line with its endogenous NMIIA knocked out with CRISPR/Cas9 (Figure 2-3). The N93K mutant has the ability to bind actin filaments but has reduced motor activity compared to wild type (Hu et al., 2002; Vicente-Manzanares et al., 2007). Consistent with motor activity driving stack formation, we found the N93K mutant NMIIA created shorter stacks with a slight reduction in filament density (Figure 2-3). As NMIIA motors pull on actin filaments, we next tested if the availability of actin filaments could also regulate stack formation.

Figure 2-3

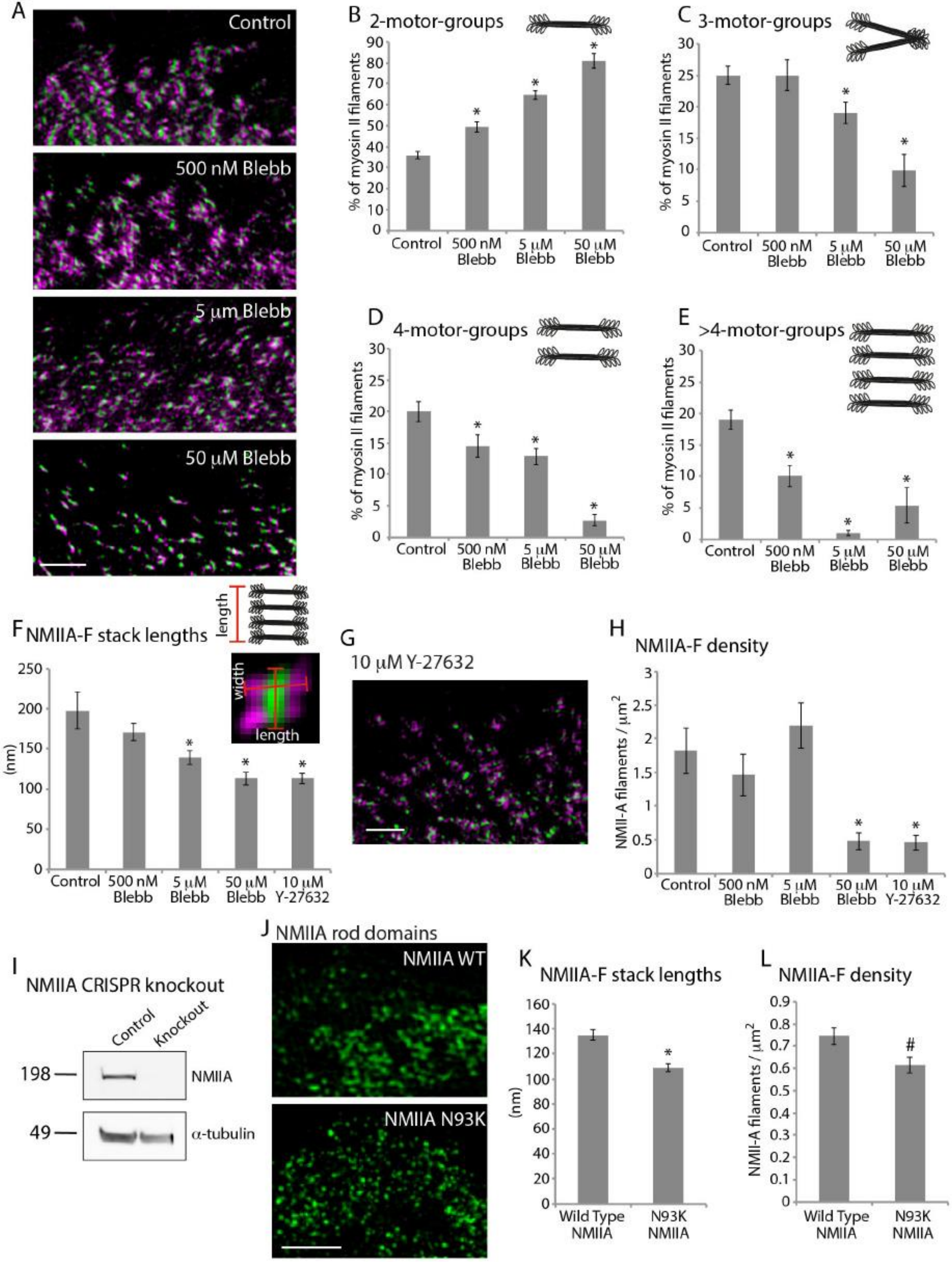
A
Control
500 nM Blebb
5 μm Blebb
50 μM Blebb
B 2-motor-groups
% of myosin II filaments
90
80
70
60
50
40
30
20
10
0
Control
500 nM Blebb
5 μM Blebb
50 μM Blebb
*
C 3-motor-groups
% of myosin II filaments
30
25
20
15
10
5
0
Control
500 nM Blebb
5 μM Blebb
50 μM Blebb
*
D 4-motor-groups
% of myosin II filaments
30
25
20
15
10
5
0
Control
500 nM Blebb
5 μM Blebb
50 μM Blebb
*
E >4-motor-groups
% of myosin II filaments
30
25
20
15
10
5
0
Control
500 nM Blebb
5 μM Blebb
50 μM Blebb
*
F NMIIA-F stack lengths
length
width
length
(nm)
250
200
150
100
50
0
Control
500 nM Blebb
5 μM Blebb
50 μM Blebb
10 μM Y-27632
*
G
10 μM Y-27632
H
NMIIA-F density
NMII-A filaments / μm^2
3
2.5
2
1.5
1
0.5
0
Control
500 nM Blebb
5 μM Blebb
50 μM Blebb
10 μM Y-27632
*
I
NMIIA CRISPR knockout
Control
Knockout
198 —
NMIIA
49 —
α-tubulin
J NMIIA rod domains
NMIIA WT
NMIIA N93K
K
NMIIA-F stack lengths
(nm)
160
140
120
100
80
60
40
20
0
Wild Type NMIIA
N93K NMIIA
*
L
NMIIA-F density
NMII-A filaments / μm^2
0.9
0.8
0.7
0.6
0.5
0.4
0.3
0.2
0.1
0
Wild Type NMIIA
N93K NMIIA
#

Figure 2-3: NMIIA-F expansion requires motor activity.
A) Immuno-localized regulatory light chain (RLC) showing motor-group distribution and NMIIA showing rod-domain localization in control and cells treated with 500nm, 5 μM and 50 μM blebbitstatin for 1 hour. B-E) Distribution of 2 motor-groups (B), 3 motor-groups (C), 4 motor-groups (D), and >4 motor groups (E) in cells treated with increasing amounts of blebbistatin. N= control (225 NMIIA-Fs, 37 cells, 3 experiments); 500 nM blebbistatin (421 NMIIA-Fs, 27 cells, 3 experiments); 5 μM blebbistatin (435 NMIIA-Fs, 32 cells, 3 experiments); 50 μM blebbistatin (237 NMIIA-Fs, 20 cells, 3 experiments). See Methods and Fig. S3-1 for a detailed description of analysis. F) Length of NMIIA-F stacks as measured from the NMIIA rod-domain localization in cells treated with increasing amounts of blebbistatin and 10 μM Y-27632 (ROCK inhibitor). N= control (9145 NMIIA-Fs, 48 cells, 3 experiments); 500 nM blebbistatin (5807 NMIIA-Fs, 38 cells, 3 experiments); 5 μM blebbistatin (11049 NMIIA-Fs, 48 cells, 3 experiments); 50 μM blebbistatin (1873 NMIIA-Fs, 37 cells, 3 experiments); 10 μM Y-27632 (1357 NMIIA-Fs, 28 cells, 3 experiments). See Methods and Fig. S3-2 for a detailed description of analysis. G) RLC/NMIIA rod-domains in a cell treated with 10 μM Y-27632 for 1 hour. H) Density of NMIIA-Fs. N is the same as (F). I) Western showing the absence of NMIIA from Hap1 knockout cells compared to control (Fig. S3-3). J) NMIIA rod domains localized in knockout Hap1 cells either expressing wild type N93K NMIIA. K) Length of NMIIA-F stacks in Hap1 knockout cells transfected with either wild type or N93K NMIIA. L) Density of NMIIA-Fs in Hap1 knockout cells transfected with either wild type or N93K NMII. * denotes P < 0.001, and # denotes P < 0.05 compared to control. Scale bars, 2 μm. Error bars in (B)-(E), (F), (H), (K), and (L) indicate SEM.

To test if the availability of actin filaments regulated NMIIA stack formation, we sought a way to reduce actin filament density. Therefore, we treated cells with Cytochalasin B (CB), a molecule that binds to the plus end of actin filaments and thus reduces the rate of actin filament polymerization (MacLean-Fletcher and Pollard, 1980; Smith et al., 1967). High concentrations of CB (i.e., 1-5 μM) can inhibit the majority of actin filament polymerization and result in the removal of most of the actin filament cytoskeleton (Forscher and Smith, 1988). However, sub-saturating concentrations of CB have been shown to remove specific populations of actin filaments, such as the actin bundles that make the core of filopodia in neuronal growth cones (Burnette et al., 2007). Therefore, we tested several concentrations of CB and found that 100 nM specifically and significantly reduced the actin filaments in the region where NMIIA-F form (i.e., right behind the protrusive lamellipodium (Figure 2-4) with no effect on the amount of actin filaments in the protrusive lamellipodium (Figure 2-4). Furthermore, cells treated with 100 nM CB also had a significant reduction in NMIIA-F stack lengths (Figure 2-4). These results were consistent with the concept that actin filament densities regulate the ability of NMIIA-Fs to expand into stacks. Together, our data supports a model in which NMIIA molecules split from a NMIIA-F through the interactions of motor domains and actin filaments. We next tested if the formation of contractile systems in other cellular contexts could also involve NMIIA-F expansion.

Figure 2-4

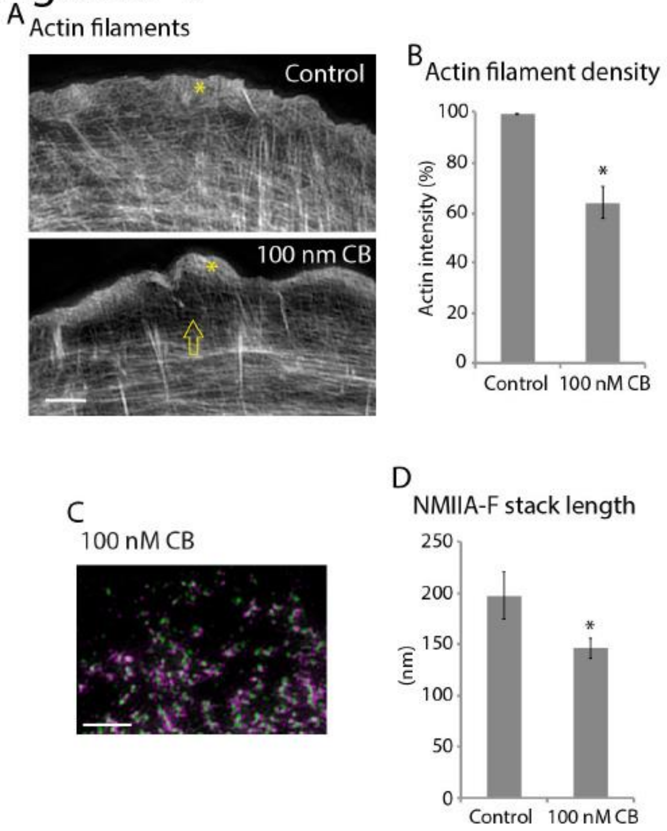

Figure 2-4: Reducing actin filament density reduced NMIIA-F stacks
A) Actin filaments in a control U2-OS cell and a cell treated with 100 nM CB for 1 hour. Arrow denotes the drop in intensity behind the lamellipodium. B) Quantification of the drop in intensity of actin filaments treated with 100 nM CB compared to control. N= control (3 measurements each from 42 cells over 3 experiments); 100nm CB (3 measurements each from 46 cells over 3 experiments). C) RLC/NMIIA rod-domains in a cell treated with 100 nM CB for 1 hour. D) Lengths of NMIIA-Fs in control cells and cell treated with 100 nM CB. N= control (9145 NMIIA-Fs, 48 cells, 3 experiments); 100 nm CB (925 NMIIA-Fs, 20 cells, 3 experiments). * denotes $P < 0.001$ compared to control. Scale bars, 2 μm. Error bars in (B) and (D) indicate SEM.

NMII is largely responsible for the forces driving ingression of the cleavage furrow during cytokinesis of vertebrate cells (Ma et al., 2012; Straight et al., 2003). Furthermore, there is electron microscopy evidence from both classic and recent studies that strongly suggest the presence of NMII stacks in the cleavage furrow (Ong et al., 2014; Sanger and Sanger, 1980). NMIIA is recruited to the membrane of dividing cells during the transition between anaphase and telophase, and this recruitment is followed by cleavage furrow ingression (Matsumura et al., 1998). We started by confirming this using spinning disk confocal microscopy of dividing HeLa cells expressing NMIIA-(N-terminal)-mEGFP and Histone 2B-mCherry to visualize chromosomes (Figure 2-5). As expected, NMIIA-(N-terminal)-mEGFP localized to the membrane at the cleavage furrow during ingression (Figure 2-5). We next tested if there were similar NMIIA-F dynamics (e.g., expansion) during contractile ring formation in HeLa cells as we found at the leading edge of crawling U2-OS cells.

To test if there was NMIIA-F expansion in the cleavage furrow, we acquired high-resolution time-lapse images of NMIIA-(N-terminal)-mEGFP of the very bottom of the forming contractile ring (Figure 2-5). We observed NMIIA-Fs both expanded and also lined up creating NMIIA-F stack-like arrays (Figure 2-5). To confirm the presence of NMIIA-F stacks, we imaged the motor domains with NMIIA-(N-terminal)-mEmerald and rod domains with an antibody in the cleavage furrow using SIM. Indeed, HeLa cells had prominent NMIIA-F stacks spanning the cleavage furrow (Figure 2-5). NMIIA-Fs within stacks were organized parallel to the division plane and the lengths of stacks were perpendicular to the division plane, consistent with a model wherein the furrow closes through a purse-string mechanism. Interestingly, the NMIIA-F stack lengths in the cleavage furrow of HeLa cells were the same as at the leading edge of U2-OS crawling cells (Figure 2-5). Taken together, this data shows NMIIA-F expansion occurs in the cleavage furrow and results in a similar organization as found at the leading edge of a crawling cell during interphase.

We next wanted to determine if NMIIA-F stacks formed in the cleavage furrow by similar mechanisms as at the leading edge. Since NMIIA-F stack length in interphase cells can be modulated by varying the concentration of blebbistatin (Figure 2-3), we analyzed the effect of treating cytokinetic cells with a concentration of blebbistatin that would not halt furrow ingression. As expected, a high concentration of blebbistatin (50 μM) stops furro2-w ingression (Straight et al., 2003) (Figure 2-S5). Cells treated with 20 μM blebbistatin, however, had significantly slower ingression rates, but still divided (Figure 2-S5). Therefore, we used SIM to image and then quantify the NMIIA-F stack lengths in the cleavage furrows of control cells and those treated with 20 μM blebbistatin. Cells treated with 20 μM blebbistatin showed a decrease in overall NMIIA-F stack length (Figure 2-5), even though the numbers of filaments as defined by the numbers of rod localizations was not significantly different (Figure 2-5). Thus, the same number of NMIIA-Fs formed but they failed to elongate into stacks. Thus, NMIIA-F stack formation was sensitive to NMII ATPase inhibition in both interphase and mitosis.

Figure 2-5

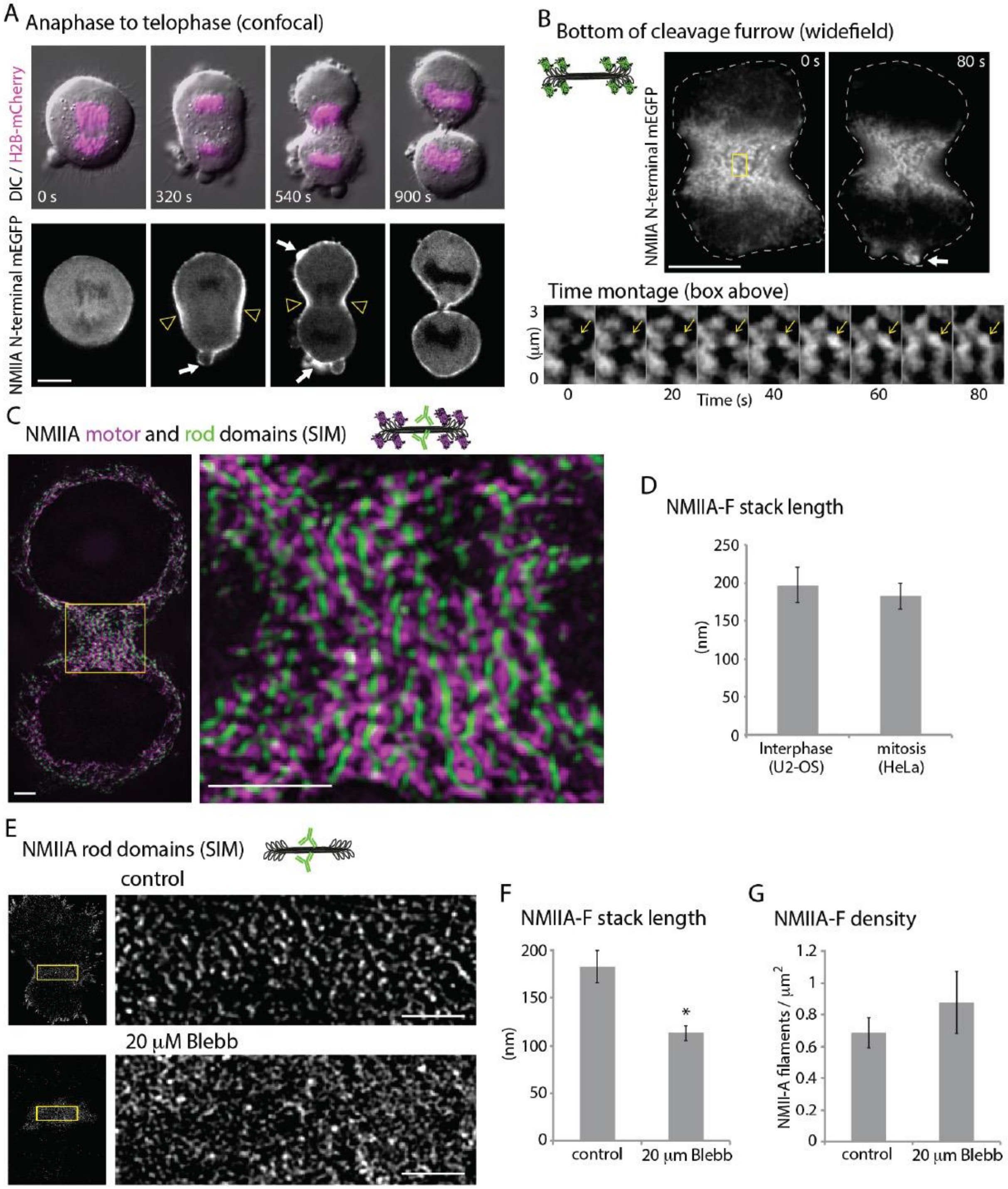

Figure 2-5: NMIIA-F stacks expand in the cleavage furrow

A) Time-lapse montage of DIC and confocal section showing H2B-mCherry (magenta) and NMIIA-(N-terminal)-mEGFP in a HeLa between anaphase and G1. NMIIA accumulation occurs at the membrane from anaphase to telophase (yellow arrowheads). Arrows show NMIIA at sites of blebbing. B) Time-lapse widefield epi-fluorescence imaging of NMIIA-(N-terminal)-mEGFP at the bottom of the cleavage furrow. Time-montage from the yellow box shows NMIIA-F expansion (yellow arrow). Note that expanding NMIIA-Fs appear to align into larger stacks. C) SIM of NMIIA-(N-terminal)-mEmerald and immuno-localized NMIIA rod domains. Whole cell and zoomed view of the cleavage furrow. D) Stack lengths at the leading edge of U2-OS (N= 9145 NMIIA-Fs, 48 cells, 3 experiments) and cleavage furrow of HeLa (N= 362 NMIIA-Fs, 11 cells, 8 experiments) cells. E) SIM of immuno-localized NMIIA rod domains in a control and 20 μM blebbistatin treated cleavage furrow. Note the loss of linear structures in the 20 μM treated furrow. F-G) Length of NMIIA-F stacks (F) and density of NMIIA-Fs (G) in the cleavage furrow of control cells (N= 362 NMIIA-Fs, 11 cells, 8 experiments) and cell treated with 20 μM Blebbistatin (N= 94 NMIIA-Fs, 5 cells, 3 experiments). * denotes $P < 0.001$ compared to control. Scale bars: (A), (B) and, 10 μm; (C) and (E), 2 μm. Error bars in (D), (F), and (G) indicate SEM.

Discussion

We present evidence for a new model of NMIIA stack formation that occurs at both the leading edge of crawling cells and in the cleavage furrow of dividing cells. Through a combination of high and super-resolution light microscopy techniques, we show that NMIIA stacks form from 2 non-mutually exclusive mechanisms, expansion and concatenation (Figure 2-2). Pharmacological and genetic perturbations showed that NMIIA motor activity, cellular contractility, and actin filament availability regulate NMIIA stack formation (Figures 2-3 and 2-4). Furthermore, we show that a slowing of cleavage furrow ingression is associated with a loss of large organized NMIIA stacks. As such, NMIIA filament expansion and concatenation could represent a universal mechanism of contractile unit assembly.

The initial steps of NMIIA-F formation have been well characterized (Vicente-Manzanares et al., 2009a). Auto-inhibited NMIIA molecules become polymerization competent through phosphorylation (Figure 2-6), and form a 2-motor-group filament through electrostatic interactions of their rod domains (Figure 2-6) (Craig et al., 1983; Pollard, 1975; Ricketson et al., 2010) (Pollard, 1975; Ricketson et al., 2010). Steric hindrance limits the number of NMII molecules that can be added to a growing 2-motor-group NMIIA-F (Billington et al., 2013; Pollard, 1975). Thus, a likely role for the formation of NMIIA-F stacks would be to circumvent this inherent limitation in order to create stronger contractile units. Our data shows that NMIIA-F stacks form by both a single 2-motor-group NMIIA-F expanding and by concatenating of multiple NMIIA-F/NMIIA-F stacks (Figure 2-6). During expansion, NMIIA molecules within a NMIIA-F spread out in space (cartoon in Figure 2-6 and Figure 2-2). We envision “pioneer” myosins could move relative to the filament in a number of mechanisms. Pioneers are seemingly left behind by moving slower than other NMII molecules in the NMIIA-F (Figure 2-2). This could be a result of either binding more strongly to actin filaments, walking along actin filaments (i.e., as NMIIB is capable of) (Nagy et al., 2013; Norstrom et al., 2010), or by being pulled out by another molecular motor. The spreading out of the original NMIIA molecules is accompanied by addition of new NMIIA molecules to the growing stack (Figure 2-6) as revealed in our live-cell data by an increase in fluorescent signal during expansion (Figure 2-1 and 2-2).

Figure 2-6

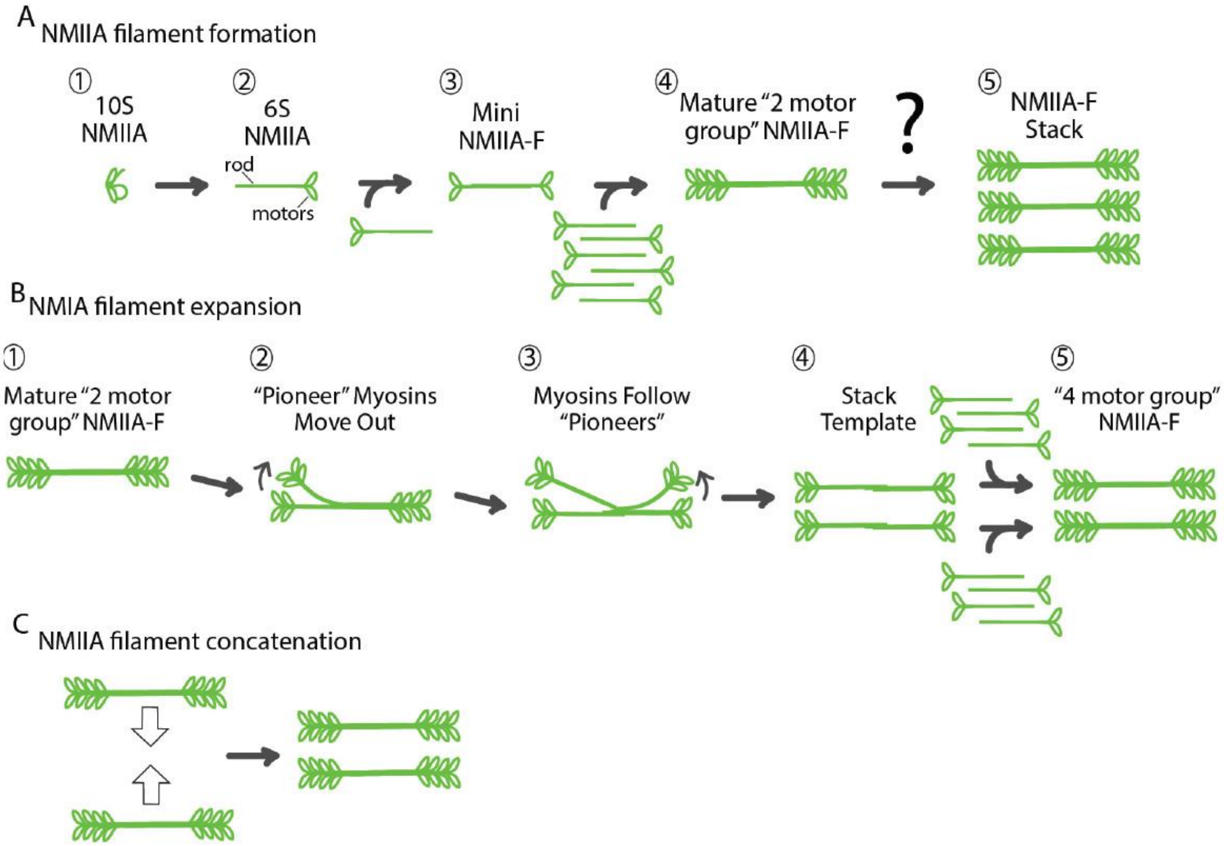

Figure 2-6: Model of NMIIA-F stack formation
A) Classic model of the formation of a 2-motor-group NMIIA-F. An auto-inhibited NMIIA molecule (1) becomes polymerization competent (2) after phosphorylation of its regulatory light chain. Two polymerization competent NMIIA molecules then form a mini NMIIA-F (3) through electrostatic interactions of their rod domains. Addition of more NMIIA molecules to the mini-filament drives the growth of a 2-motor-group NMIIA-F (4). Steric hindrance limits the number of molecules that can be added to 2-motor-group NMIIA-F(Billington et al., 2013). Note a smaller number of myosins than the ~15 on each side of the filament are drawn for simplicity. Importantly, how larger contractile arrays (i.e., stacks) containing more myosins capable of generating more contractile forces is not understood (5). B) Model of NMIIA-F expansion. After the formation of a 2-motor-group NMIIA-F (1), a subset of "pioneer" myosins separate themselves from one side of the filament (2). "Pioneer" myosins are then followed by myosins from the other side of the filament (3) to create a template for a stack (4). Growth of these templates is driven by

addition of new NMIIA molecules (5). We have drawn this addition at the end for simplicity, but it could occur as soon as the “pioneer” myosins have separated themselves enough from the 2-motor-group NMIIA-F to fit in new molecules as in (2). C) Stacks can also form through concatenation of multiple NMIIA-Fs. Expansion and concatenation are not mutually exclusive as expanding NMIIA-Fs can concatenate with other NMIIA-Fs as in Fig. 2K.

Exactly why expansion of NMIIA filaments occurs, as opposed to only addition of NMIIA molecules from a soluble cytoplasmic pool adjacent to a 2-motor group filament isn't currently understood, but our data points to a few plausible explanations. Previous data has shown that a majority of NMIIA molecules are in a soluble, un-polymerized pool (i.e., not in a bipolar filament) (Breckenridge et al., 2009; Shutova et al., 2012). In addition, a finite number of NMIIA molecules make up an individual NMIIA bipolar filament before steric hindrance restricts addition of more NMIIA molecules (Billington et al., 2013; Niederman and Pollard, 1975; Pollard, 1975). Thus, expansion and separation of a NMIIA 2-motor group filament would reduce steric hindrance in the filament and allow for addition of more NMIIA molecules, increasing the force generating capabilities of the ensemble. Continued expansion and addition would result in larger NMIIA ensembles (i.e., a NMIIA stack). This mechanism would conceivably be more efficient than polymerizing a 2-motor group filament "de novo" adjacent to a previously formed 2-motor-group filament.

Surprisingly, we found that only a small percentage of NMIIA filaments exhibit a network contraction like behavior (Figure 2-2) (Verkhovsky et al., 1999b). Despite this small percentage, we do not rule out a role for this population of NMIIA filaments in either crawling or dividing cells, or other cellular contexts. For example, this small percentage of NMIIA filaments could be locally remodeling actin filaments at the leading edge of crawling cells, just as the network contraction model has predicted. The larger percentage of expanding NMIIA filaments could be involved in NMII required processes, such as adhesion maturation and actin arc translocation, all of which are required for efficient cell migration (Medeiros et al., 2006; Vicente-Manzanares et al., 2007).

NMIIA-F stacks have inherently more NMIIA molecules within them than nascent 2-motor-group filaments. Thus, stacks are likely to be able to generate more force. This may be vital to the function of the sarcomere-like stress fibers driving the movement of crawling and the separation of dividing cells (Figure 2-S4) (Burnette et al., 2014b; Sanger and Sanger, 1980; Verkhovsky et al., 1995). Another possible role for NMIIA-F stack formation could be to template the formation of other myosin isoforms with different biophysical properties, such as NMIIB, which has been shown to incorporate into NMIIA-Fs over time (Beach et al., 2014; Shutova et al., 2014). Indeed, we found reducing NMIIA in U2-OS cells with RNAi does tend to abolish NMIIB filament stacks (Fig. S6).

Our SIM analysis of NMIIA organization in cleaving cells also provides insight into the force generating machinery that drives cytokinesis. Constriction of an annular actomyosin array is arguably the dominant model in the field, but other models are equally plausible (Eggert et al., 2006; Wang, 2005). Debate has continued in part because we lack information on how actomyosin is arranged within the cleavage furrow. In fission yeast, this problem was addressed through electron microscopic analysis of time-dependent changes in the three-dimensional arrangement of F-actin throughout cytokinesis (Kamasaki et al., 2007). Consistent with a purse string mechanism, actin filaments circumscribe the cortex, forming a circular structure composed of filaments oriented parallel to the plane of division. Our data clearly show that furrow NMIIA forms stacks that orient perpendicular to the plane of division (Figure 2-5), suggesting that they slide an array of actin filaments that are also arranged in parallel relative to the direction of ingression. Interestingly, the stack length and density of NMIIA correlate with the speed of ingression (Figure 2-5). Thus, although our analysis does not formally prove that furrow localized NMIIA generates the forces that drive cell cleavage, they are consistent with the notion that cytokinesis in human cells is also driven by a purse string mechanism.

Supplemental figures

Figure 2-S1

A RLC and NMIIA-(N-terminal)-mApple

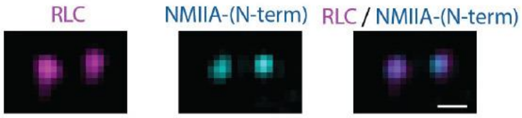

B
Endogeous RLC and NMII-A rod domains

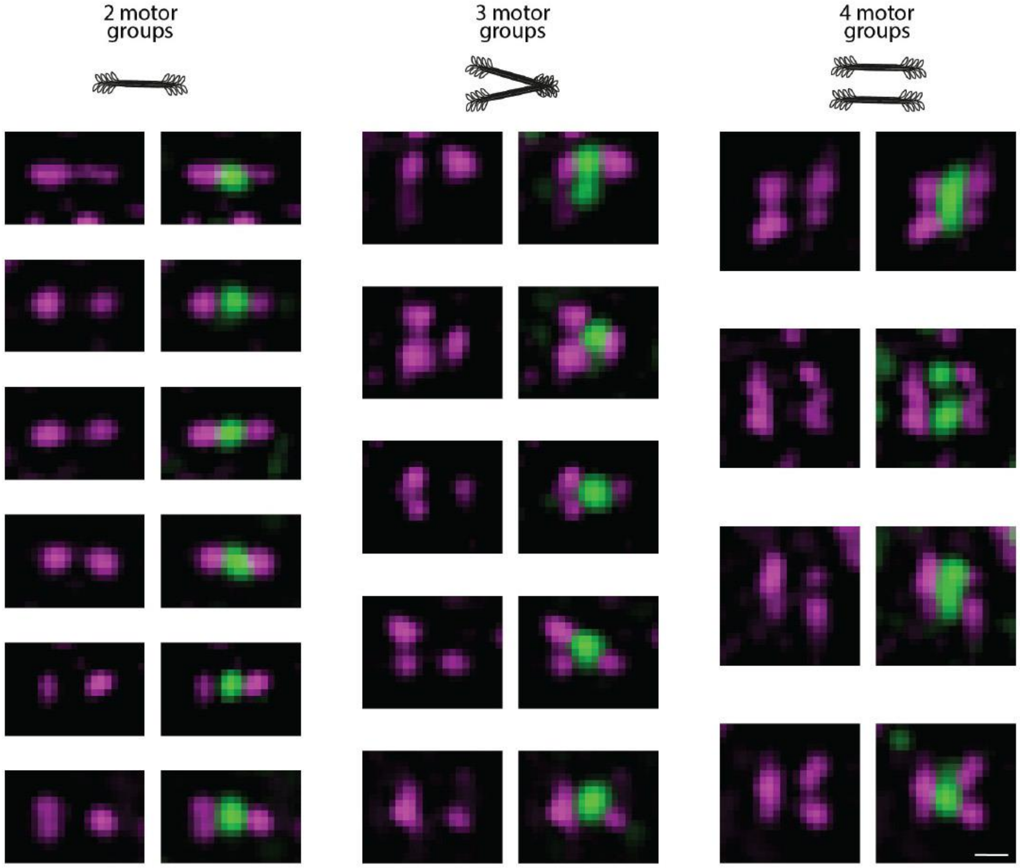

Figure 2-S1: Endogenous NMIIA-F organization
A) SIM of RLC (magenta) and NMIIA-(N-terminal)-mApple motor domains (green). Signal from RLC channel aligns with NMIIA-(N-terminal)-mApple motor domains, and thus can be used to quantify motor domains. B) Examples of 2-motor-group, 3-motor-group, and 4-motor-group NMIIA-Fs at the leading edge of crawling U2-OS cells. Scale bars, 200 nm.

Figure 2-S2

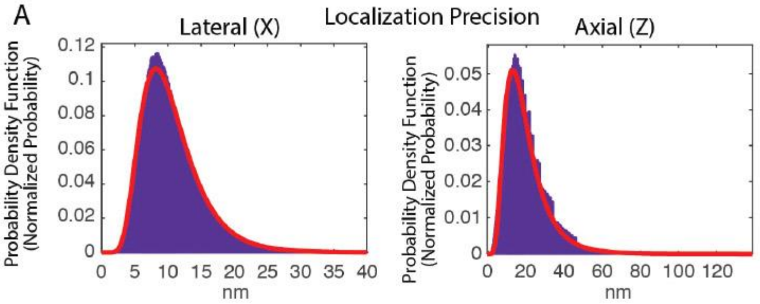

B 2-motor-group filaments from Figure 1I

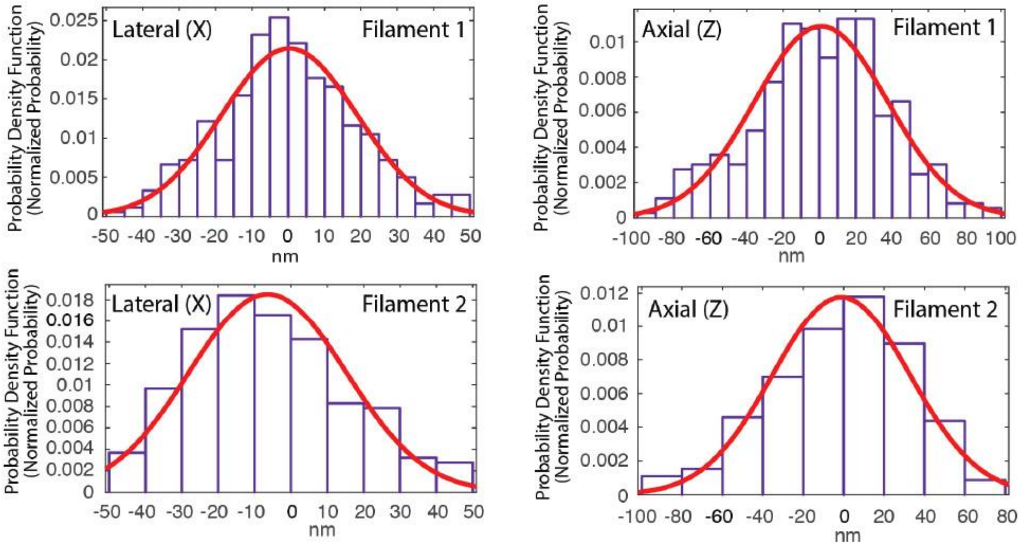

C 3-motor-group filaments from Figure 1J

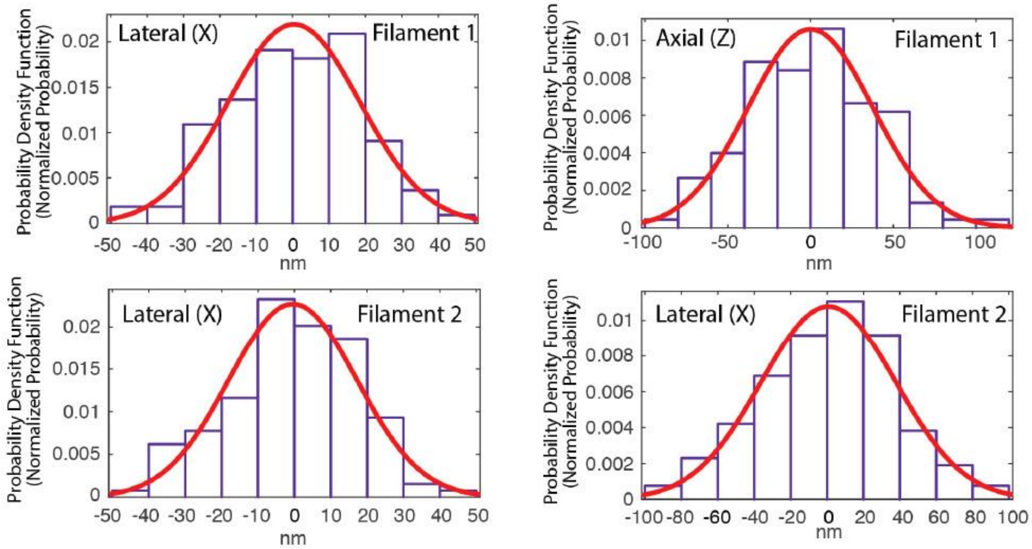

Figure 2-S2: Spatial distributions and localization precision of NMIIA-mEOS 3D-PALM measurements.
A) Localization precision for all NMIIA-mEOS2 molecules detected within a cell. The mean of the localization precision was extracted from a lognormal fit to the histogram distribution ($\boldsymbol{\mu}_\mathbf{z}$ = 20 +/- 11 nm and $\boldsymbol{\mu}_\mathbf{x}$ = 11+/- 5 nm; error represents S.D.). B) Representative histogram distributions of individual NMIIA-mEOS2 localized within clusters from 2-motor-group filament. Isolated clusters of NMIIA-mEOS2, interpreted to represent NMIIA motor groups, were segmented, normalized to their respective means, and quantified along X and Z spatial dimensions. Histograms were fit to a normal distribution model and the standard deviation was extracted (σ). Cluster dimensions for Filament 1 were $\boldsymbol{\sigma}_\mathbf{x}$ = 19 and $\boldsymbol{\sigma}_\mathbf{z}$ = 37 nm and for Filament 2 were $\boldsymbol{\sigma}_\mathbf{x}$ = 22 and $\boldsymbol{\sigma}_\mathbf{z}$ = 34 nm. C) Representative histogram distributions of individual NMIIA-mEOS2 localization clusters from 3-motor-group filament. Isolated clusters of NMIIA-mEOS2, interpreted to represent NMIIA motor groups, were segmented, normalized to their respective means, and quantified along X and Z spatial dimensions. Histograms were fit to a normal distribution model and the standard deviation was extracted (σ). Cluster dimensions for Filament 1 were $\boldsymbol{\sigma}_\mathbf{x}$ = 18 and $\boldsymbol{\sigma}_\mathbf{z}$ = 38 nm and for Filament 2 were $\boldsymbol{\sigma}_\mathbf{x}$ = 18 and $\boldsymbol{\sigma}_\mathbf{z}$ = 37 nm.

Figure 2-S3

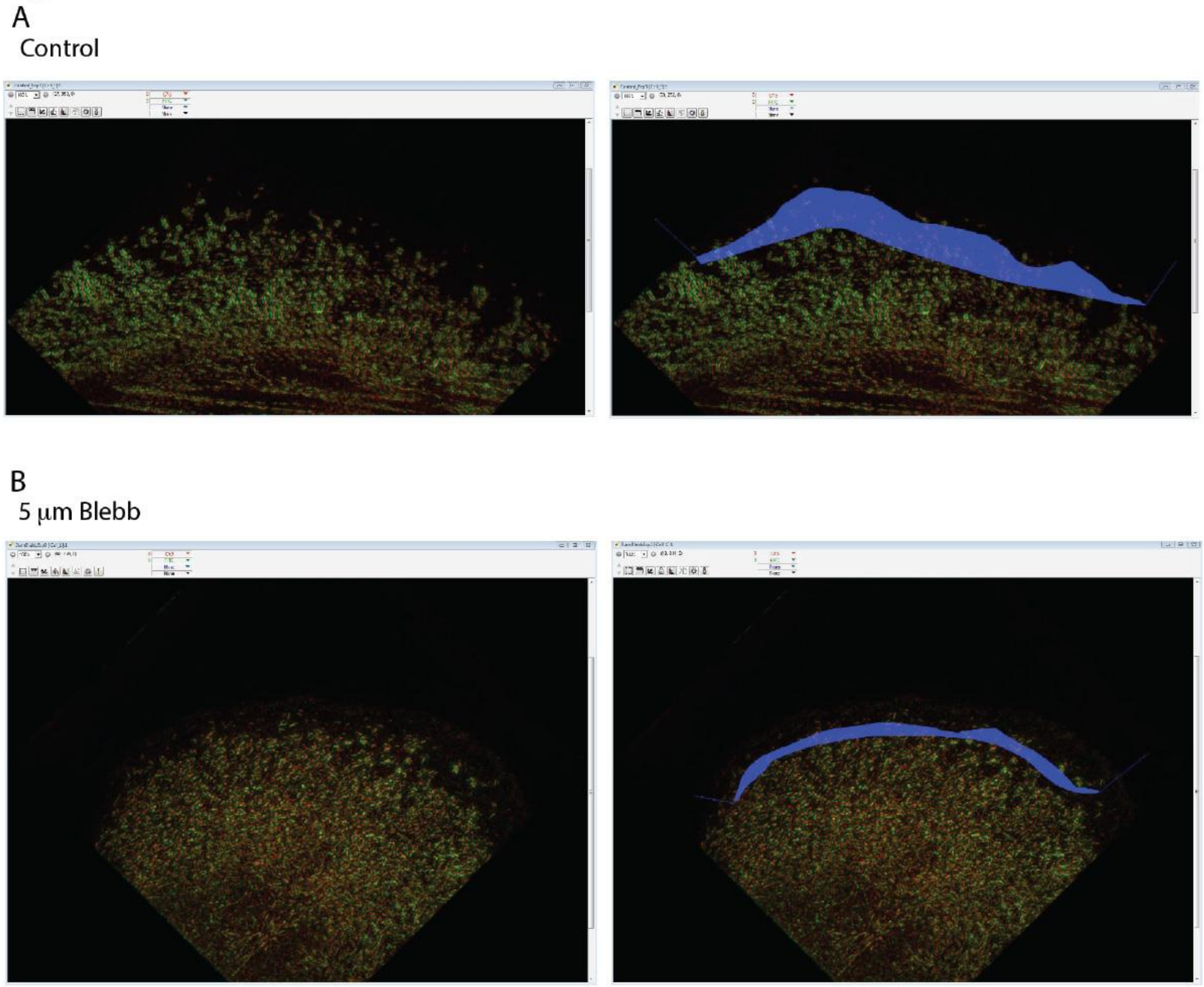

Figure 2-S3: Defining region for 2, 3, 4, and >4 motor-group NMIIA-Fs
Actual screen shots of data analyzed in Slidebook from cells visualized by endogenous RLC (green) and NMIIA (red). A) Left screen shot shows a control cell without the region in which 2, 3, 4, >4 motor-group NMIIA-Fs were quantified. A) Right screen shot shows the same control cell with the region in which 2, 3, 4, >4 motor-group NMIIA-Fs were quantified. NMIIA-Fs were quantified above the blue shaded area. Region was made by measuring 1.5 µm towards cell body from the first visualized NMIIA-Fs along the edge of a migrating cell. Width of blue shaded area did not factor into quantification. B) Left screen shot shows a cell treated with 5 µm blebbistatin before quantification, and the right screen shot shows the same cell including the region (blue shaded area), above which 2, 3, 4, >4 motor-group NMIIA-Fs were quantified.

Figure 2-S4

A

Control

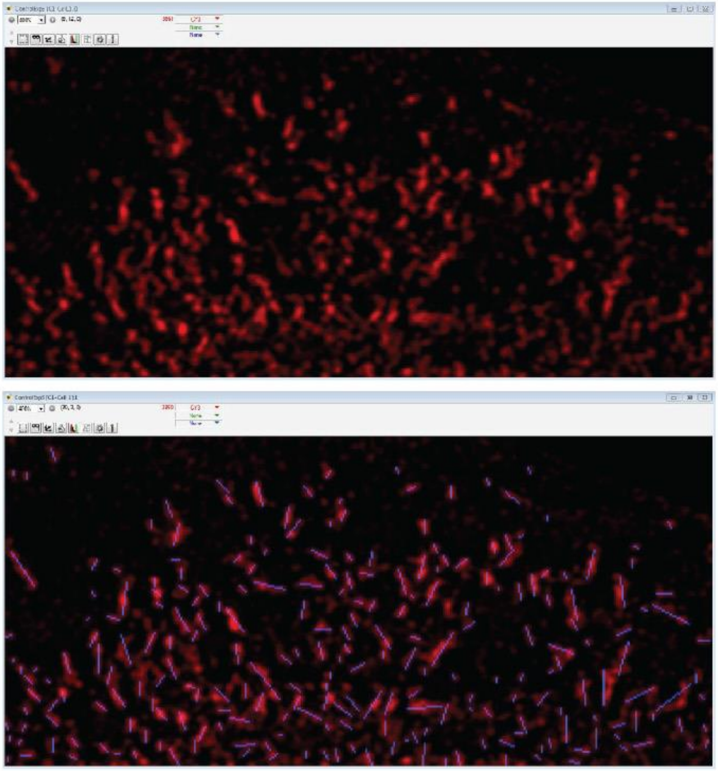

B

5 µm Blebb

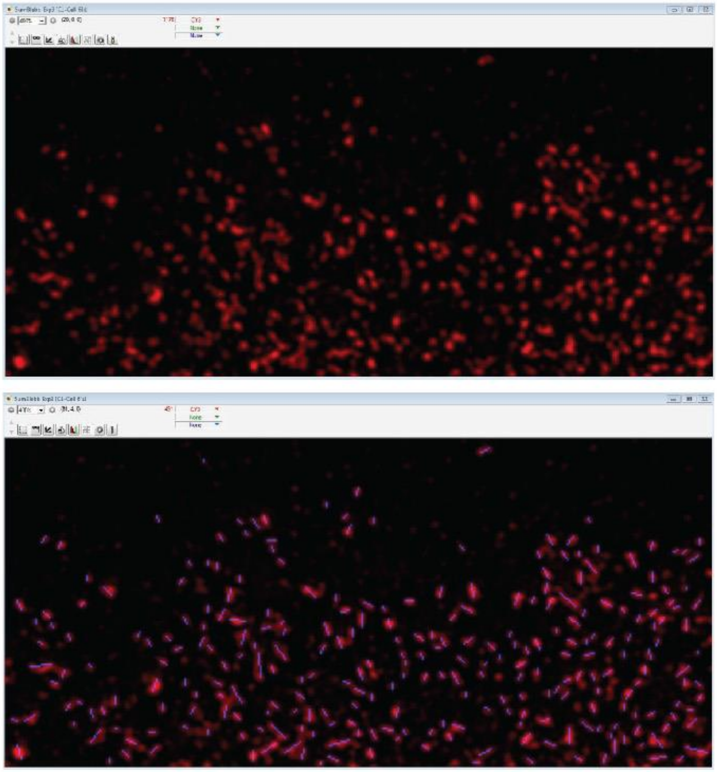

Figure 2-S4: Measuring NMIIA-F stack length
A 15x7 μm region was used to crop cells visualized by endogenous NMIIA (red), starting at the first visualized NMIIA-F. Shown are screen shots from Slidebook, as in Fig. S3-1. a) Top screen shot shows the cropped region of a control cell. Bottom screen shot shows the same cell, including a mask of all NMIIA-Fs (blue lines), which give the number of overall NMIIA-Fs, and length of each filament. b) Top screen shot shows the cropped region of a cell treated with 5 μM blebbistatin. Bottom screen shot shows the same cell including a mask of all NMIIA-Fs (blue lines), which give the length and number of overall NMIIA-Fs.

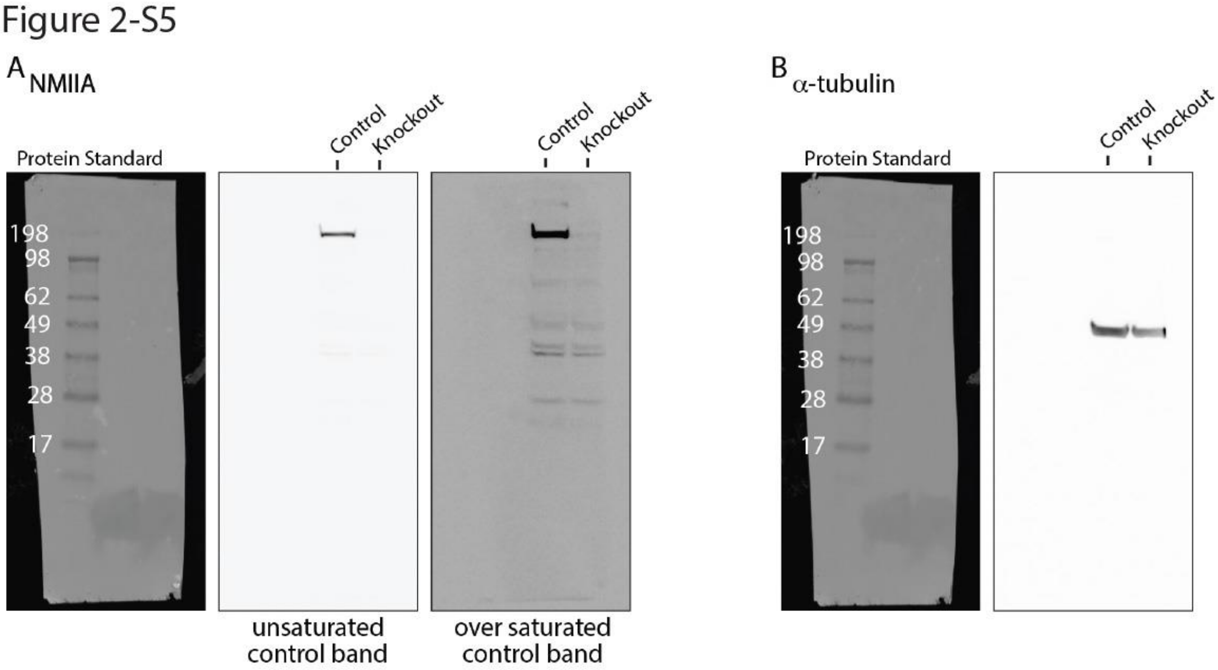

Figure 2-S5: Western blot analysis of HAP1 NMIIA knockout cells
A) Cell lysates from control and myosin IIA knockout cells probed for NMIIA. Control cells show a prominent band at ~200kD corresponding to NMIIA heavy chain, while knockout cells lack this band. B) α-tubulin loading control from the same gel as (A).

Figure 2-S6

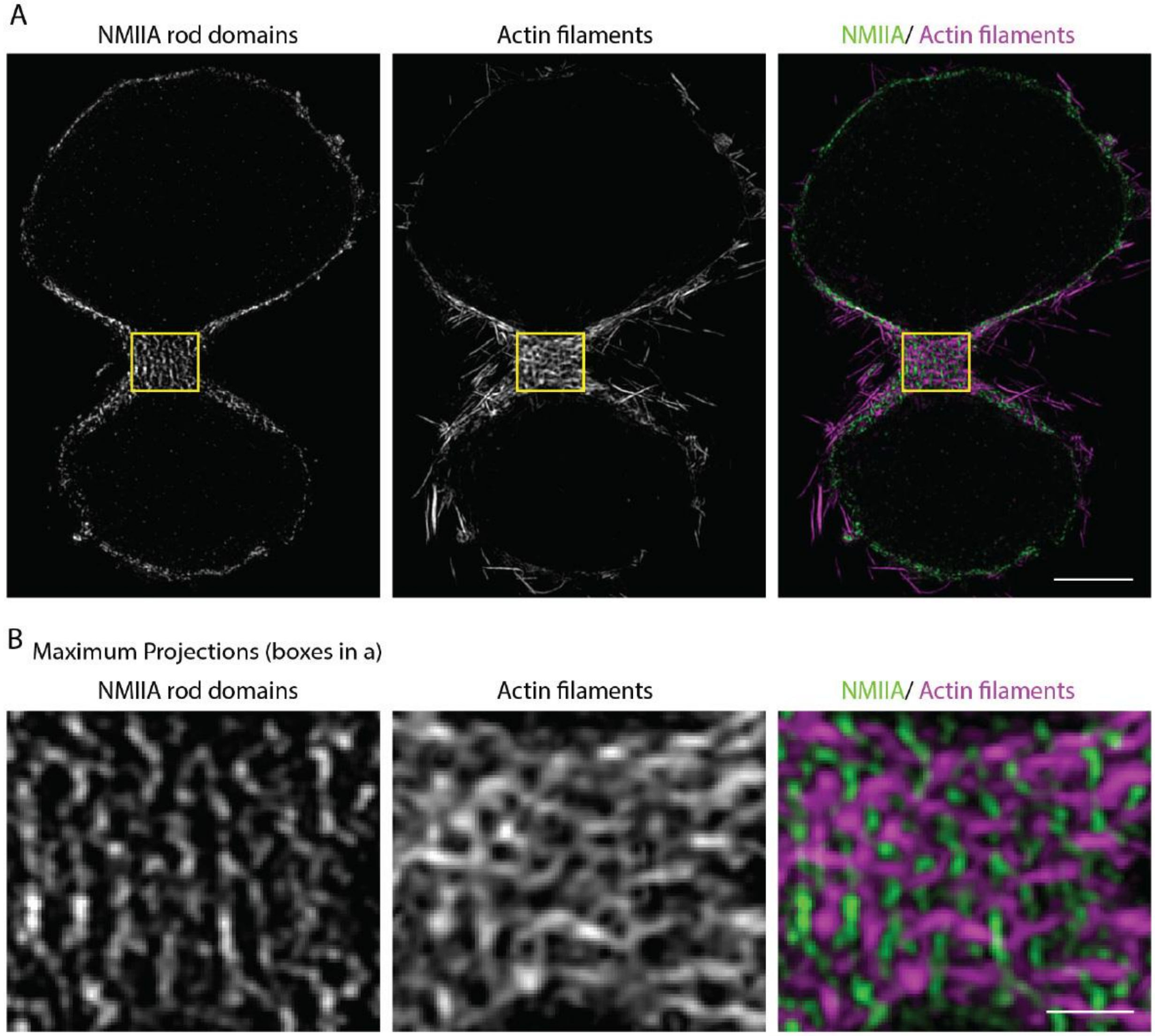

Figure 2-S6: Relative NMIIA-Fs and actin filament bundles in the cleavage furrow A) Whole cell view of endogenous NMIIA rod domains, actin filaments (visualized with phalloidin), and overlay of NMIIA rod domains (green) and actin filaments (magenta) at the bottom of a cleavage furrow in a HeLa cell. B) High mag views of the boxes in (A). Note the positions of actin filament bundles are consistent with published electron microscopy data(Sanger and Sanger, 1980). In addition, the NMIIA filaments and actin bundles resemble the sarcomere-like organization of the stress fibers at the leading edge of U2-OS cells (Burnette et al., 2014b). This cell was fixed with 4% paraformaldehyde without live-cell extraction (i.e., the same protocol as used for U2-OS cells) as the unlabeled phalloidin in the extraction buffer interfered with labeling with fluorescent Alexa-488 phalloidin. Scale bars: (a), 5 μm; (b), 1 μm.

Figure 2-S7

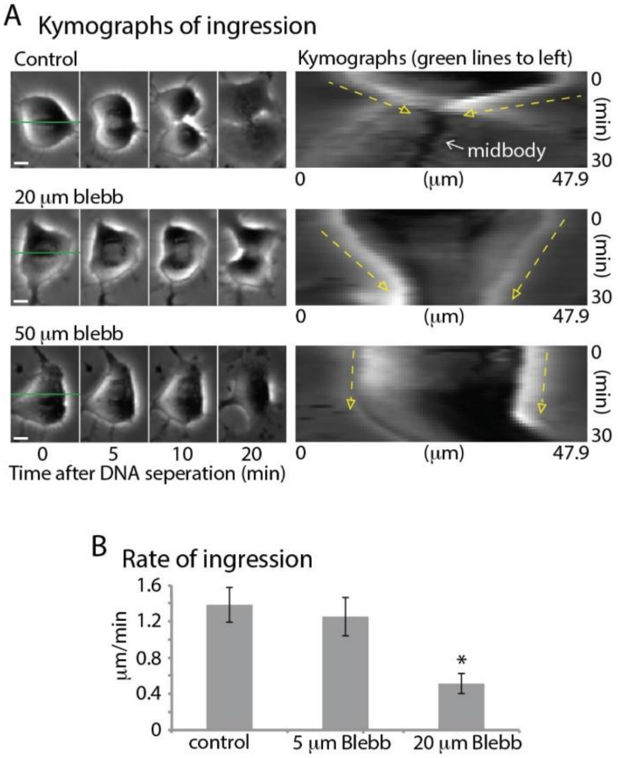

Figure 2-S7: Rates of cleavage furrow ingression during cell division
A) Phase contrast time-montages of control, 20 μM blebbistatin, 50 μM blebbistatin treated cells during. First frame is the time-point before chromosome separation. Kymographs showing ingression rates were created from the lines indicated in the first frame. Arrows in kymographs show ingression. Kymographs were created with Nikon Elements. B) Rates of ingression for control cells (N = 43 cells, 3 experiments), cells treated with 5 μM blebbistatin (N = 37 cells, 3 experiments), and cells treated with 20 μM blebbistatin (N = 36 cells, 3 experiments). * denotes $P < 0.001$. Scale bars, 10 μm.

Figure 2-S8

A NMIIA rod domains

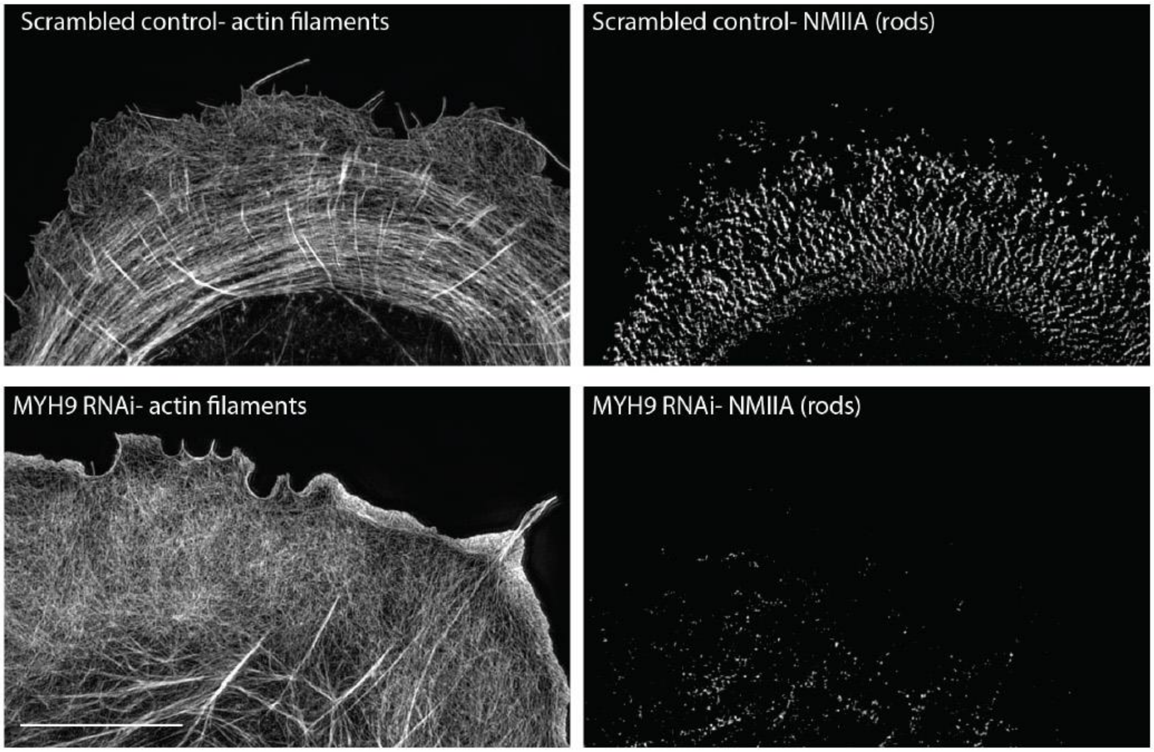

B NMIIB rod domains

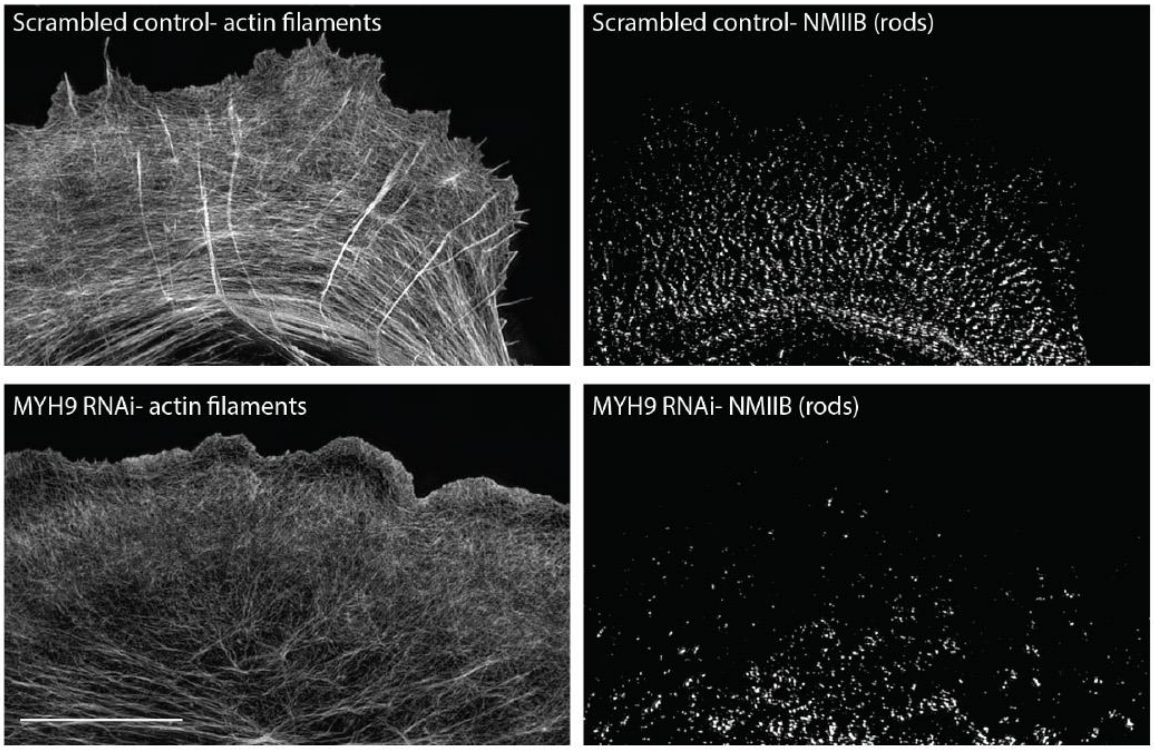

Figure 2-S8: NMIIB-F stacks are absent after knockdown of NMIIA in U2-OS cells A) Actin filaments localized with phalloidin and NMIIA-F rod domains localized with an antibody in a cell treated with an RNA molecule of a random sequence (Scrambled control) or a pool of RNA molecules design to silence the expression of MYH9 (NMIIA). Images were acquired and are displayed using the same parameters. B) Actin filaments localized with phalloidin and NMIIB rod domains localized with an antibody in a cell treated with an RNA molecule of a random sequence (Scrambled control) or a pool of RNA molecules designed to silence the expression of MYH9 (NMIIA). Images were acquired and are displayed using the same parameters. Note the absence of stack-like arrays of NMIIA-F when RNAi reduces the amount of NMIIA. Scale bars, 10 μm.

Chapter III

Muscle stress fibers give rise to sarcomeres in cardiomyocytes

Aidan M. Fenix, Mike R. Visetsouk, Abigail C. Neininger, Nilay Taneja, Ryan J. Garde, Baohong Liu, Benjamin R. Nixon, Annabelle E. Manalo, Jason R. Becker, Scott W. Crawley, David M. Bader, Matthew J. Tyska, Qi Liu, Jennifer H. Gutzman, Dylan T. Burnette

Introduction

The sarcomere is the contractile unit within cardiomyocytes which drives heart muscle contraction, and thus, blood flow throughout the body. At its core, a sarcomere is composed of “thick” myosin II filaments, and “thin” actin filaments (Figure 3-1) (Au, 2004). One sarcomere is measured from Z-line to Z-line, which contain α-actinin 2 (Figure 3-1). The proper establishment of cardiac sarcomeres during development and their subsequent maintenance is critical for heart function. Previous studies in cultured myocytes have shown the presence of actin bundles called “stress fiber-like structures” similar in appearance to classic stress fibers (Dlugosz et al., 1984). These stress fibers were often found to be close to the edge of the myocyte with sarcomeres existing further from the edge (Rhee et al., 1994). These studies proposed that the stress fibers served as a template for the formation of sarcomeres (Dlugosz et al., 1984; Rhee et al., 1994; Sanger et al., 2005). The original model that proposed this was called the Templating Model (Dlugosz et al., 1984), and was proposed before it was known these stress fibers contained both non-muscle and sarcomeric proteins (Rhee et al., 1994). Beyond non-muscle myosin IIB (NMIIB), which is present in non-muscle cells, stress fibers in muscle cells contain muscle specific proteins, such as α-actinin, tropomyosin, troponins, and tropomodulin (Almenar-Queralt et al., 1999; Rhee et al., 1994; Sanger et al., 2005). Each of these proteins have non-muscle paralogs, which likely serve similar functions (Bryce et al., 2003; Colpan et al., 2013; Cote, 1983; Gunning et al., 2015; Lim et al., 1986; Sjoblom et al., 2008). Partly in response to the presence of muscle specific proteins in stress fibers, the Templating Model was modified to the "Pre-Myofibril Model" (Rhee et al., 1994; Sanger et al., 2005). Even though these models have different names and are often presented as mutually exclusive, they are very similar in their predictions. Specifically, both models posit an actin bundle that appears structurally similar to a stress fiber will acquire a row of sarcomeres over time to become a "myofibril" (Dlugosz et al., 1984; Rhee et al., 1994; Sanger et al., 2005) (Figure 3-1). There is a vast amount of localization data in fixed cardiomyocytes to support these models. However, there is very little dynamic data in live cells that suggests stress fibers give rise to sarcomeres. The strongest dynamic support comes from imaging fluorescently tagged α-actinin 2 in myocytes. Time montages from chick skeletal myotubes showed small puncta of α-actinin 2 adding to pre-existing Z lines (McKenna et al., 1986). Subsequently, a time montage was used to show a similar phenomenon occurring in chick cardiomyocytes (Dabiri et al., 1997).

Some *in vivo* data support the Template/Pre-Myofibril Model, while others do not. In strong support of the Template/Pre-Myofibril Model, static images of chick heart tissue have essentially revealed every structure described in primary cultured chick cardiomyocytes (Du et al., 2008). The presence of NMIIB-containing stress fibers in the cardiomyocytes was particularly clear (Du et al., 2008). NMIIB germline knockout (KO) mice were also reported to have fewer and disorganized sarcomeres via EM (Tullio et al., 1997). On the other hand, several studies have called into question the role of stress fibers in sarcomere assembly. First, several studies examining cardiomyocytes within mouse or chick heart tissue did not find stress fibers containing NMIIB (Ehler et al., 1999; Kan et al., 2012; Ma et al., 2009). In addition, a conditional KO mouse that removes NMIIB genetically at P9 apparently still had striated sarcomere structures (Ma et al., 2009). Finally, a conditional heart KO of the other major paralog of NMII, NMIIA, was also reported to have no apparent defects in heart formation (Conti et al., 2004; Conti et al., 2015). Taken together, the lack of clear data showing stress fibers in cardiomyocytes and inconsistencies for a role of NMII in sarcomere assembly calls into question whether the Template/Pre-Myofibril Model is a viable construct for understanding sarcomere assembly (Sanger et al., 2005; Sparrow and Schock, 2009).

There is further data to suggest that a mechanism other than that described in the Template/Pre-Myofibril model could be driving sarcomere assembly. This alternative model—called the “Stitching Model”—is based on the idea that parts of a sarcomere are assembled independently and then brought together (i.e., stitched) (Holtzer et al., 1997; Lu et al., 1992; Sanger et al., 2005). In support of the Stitching Model, studies in *Drosophila* have shown the presence of small myosin filaments following knockdown (KD) of separate Z-line components (Rui et al., 2010). This data suggests that myosin filaments can assemble independently of Z-lines. Indeed, there are also electron micrographs that appear to show stacks of myosin II filaments (i.e., A-bands) without detectable actin filaments in skeletal muscle (Holtzer et al., 1997; Lu et al., 1992; Sanger et al., 2005). Examination of electron micrographs also supports the idea that bodies containing Z-line components and actin filaments—called “I-Z-I” bodies—could also exist in skeletal muscle without apparent myosin II filaments (Holtzer et al., 1997; Lu et al., 1992; Sanger et al., 2005). Based on this data, it was proposed that stitching could occur through sequential assembly by adding new I-Z-I bodies and myosin II filaments (Holtzer et al., 1997; Lu et al., 1992; Sanger et al., 2005).

The Template/Pre-Myofibril Model and Stitching Model have been proposed to be mutually exclusive explanations of how sarcomeres arise. The Template/Pre-Myofibril Model predicts that multiple sarcomeres will appear approximately simultaneously along the length of a stress fiber, while the Stitching Model would predict that sarcomeres will appear adjacently one by one, sequentially (see original models in (Dlugosz et al., 1984; Holtzer et al., 1997; Rhee et al., 1994)). Here, we leverage our discovery that immature human induced pluripotent stem cell-derived cardiomyocytes (hiCMs) completely disassemble and then reassemble their sarcomeres following plating to test these possibilities. Using this assay, we show that sarcomeres are assembled directly from actin stress fiber templates, and we refer to these stress fibers as Muscle Stress Fibers (MSFs). Our data suggests sarcomere assembly is dependent on the formin actin filament nucleator, FHOD3, non-muscle myosin IIA and non-muscle myosin IIB. Surprisingly, our data does not fully support either the Template/Pre-Myofibril Model or Stitching Model, but rather some aspects of each. As such, we now propose a unified model of sarcomere assembly based on the formation of MSFs and their subsequent transition into sarcomere-containing myofibrils.

Results

Development of an assay to test sarcomere assembly

To address how cardiac sarcomeres are assembled, we used hiCMs as a model system (Takahashi et al., 2007). We first noted the actin filaments in hiCMs, which had spread for 24 hours, had two distinct organizations, muscle stress fibers (MSFs) and sarcomere-containing myofibrils (Figure 3-1). Spread hiCMs displayed MSFs at the leading edge and organized sarcomere structures in the cell body (Figure 3-1). Strikingly, super-resolution imaging revealed the MSFs in hiCMs resembled a classic actin stress fiber found in non-muscle cells, referred to as actin arcs (Figure 3-1) (Heath, 1983; Hotulainen and Lappalainen, 2006). Actin arcs are stress fibers on the dorsal (top) surface of the cell that are parallel to the leading edge and stain continuously with fluorescent phalloidin (Figure 3-1). Similarly, both MSFs and sarcomeres in hiCMs are on the dorsal surface (Figure 3-1). We next sought to test the concept that a MSF obtained sarcomeres as predicted by the Templating/Pre-Myofibril Model.

To test whether MSFs give rise to sarcomeres, we needed to develop a sarcomere assembly assay. We noticed that freshly plated hiCMs contained no sarcomere structures (Figure 3-S1). hiCMs subsequently assembled sarcomere structures over the course of 24 hours. Loss of sarcomere structure following plating was confirmed by visualizing multiple sarcomeric proteins, including actin, beta cardiac myosin II (βCMII), α-actinin 2, and TroponinT (Figure 3-S1). We next sought to ask if MSFs template sarcomeres. Indeed, time-lapse microscopy of hiCMs expressing the actin probe Lifeact-mEmerald (Riedl et al., 2008) revealed that MSFs acquire sarcomeres over time, with the first sarcomeres appearing between 4 and 16 hours (Figure 3-1). As our SIM data suggests MSFs and sarcomeres are localized on the dorsal surface of the cell, the transition of MSFs to sarcomeres also occurs on the dorsal surface of the cell (Figure 3-1).

Figure 3-1

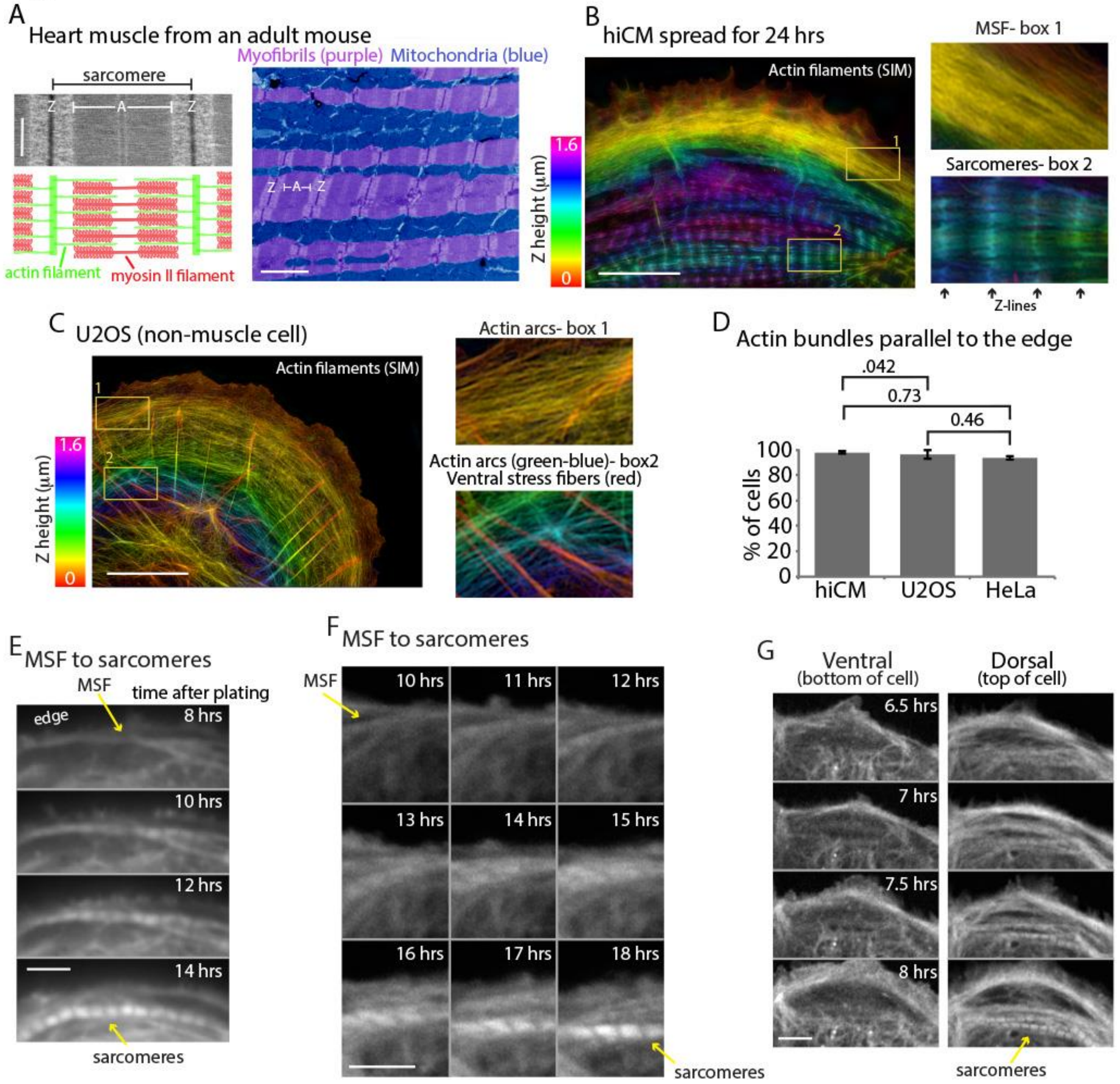

Figure 3-1: Sarcomeres arise directly from Muscle Stress Fiber (MSF) precursors (A) Electron microscopy (EM) schematic of a cardiac sarcomere from adult mouse. Electron dense regions on border of sarcomere are Z-discs (Z), while the core of the sarcomere is composed of thin actin filaments and thick myosin II filaments (A). Multiple sarcomeres aligned adjacently form a myofibril (lower mag EM, right). (B) hiCM allowed to spread for 24 hours following plating and imaged with SIM. hiCM has been stained for actin and color coding is a representation of height (Z plane) within the cell following 3D imaging (Z-height, left). Notice the clear stress fiber and sarcomere-like actin organization at the front and rear of the cell in box 1 and 2, respectively. (C) Spread U2OS cell color

coded for Z as in Figure 3-1, displaying prominent actin arc stress fibers behind leading edge of cell and imaged with SIM. Box 1 shows actin arcs just behind the leading edge of cell, while box 2 shows actin arcs on dorsal surface in cell body (green and blue colored actin), while ventral stress fibers (red colored actin) are on bottom surface of cell. (D) Percentage of hiCMs, U2OS, and HeLa cells with actin arc stress fibers. hiCMs; 1372 cells over 3 experiments. U2OS; 37 cells over 4 experiments. HeLa; 186 cells over 4 experiments. (E) Wide-field time lapse of hiCM transfected with Lifeact-mEmerald to visualize actin. MSF at front of hiCM undergoes retrograde flow and acquires sarcomeres (yellow arrows). (F) Laser-scanning confocal microscopy of hiCM expressing Lifeact-mApple showing MSF to sarcomere transition. hiCM lacks sarcomeres at first time point, and MSF at edge of cell undergoes retrograde flow and acquires sarcomeres (yellow arrows). (G) 3D laser-scanning confocal microscopy of hiCM expressing Lifeact-mApple forming sarcomeres. Note how ventral surface (left montage) contains no sarcomere structures, while sarcomere assembly occurs on the dorsal surface of cell (right montage). Scale Bars; (A) 500 nm high mag, 2 µm low mag; (B), (C), (E), (F), (G), 10 µm. P-values denoted in graphs.

To further characterize our sarcomere assembly assay, we used α-actinin 2, which is a classic marker of Z-lines (Luther, 2009). Endogenous α-actinin 2 localized to both MSFs and sarcomeres (Figure 3-2). Small puncta of α-actinin 2 localized to MSFs, while sarcomeres had linear α-actinin 2 which labeled Z-lines (Figure 3-2). As has been shown in other systems (Dabiri et al., 1997; Du et al., 2008), the spacing between α-actinin 2 puncta increases during the MSF to sarcomere transition, with the spacing of α-actinin 2 ~0.5 µm in MSFs and ~1.7 µm in sarcomeres (Figure 3-2). In hiCMs, α-actinin 2 puncta in MSFs alternates with NMII, as has been shown for other systems (Figure 3-S2) (Ehler et al., 1999; Hotulainen and Lappalainen, 2006; Rhee et al., 1994; Sanger et al., 2005). Interestingly, the spacing of α-actinin 2 puncta associated with MSFs in hiCMs was very similar to the spacing of α-actinin 4 (i.e., a non-muscle paralog of α-actinin) in actin arcs in U2OS cells (Figure 3-2). If MSFs were serving as a template for sarcomeres, we asked whether the molecules in MSFs were also being incorporated into the sarcomere structures. Previous data suggests α-actinin 2 puncta join existing Z-lines (Dabiri et al., 1997; McKenna et al., 1986). To test this hypothesis, we utilized a photo-convertible probe, mEOS2, which converts from green to red fluorescence to specifically mark the α-actinin 2 puncta of MSFs (McKinney et al., 2009). We found that a subset of photo-converted α-actinin 2-mEOS2 puncta were indeed incorporated into Z-lines (Figure 3-2). Collectively, these results strongly suggest MSFs give rise to sarcomeres in hiCMs.

Figure 3-2

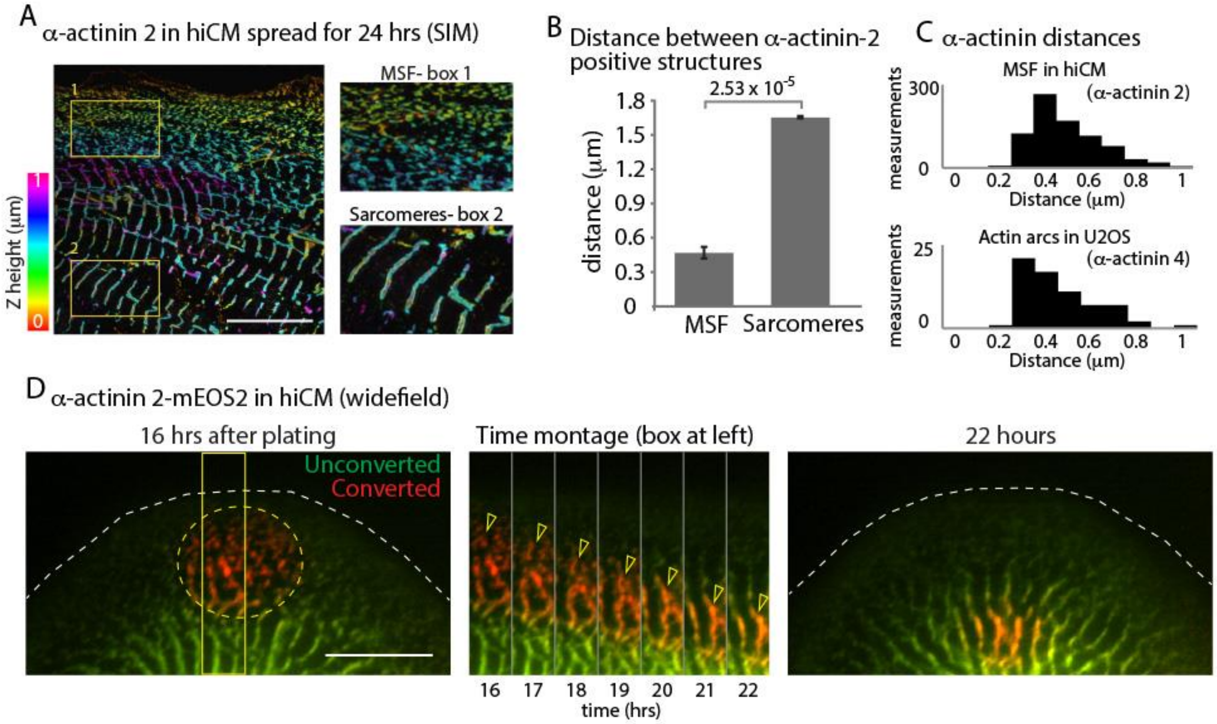

Figure 3-2: α-Actinin 2 spacing and dynamics in hiCMs

(A) Color coded representation for Z-height of endogenous α-actinin 2 in MSFs (box 1) and sarcomeres (box 2) of hiCM imaged with SIM. Note difference in structure and spacing of α-actinin 2 in MSFs (box 1) and sarcomeres (box 2) (B) Distance between α-actinin 2 structures in MSFs and sarcomeres. MSFs; 14 cells, 3 experiments, 827 measurements, Sarcomeres; 15 cells, 3 experiments, 527 measurements. Distance between structures increases as MSFs transition to sarcomeres. (C) Histogram depicting distribution of distances between α-actinin 2 structures in MSFs in hiCMs (top) and α-actinin 4 found in actin arcs of non-muscle cells (bottom). Distribution is similar between cell types. (D) Wide-field montage of photoconversion of α-actinin 2-mEOS2 in hiCM. MSFs at leading edge of the cell were photoconverted (green to red) and imaged over time. Montage (middle) depicts α-actinin 2-mEOS2 puncta of MSFs (hollow yellow arrow heads) transition into sarcomere structures (middle, right). Scale Bars; (A), (D), 10 μM. P-values denoted in graphs.

Actin Retrograde flow in hiCMs and non-muscle cells

We next wanted to further investigate the similarities between MSFs and actin arcs. Actin arc stress fibers in non-muscle cells undergo robust “retrograde flow” away from the edge of the cell as can be seen in U2OS cells, a classic model of mesenchymal migration (Figure 3-2) (Hotulainen and Lappalainen, 2006; Ponti et al., 2004). Kymography measurements found that actin arcs in U2OS cells moved at ~200 nm/min, in agreement with previously published findings (Figure 3-2) (Ponti et al., 2004). We found MSFs also underwent retrograde flow (Figure 3-3). Strikingly, however, kymography revealed MSFs in hiCMs moved significantly slower than actin arcs in U2OS cells (Figure 3-3). This was the first indication that actin arcs in non-muscle cells are different than MSFs in hiCMs. We next wanted to define the mechanisms governing MSFs and their acquisition of sarcomeres. As the mechanisms of actin arc formation and maintenance have been well studied (Burnette et al., 2014a; Hotulainen and Lappalainen, 2006; Murugesan et al., 2016), we were interested in using our assay to test whether the same mechanisms driving actin arc dynamics were governing MSF dynamics.

Figure 3-3

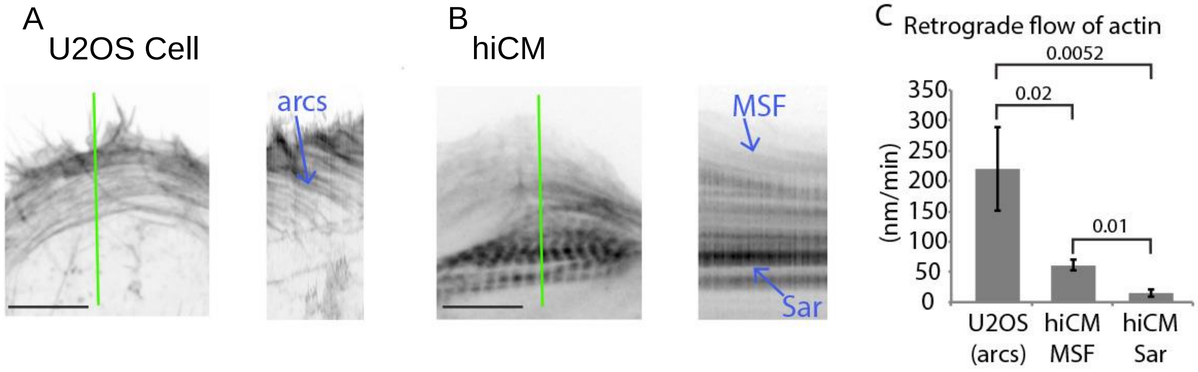

Figure 3-3: Retrograde flow of actin in non-muscle cells and hiCMs
(A) Still of U2OS cell expressing Lifeact-mEmerald (left) imaged with spinning disk confocal. Kymograph (right) taken from purple line of left image. Note robust movement of actin arc stress fibers (yellow arrow). (B) Still of hiCM expressing Lifeact-mApple (left) imaged with spinning disk confocal. Kymograph (right) taken from purple line of left image. Note slower movement of MSF in hiCM compared to actin arcs in U2OS cell, and stationary nature of sarcomeres. (C) Quantification of actin stress fiber translocation rates in U2OS cells and hiCMs. U2OS; 3 cells over 3 experiments. hiCMs; 12 cells over 3 experiments. Scale Bars; (A), (B), 10 µM. P-values denoted in graph.

Formins, but not the Arp2/3 complex, are required for MSF-based sarcomere formation

The Arp2/3 complex is well known to be required for actin arc formation in non-muscle cells (Hotulainen and Lappalainen, 2006). To test the role of the Arp2/3 complex during sarcomere assembly, we allowed hiCMs to spread in the presence of CK666, an inhibitor of the Arp2/3 complex (Nolen et al., 2009). Surprisingly, hiCMs allowed to spread in the presence of CK666 formed robust MSFs and sarcomeres comparable to untreated control cells (Figure 3-4). Cells were quantified as containing sarcomeres if they contained three parallel Z lines in a row each separated from the adjacent Z line by 1µm – 2.5µm. An α-actinin 2 localization was defined as a Z line if it was as least 2x the length of the microscope's resolution limit (see Methods). In addition, the spacing between Z-lines between control and CK666 hiCMs was unchanged (Figure 3-4). We also found the retrograde flow of MSFs was unchanged between control and CK666-treated hiCMs (Figure 3-4). To confirm inhibition of the Arp2/3 complex by CK666, we examined the endogenous localization of the Arp2/3 complex with and without CK666 treatment. The strong localization of the Arp2/3 complex at the edge of control hiCMs was absent in CK666 treated hiCMs (Figure 3-4). To further confirm this observation, we analyzed the loss of p16b-mEGFP, a subunit of the Arp2/3 complex, from the leading edge of hiCMs via CK666 in live hiCMs. Indeed, hiCMs showed rapid loss of p16b-mEGFP from the leading edge following administration of CK666 (Figures 3-4). The delocalization of the Arp2/3 complex from the leading edge is consistent with inactivation by CK666, as shown previously in non-muscle cells (Henson et al., 2015). Taken together, our data suggests that the Arp2/3 complex does not need to be localized at the leading edge for sarcomeres to be assembled. While we find it un-likely, it is possible a relatively small amount of Arp2/3, could be driving the retrograde flow in the CK666 treatment. However, the inhibitor is used at above saturation concentrations, so it is likely other mechanisms are driving retrograde flow in hiCMs.

Figure 3-4

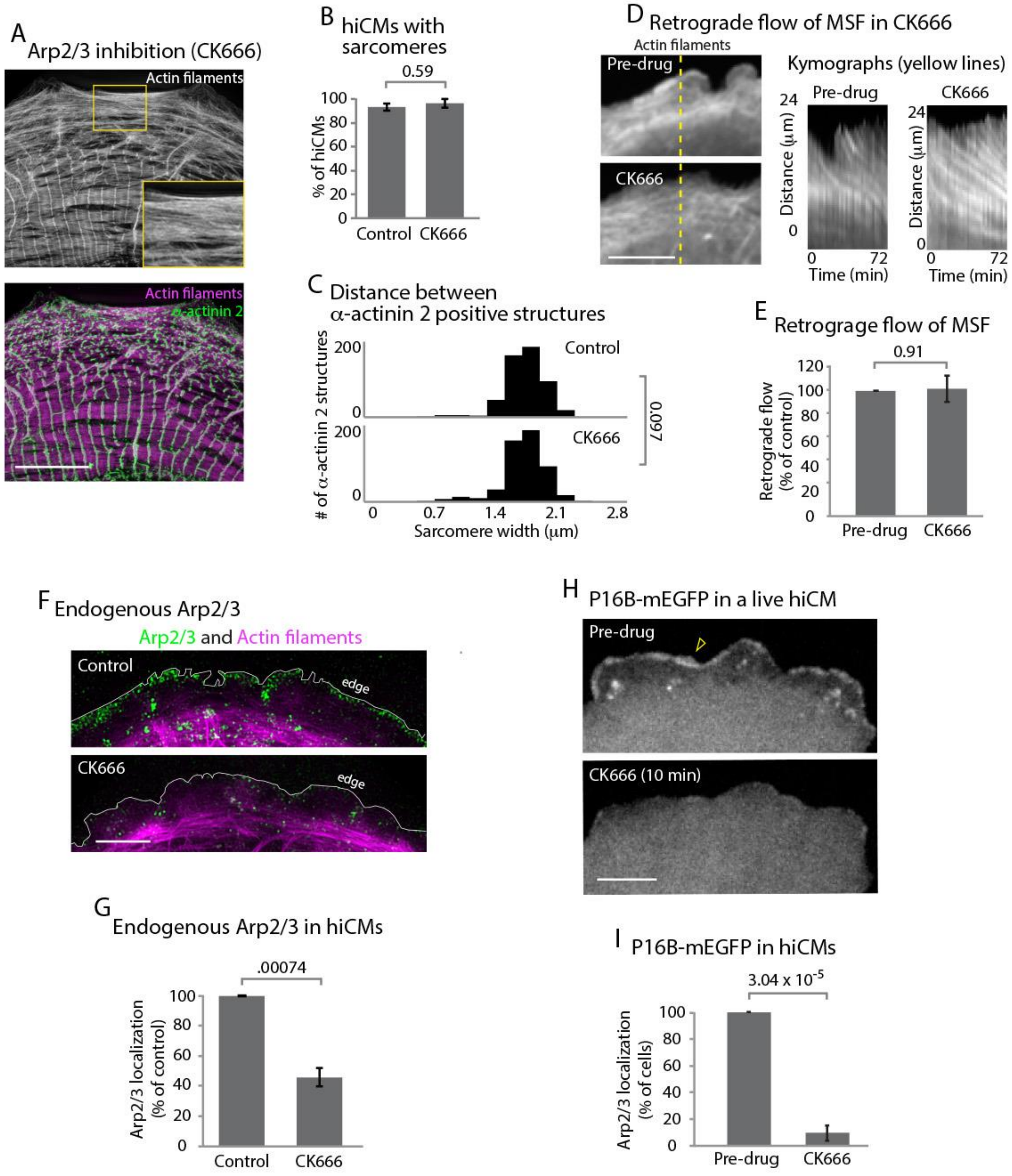

Figure 3-4: The Arp2/3 complex is not required for sarcomere assembly
(A) hiCM allowed to spread for 24 hours in the presence of 25 µM CK666, labeled with actin and α-actinin 2 (i.e., Z-lines) and imaged with SIM. Box indicates presence of MSFs. (B) Quantification of percentage of cells with sarcomeres at 24 hours post plating in

control and 25 µM CK666. Control: 76 cells, 10 experiments; 25 µM CK666: 41 cells, 3 experiments. (C) Histogram of distribution of distances between α-actinin 2 Z-lines. Note tight distribution of Z-lines in both conditions. Control: 14 cells, 3 experiments, 317 measurements. 25 µM CK666: 16 cells ,3 experiments, 530 measurements. (D) Stills of hiCM expressing Lifeact-mApple pre (top) and post (bottom) addition of 25 µM CK666 and imaged with spinning disk confocal. Kymographs (right) taken from dotted yellow line (left). (E) Rates of retrograde flow of hiCMs depicted as percent change in CK666 from pre-drug condition. 8 cells over 3 experiments. (F) Localization of the Arp2/3 complex in control (top) and 25 µM CK666 treated (bottom) hiCMs imaged with SIM. Note loss of Arp2/3 at the edge of CK666 treated hiCM. Cells spread for 24 hrs in presence of 25 µM CK666 as in Figure 3-4A (G) Quantification of loss of the Arp2/3 complex from the leading edge of hiCMs. Control; 36 cells over 3 experiments. 25 uM CK666; 29 cells over 3 experiments. (H) hiCM expressing P16B-mEGFP (a component of the Arp2/3 complex) and imaged with spinning disk confocal. Localization of P16B-mEGFP at leading edge in pre-drug control (top) is acutely lost after addition of 25 µM CK666 (bottom). (I) Quantification of hiCMs displaying localization of the Arp2/3 complex (P16B-mEGFP) pre- and post-25µM CK666 in live hiCMs (as in Figure 3-4H). 27 cells over 3 experiments. Scale bars; (A), (D), (F), (H), 10 µm. P-values denoted in graphs.

In addition to the Arp2/3 complex, formin-mediated actin polymerization has been shown to be crucial for actin arc formation and dynamics in multiple cell types (Hotulainen and Lappalainen, 2006; Murugesan et al., 2016). As a starting point to test whether formins are required for sarcomere assembly, we allowed hiCMs to spread in the presence of a pan-inhibitor of formin-mediated actin polymerization, small molecule inhibitor of formin homology domain 2, SMIFH2 (Rizvi et al., 2009). SMIFH2 has been shown to stop formin-mediated actin polymerization, actin arc formation and retrograde flow in non-muscle cells (Henson et al., 2015; Murugesan et al., 2016; Rizvi et al., 2009). We found hiCMs spreading in the presence of SMIFH2 completely failed to form sarcomeres (Figures 3-5, and 3-S3). This effect was reversible, as sarcomeres formed after the removal of SMIFH2 (Figure 3-S4). Distances between α-actinin 2 structures were also significantly decreased in hiCMs treated with SMIFH2, with the distribution of α-actinin 2 more closely resembling MSFs than sarcomeres (Figures 3-5 and 3-2). However, the alignments of the α-actinin 2 puncta were not similar to MSFs in control hiCMs, as they were not periodic (Figure 3-5 and 3-2). This result strongly suggested formins are required for sarcomere assembly.

We next asked if formin inhibition was affecting either the MSFs or sarcomeres directly. To test this, we allowed hiCMs to spread for 24 hours (after they have established sarcomeres) and imaged their actin cytoskeleton via live-cell microscopy before and after administering SMIFH2 (Figure 3-5). Following addition of SMIFH2, formation of new MSFs was immediately blocked, along with retrograde flow of existing MSFs (Figures 3-5). However, we did not detect any changes in sarcomere structure over the short time of the experiment, and hiCMs continued to beat in the presence of SMIFH2 (note sarcomere structure in Figure 3-5). As there are 15 mammalian formin genes, we next asked what specific formin was required for sarcomere assembly.

Figure 3-5

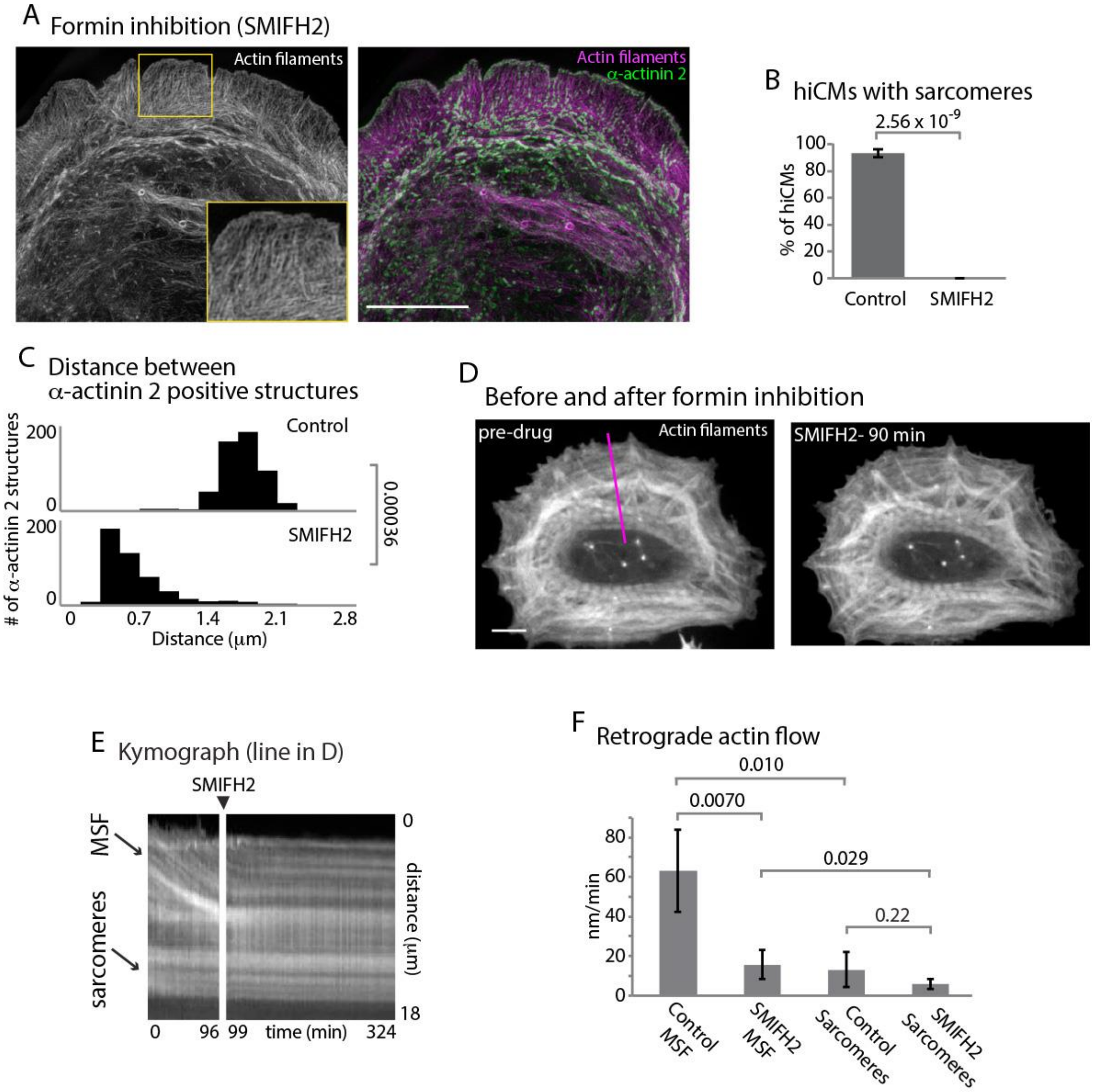

Figure 3-5: Formins are required for sarcomere assembly and MSF dynamics
(A) hiCM allowed to spread in the presence of 25 µM SMIFH2 for 24 hours, labeled with actin and α-actinin 2 and imaged with SIM. Box indicates loss of transverse MSFs behind leading edge of hiCM. (B) Quantification of percentage of cells with sarcomeres at 24 hours post plating. Control: 76 cells, 10 experiments; 25 µM SMIFH2, 16 cells, 3 experiments (C) Histogram of distribution of distances between α-actinin 2 Z-lines. Control: 14 cells, 3 experiments, 317 measurements, 25 µM SMIFH2: 11 cells, 3 experiments, 468 measurements. (D) Stills from live hiCM expressing Lifeact-mApple before (left) and 90 minutes following addition of 25 µM SMIFH2 (right) and imaged with spinning disk microscopy. Note how sarcomeres and overall actin architecture remains unperturbed at 90 minutes post 25 µM SMIFH2. (E) Kymographs of MSF and sarcomere

retrograde flow taken from purple line in Fig. 4D. Note immediate loss of retrograde flow following addition of 25 µM SMIFH2. (F) Quantification of actin retrograde flow in hiCMs pre and post addition of 25 µM SMIFH2. Control: 12 cells, 3 measurements from each cell, 3 experiments; 25 µM SMIFH2, 12 cells, 3 measurements from each cell, 3 experiments. Scale Bars: (A), (D) 10 µM. P-values denoted in graphs.

We performed RNA sequencing analysis of mRNA isolated from hiCMs. Normalized read counts revealed that one formin, FHOD3, was expressed higher than all other formins (Figure 3-6). Indeed, previous data from isolated rat cardiomyocytes has shown FHOD3 as crucial for sarcomere maintenance (Iskratsch et al., 2010; Kan et al., 2012; Taniguchi et al., 2009). Rat cardiomyocytes containing myofibrils subsequently lost their myofibrils following FHOD3 knockdown (Iskratsch et al., 2010; Taniguchi et al., 2009). However, the role of FHOD3 during *de novo* sarcomere assembly has not been tested. Therefore, we sought to use our assay to directly test if the formin FHOD3 was required for MSF based sarcomere assembly. We knocked down FHOD3 using siRNA, and hiCMs were unable to assemble sarcomeres following plating (Figure 3-6). Interestingly, KD of the two most highly expressed formins after FHOD3, DAAM1 and DIAPH1, did not stop sarcomere assembly (Figures 3-6 and 3-S5). However, there are clear defects in the actin organization at the cell edge and in the sarcomeres (Figure 3-S5). As FHOD3 had the most prominent phenotype, we decided to focus our further analysis on this condition. In line with pan-formin inhibition, the actin organization and spacing between α-actinin 2 in FHOD3 KD hiCMs closely resembled hiCMs spread in the presence of SMIFH2 (Figures 3-5 and Figure 3-6).

Based on our results, if FHOD3 is involved in sarcomere assembly, it should localize to MSFs. FHOD3-mEGFP localized to both MSFs at the edge of hiCMs, and then becomes increasingly organized away from the leading edge of the cell where sarcomeres are located (Figure 3-6). This localization is consistent with a role for FHOD3 in mediating the transition from MSFs to sarcomeres. Taken together, our data show that the formin FHOD3 localizes to both MSFs and sarcomeres, and is required for *de novo* sarcomere assembly. We next wanted to investigate other potential mechanisms regulating sarcomere assembly.

Figure 3-6

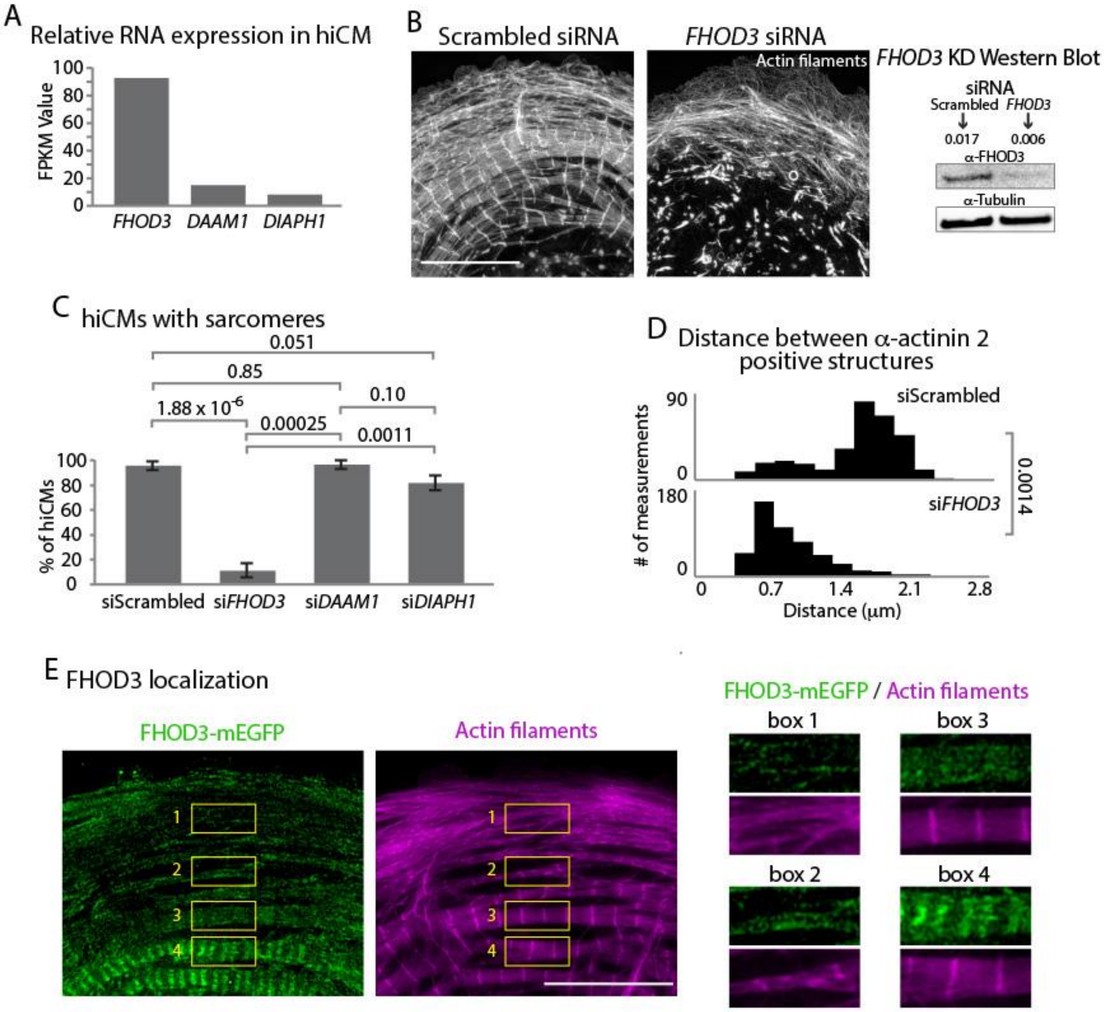

Figure 3-6: Formin FHOD3 is required for sarcomere assembly
(A) Normalized Fragments Per Kilobase Million (FPKM) of mRNA expression of the top 3 expressed formins in hiCMs. 3 experiments, 3 separate runs. (B) Actin of siRNA scramble control and siRNA *FHOD3* hiCMs allowed to spread for 24 hours and imaged with SIM. Note loss of sarcomeres comparable to SMIFH2 treatment in FHOD3 KD hiCMs (Figure 3-5A). Western blot (right) denotes protein loss in FHOD3 KD. (C) Quantification of percentage of cells with sarcomeres at 24 hours post plating in scramble control, si*FHOD3*, si*DAAM1*, and si*DIAHP1* hiCMs. Control: 76 cells, 10 experiments; siRNA FHOD3: 33 cells, 3 experiments; siRNA DAAM1: 29 cells, 3 experiments; siRNA Dia1: 26 cells, 3 experiments. (D) Histogram of distribution of distances between α-actinin 2 Z-lines. Control: 14 cells, 3 experiments, 317 measurements; si*FHOD3*: 15 cells, 3 experiments, 488 measurements. (E) hiCM transfected with FHOD3-mEGFP, fixed at 24 hours, stained for Actin and imaged with SIM. Boxes 1-4 depict localization of FHOD3-

mEGFP along MSFs (boxes 1 and 2) and in sarcomeres (boxes 3 and 4). Note increasingly organized structure, and localization between Z-lines of FHOD3-mEGFP. Scale bars; (B), (E) 10 µm. P-values denoted in graphs.

Non-muscle myosin II is required for cardiac sarcomere actin filaments

In addition to actin nucleators, non-muscle myosin II (NMII) activity has been shown to be required for actin arc formation and organization in non-muscle cell types (Hotulainen and Lappalainen, 2006; Medeiros et al., 2006). Thus, we asked whether NMII was required for MSF formation and/or the MSF to sarcomere transition. We first localized the two major paralogs of NMII in humans, NMIIA and NMIIB, in spread hiCMs (Vicente-Manzanares et al., 2009b). Both NMIIA and NMIIB localize to actin arcs in non-muscle cells (Kolega, 1998). Consistent with this, both NMIIA and NMIIB localized to MSFs, and were restricted from the middle of the cell where sarcomeres were localized (Figure 3-7). Indeed, time-lapse microscopy revealed NMIIA filaments formed at the edge of hiCMs and underwent retrograde flow as in non-muscle cells (Figure 3-7). However, NMIIA remained at the edge of hiCMs and was restricted from the cell body where sarcomeres are formed (Figure 3-7). The vast majority of NMIIA and NMIIB filaments overlapped, except at the very leading edge where NMIIA is localized slightly ahead of NMIIB in hiCMs (Figure 3-7). Super-resolution microscopy revealed that most NMII filaments contained NMIIA and NMIIB (Figure 3-7). NMIIA and NMIIB co-filaments have previously been reported in non-muscle cells (Beach et al., 2014; Shutova et al., 2014). Muscle thick filaments have also been shown to contain multiple myosin isoforms in nematodes (Miller, DM., 1983). Measurements of the lengths of NMII co-filaments in hiCMs showed lengths agreeing with previously published measurements in non-muscle cells (Figure 3-7) (Beach et al., 2014; Shutova et al., 2014). Taken together, these data suggest NMII organization and dynamics appear similar in MSFs of hiCMs as in actin arcs of non-muscle cells.

Figure 3-7

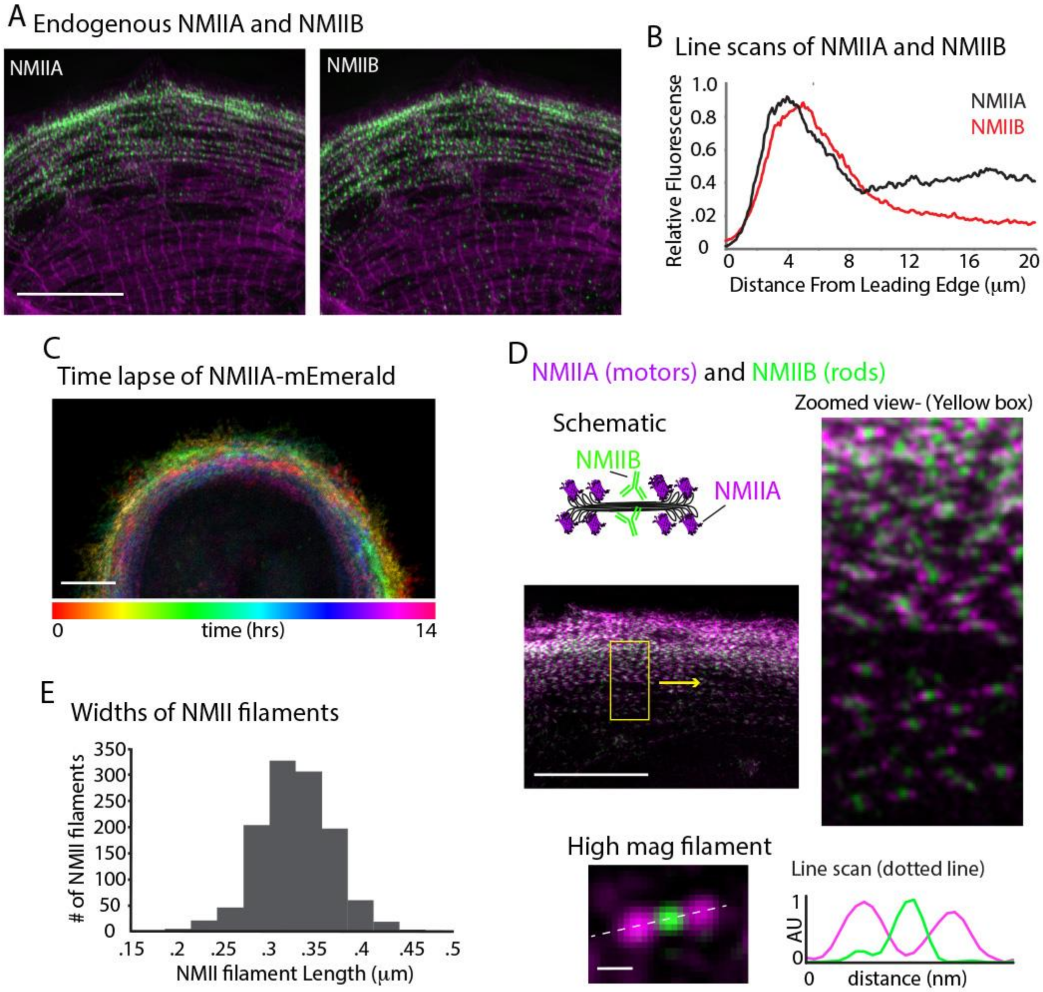

Figure 3-7: NMII Localization and Dynamics in hiCMs

(A) hiCM localized for both endogenous NMIIA (left) and NMIIB (right) and imaged with SIM. Both NMIIA and NMIIB localize to MSFs at the leading edge of hiCMs. (B) Line scans starting from edge of hiCMs showing localization of NMIIA (black) and NMIIB (red). Note NMIIA is localized slightly, ~1 μm in front of NMIIB. NMIIA: 15 cells, 2 experiments; NMIIB: 32 cells, 4 experiments. (C) Color projection of time-lapse of hiCM expressing NMIIA-mEmerald and imaged with laser-scanning confocal. Note how NMIIA-mEmerald remains at the edge of hiCMs. (D) hiCM transfected with NMIIA-mEmerald (N-terminal motors), stained for endogenous NMIIB C-terminal rod domain (cartoon schematic and middle left), and imaged with SIM. High-mag views of NMIIA-NMIIB co-filaments (right) from yellow box 4D (middle left). High mag view of single NMIIA-NMIIB co-filament (bottom) and line scan across white dotted line, from N-terminal motors (purple) and C-terminal rod domains (green). (E) Quantification of NMII co-filament length. Histogram displays the distribution of NMII co-filament lengths (motor-domain to motor-domain). Scale Bars; (A), (C), (D, top), 10 μm, (D, bottom), 200 nm.

Given the presence of both NMIIA and NMIIB in each filament within MSFs, we next asked whether NMIIA and/or NMIIB were required for sarcomere assembly. NMIIA has previously been shown to be required for actin arc assembly in non-muscle cells (Figure 3-S6) (Burnette et al., 2014a; Fenix et al., 2016). Thus, we hypothesized that NMIIA would likely be the key paralog required for MSF formation and subsequent sarcomere assembly. Surprisingly, KD of NMIIA did not result in a complete inhibition of MSF or sarcomere assembly, although the sarcomeres in NMIIA KD hiCMs were disorganized (Figures 3-8 and Figures 3-S7 and 3-S8). Notably, NMIIA KD hiCMs displayed a similar distribution of distances between α-actinin 2 structures compared to control hiCMs (Figure 3-8). This measurement shows that though there are fewer and more disorganized sarcomeres in the NMIIA KD, their widths as measured from Z-line to Z-line are similar to control hiCMs. However, NMIIA KD cells had significantly shorter Z-lines compared to control hiCMs (Figure 3-8). Taken together, this data suggests NMIIA is involved in sarcomere assembly and organization.

It has previously been shown NMIIB is not required for actin arc formation in non-muscle cells (Kuragano et al., 2018; Shutova et al., 2017) (Figure 3-S6). We hypothesized that NMIIB would not be required for MSFs or sarcomere assembly in hiCMs. Surprisingly, NMIIB KD resulted in a complete inability of hiCMs to form sarcomeres after plating (Figures 3-8 and Figures 3-S7 and 3-S9). In addition, the width between α-actinin 2 structures was significantly smaller than control hiCMs (Figure 3-8). These results argue NMIIB is also a major player required for sarcomere assembly in hiCMs. To further confirm that myosin II is required for sarcomere assembly, we then pharmacologically inhibited all myosin II paralogs in hiCMs with blebbistatin (Straight et al., 2003). hiCMs spreading in the presence of blebbistatin were unable to assemble sarcomere structures (Figure 3-S10). While these defects in sarcomere assembly were dramatic, we noticed that hiCMs treated with siRNA against NMIIA or NMIIB were still beating before re-plating. This implied that the pre-existing sarcomeres of the hiCMs were still intact after KD but before plating. Therefore, we immuno-localized α-actinin 2 to visualize sarcomeres in hiCMs before plating. Surprisingly, we found there were no differences between control, NMIIA, and NMIIB KD cells before plating (Figures 3-8 and 3-S11) Collectively, this data would suggest NMIIA and NMIIB are required for *de novo* sarcomere formation, but not homeostasis (i.e., turnover) of pre-existing sarcomeres.

Figure 3-8

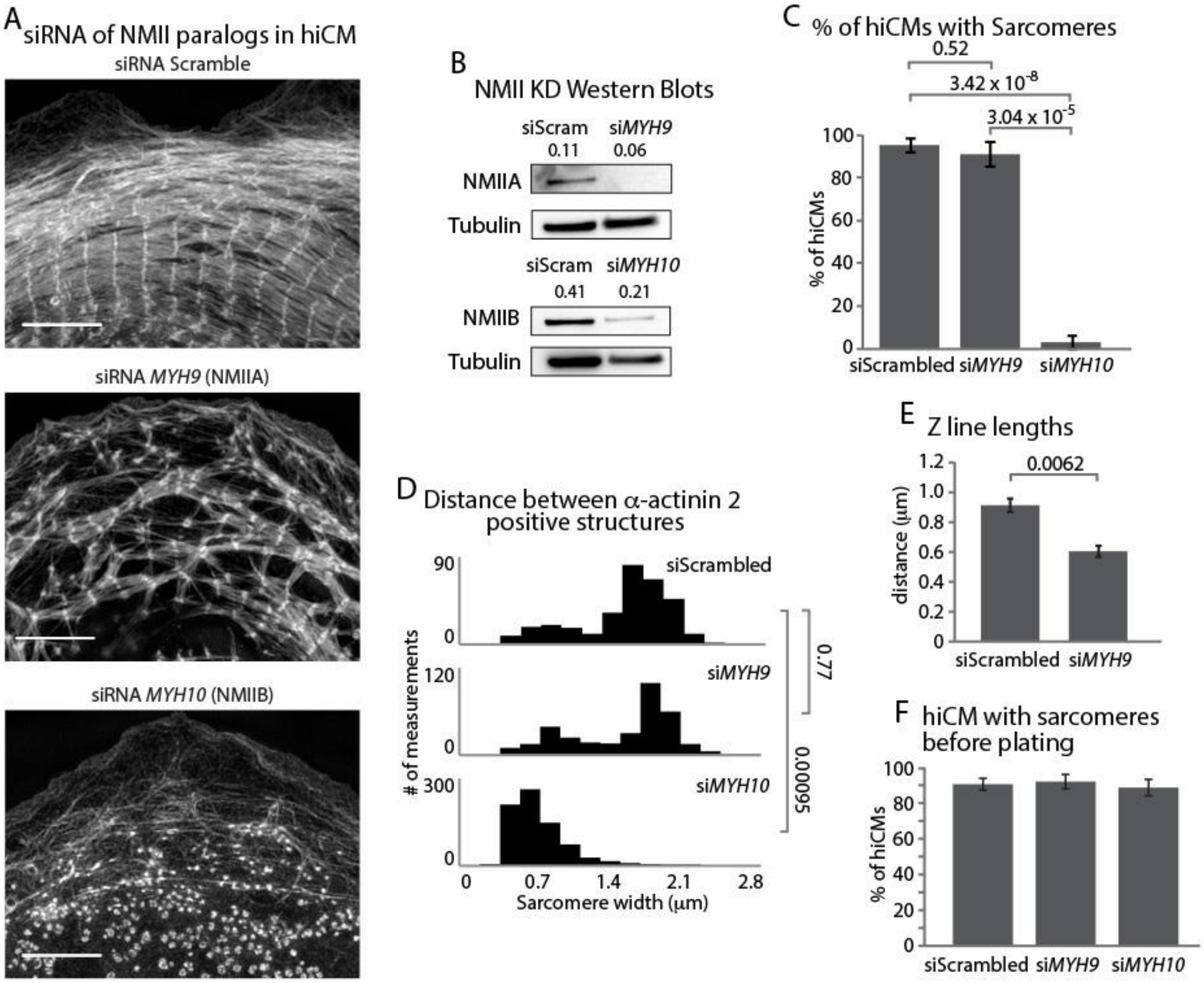

Figure 3-8: NMIIA and NMIIB are Required for Sarcomere Assembly in hiCMs
(A) Actin of representative scramble control (top), NMIIA KD (siRNA *MYH9,* middle), and NMIIB KD (siRNA *MYH10,* bottom) hiCMs allowed to spread for 24 hours and imaged with SIM. NMIIA KD hiCMs (middle) display disorganized sarcomeres, while NMIIB KD hiCMs (bottom) display no actin-based sarcomeres. (B) Representative western blots of 2 separate experiments showing knockdown of NMIIA (siRNA *MYH9*, top) and NMIIB (siRNA *MYH10*, bottom). (C) Percentage of scramble control, NMIIA KD (siRNA *MYH9*), and NMIIB KD (siRNA *MYH10*) hiCMs with actin based sarcomeres at 24 hours spread. Control: 49 cells, 6 experiments; NMIIA KD: 34 cells, 3 experiments; NMIIB KD: 59 cells, 4 experiments. (D) Histogram of distribution of α-actinin 2 structures in scramble control, NMIIA KD (si*MYH9*) and NMIIB KD (si*MYH10*) hiCMs. siScrambled: 554 measurements, 14 cells, 3 experiments; si*MYH9*: 332 measurements, 15 cells, 3 experiments; si*MYH10*: 772 measurements, 15 cells, 3 experiments. (E) Quantification of Z-line lengths in scramble control and NMIIA KD (si*MYH9*) hiCMs. Control: 22 cells, 4 experiments; NMIIA: 14 cells, 3 experiments. (F) Quantification of hiCMs with sarcomeres in scramble control, NMIIA KD (si*MYH9*), and NMIIB KD (si*MYH10*) hiCMs before re-plating. siScrambled:

772 cells, 4 experiments; si*MYH9*: 642 cells, 2 experiments; si*MYH10*: 385 cells, 2 experiments. Scale bar; (A) 10 µm. P-values denoted in graphs.

We next sought to test whether NMIIA and NMIIB are required for sarcomere assembly *in vivo*. We utilized an *in vivo* model in which rapid KD of NMIIA and NMIIB could be achieved before sarcomere assembly has begun. In zebrafish, rapid KD of NMIIA and NMIIB can be achieved via morpholino (MO) injection before heart formation with little genetic compensation as seen in KD animals (Gutzman et al., 2015; Rossi et al., 2015). Therefore, single cell zebrafish embryos were injected with standard control MO, *myh9b* MO directed against NMIIA, or *myh10* MO directed against NMIIB, each in conjunction with a p53 MO as previously described (Gutzman et al., 2015). Embryos were fixed 48 hours post-fertilization, a developmental time point when the heart has formed and is beating. Animals in all MO injection conditions formed 2-chambered hearts (Figure 3-9). *Myh9b* MO and *myh10* MO injections resulted in a significant decrease in NMIIA and NMIIB protein levels, respectively (Figures 3-9 and 3-S12). Both NMIIA KD and NMIIB KD animals had a significant decrease in the number of sarcomeres formed compared to control animals (Figure 3-9). In addition, sarcomeres that did form were significantly smaller in both NMIIA and NMIIB KD animals compared to control animals as assessed by Z-line lengths (Figure 3-9), and similarly, the few myofibrils that did form contained fewer sarcomeres compared to control animals (Figure 3-9). Taken together, our data show that NMIIA and NMIIB are required for sarcomere assembly in zebrafish, which is largely consistent with our *in vitro* data with hiCMs.

Figure 3-9

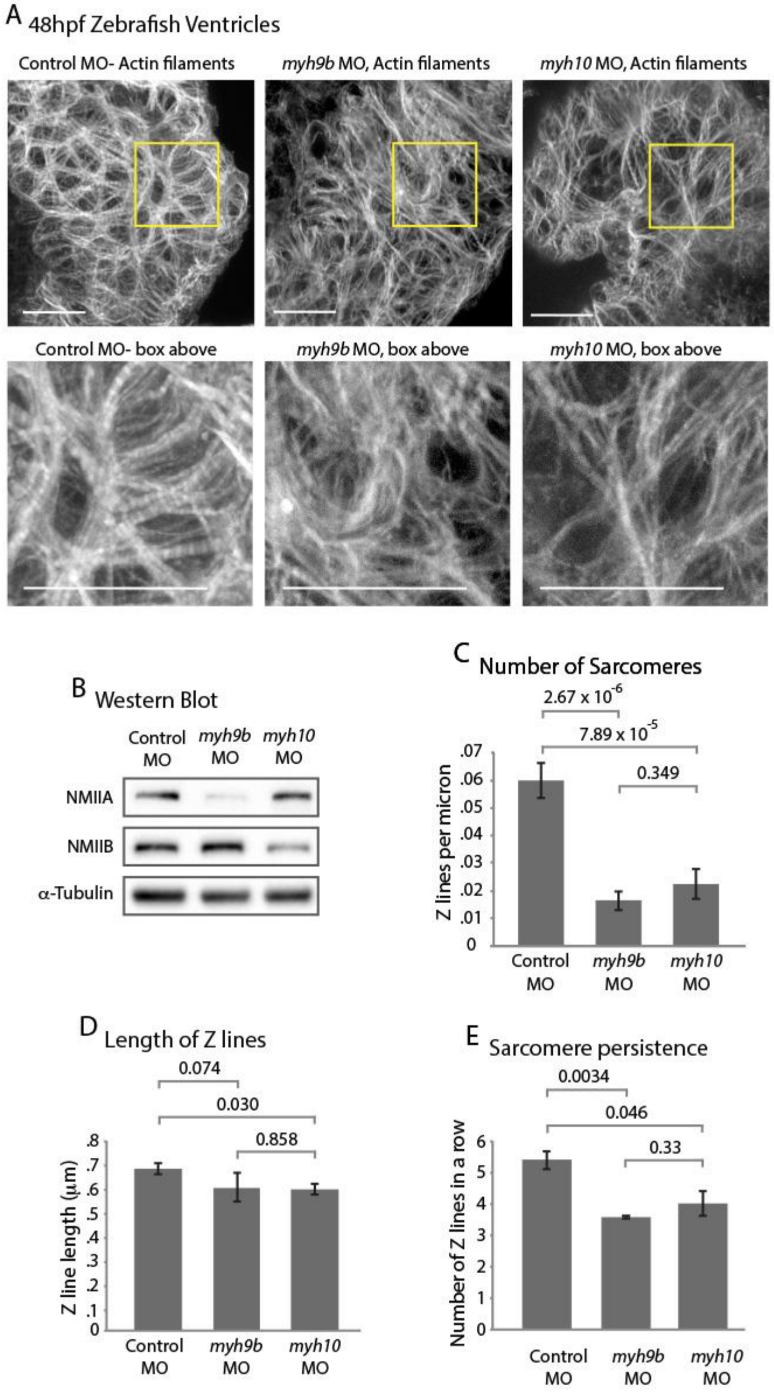

Figure 3-9: NMIIA and NMIIB are required for Sarcomere Assembly in Zebrafish
(A) Actin of Ventricles of control MO, NMIIA KD (*myh9b* MO), and NMIIB KD (*myh10* MO) injected zebrafish embryos fixed at 48 hours post fertilization (hpf) (top) and imaged with laser-scanning confocal. Enlarged boxes from yellow boxes show myofibrils with sarcomeric pattern in control, which is lacking in NMIIA KD and NMIIB KD zebrafish. (B) Representative western blots showing KD of NMIIA (top), NMIIB (middle), and loading

control (bottom). (C) Quantification of number of sarcomeres in control MO, NMIIA KD (*myh9b* MO), and NMIIB KD (*myh10* MO) treated zebrafish embryos at 48 hpf. (D) Quantification of the length of Z-lines in control MO, NMIIA KD (*myh9b* MO), and NMIIB KD (*myh10* MO). (E) Quantification of the average of the number of sarcomeres in a given myofibril in control MO, NMIIA KD (*myh9* MO), and NMIIB KD (*myh10* MO). For (C), (D), and (E); Control MO: 15 animals, 3 experiments; *myh9b* MO: 16 animals, 3 experiments; *myh10* MO: 17 animals, 3 experiments. Scale Bars, (A), 10 µm. P-values denoted in graphs.

Discussion

The goal of this study was to address a decades-old question concerning the origin of sarcomeres assembling in cardiomyocytes. A number of labs have proposed sarcomeres arise from a stress fiber-like precursor, while others propose models where separate sarcomere components sequentially stitch together to form sarcomeres (Holtzer et al., 1997; Lin et al., 1994; Lu et al., 1992; Rhee et al., 1994; Rui et al., 2010; Sanger et al., 2005). Based on previous actin filament staining and NMII localization to these stress fibers, our initial hypothesis was that the mechanisms underlying actin filament polymerization and organization would be related to those governing the non-muscle stress fibers known as actin arcs (see model in Figure 3-S13). In support of this hypothesis, both previous reports in non-human cardiomyocytes and our own work with hiCMs show that the actin organization of these precursors appears identical to actin arcs (Heath, 1983; Rhee et al., 1994; Sanger et al., 2005; Tojkander et al., 2012). Indeed, both MSFs and actin arcs contain NMII, stain continuously with phalloidin, are on the dorsal surface of the cell, and display retrograde flow by which they move away from the cell’s edge (Figure 3-S13). However, our study also revealed distinct differences between the regulation and dynamics of MSFs and actin arcs.

It has been well established that the actin filaments of actin arcs require both nucleation mediated by the Arp2/3 complex and formins (Henson et al., 2015; Hotulainen and Lappalainen, 2006; Murugesan et al., 2016). Our data would suggest the Arp2/3 is not formally required for MSF or sarcomere assembly. However, the Arp2/3 is at the edge of hiCMs, and future work will be needed to elucidate its role in cardiac biology. In contrast to the Arp2/3 complex, our data suggests that formins are required for MSFs and sarcomere assembly. Specifically, we found the formin FHOD3 has a major role in MSF and sarcomere assembly (Figure 3-S13). This adds to the already established role of FHOD3 in sarcomere homeostasis (i.e., turn-over) (Iskratsch et al., 2010; Kan et al., 2012; Taniguchi et al., 2009). While FHOD3 KD displayed the most severe phenotype, KD of DAAM1 and DIAPH1 in hiCMs resulted in both sarcomeric and non-sarcomeric defects in actin architecture. This agrees with previous literature showing roles for multiple formins in explanted mouse cardiomyocytes in maintenance of sarcomere structure (Rosado et al., 2014). The diverse roles of formins during sarcomere assembly and subsequent maintenance should be explored in future work. In addition, we show that NMIIA and NMIIB are required for proper sarcomere assembly both in our hiCM model and during heart development in zebrafish.

Collectively, our data provide new mechanistic and dynamic insight surrounding sarcomere assembly, and highlights key differences between classic, well-studied non-muscle stress fibers, and MSFs in cardiac myocytes (Figure 3-S13). In addition, our model unifies certain aspects of previously proposed models of sarcomere assembly (Figure 3-S13). These previously proposed models, while presented as mutually exclusive from one another, are actually quite similar in certain respects. Highlighting this, our data supports a major feature shared between the Template Model and Pre-Myofibril Model. Specifically, that stress fibers are precursors to sarcomere containing myofibrils rise to sarcomeres. These stress fibers were originally called “stress fiber-like structures” when the Template Model was proposed (Dlugosz et al., 1984; Sanger et al., 2005). Later, they were renamed to Pre-Myofibrils in lieu of more thorough characterization (Rhee et al., 1994; Sanger et al., 2005). It was shown these stress fibers did not contain the same proteins as non-muscle stress fibers (Rhee et al., 1994). However, most of the known proteins in stress fibers found in cardiomyocytes have paralogs in non-muscle stress fibers. We find non-muscle-*like* stress fiber is an apt description. Therefore, we find calling these structures stress fibers as acceptable. In this study, we are comparing regulatory mechanisms of the non-muscle stress fiber referred to as actin arcs, to sarcomere precursors in cardiac myocytes. Thus, we decided to call them Muscle Stress Fibers (MSFs) to avoid confusion.

Our data supports the concept that MSFs transition into sarcomere-containing myofibrils over time. This is the way the cartoon models of both the Template and Pre-Myofibril Models are presented (see original models (Dlugosz et al., 1984; Rhee et al., 1994)). An open question remains as to whether there is true templating during this process. The original Template Model posited that “stress fiber-like structures” [MSFs] would disappear after they were used as a template to build a myofibril (Dlugosz et al., 1984). While some components of MSFs (e.g., α-actinin 2) do appear to persist during the MSF to sarcomere transition, others clearly do not (e.g.,NMIIA/B). In addition to the Templating/Pre-myofibril Models, our data also supports aspects of the Stitching Model. The Stitching Model originally proposed that pre-assembled components of the sarcomere (i.e., A-bands and I-Z-I bodies) would stitch together sequentially to form a myofibril (Holtzer et al., 1997). We did not detect pre-formed I-Z-I bodies or A-bands in our assay (Figure 3-S1) or sequential assembly of sarcomeres to form a myofibril (Figure 3-1).

Our data shows the transition of a MSF to a sarcomere-containing myofibril occurs on the dorsal (top) surface of the cell. However, a recent study also imaging iPSC derived cardiac myocytes claims that sarcomeres are formed on the ventral (bottom) surface of the cell near extracellular matrix adhesions (Chopra et al., 2018). This group also report that the first sarcomeres forms between 24-48 hours after plating, well after we detect the first sarcomere appearing (Chopra et al., 2018). This led us to question what could be leading to these two seemingly opposite results. Importantly, it appears that this group was imaged the ventral (bottom) surface of their myocytes. Close inspection of their time-lapse movies revealed faint structures corresponding to sarcomeric pattern that show up in the frame right before the appearance of sarcomeres. This supports the notion that they are imaging sarcomeres that are coming into focus, and not assembling "*de novo*". To test this idea, we imaged hiCMs with 3D confocal microscopy after they had been plated for 24 hrs (Figure 3-S14). While we also see similar patterns of sarcomeres appearing on the ventral surface as (Chopra et al., 2018), our data revealed these sarcomeres are moving down from the dorsal surface and not assembling on the ventral surface (Figure 3-S17). Of interest, the phenomenon of actin arcs moving down to the ventral surface of non-muscle cells has also been reported previously (Gao et al., 2012; Hotulainen and Lappalainen, 2006). Finally, (Chopra et al., 2018) also claim that neither NMIIA nor NMIIB are required for sarcomere assembly. We also find this strange. While their double NMIIA/NMIIB knockout (KO) cardiomyocyte cell line has α-actinin 2 positive structures, they do not contain continuous labeled Z-lines aligned parallel to each other comparable to the control cell line. The authors did not measure Z-line lengths, spacing, or other criteria needed to define sarcomeres. These discrepancies between our study and theirs, including the role of NMII, need to be harmonized, as it will directly affect our interpretation of future *in vivo* data concerning sarcomere assembly.

Data from *in vivo* studies attempting to answer the question of NMII contribution to sarcomere assembly in mice have been difficult to interpret (Sparrow and Schock, 2009). Germline NMIIA KO mice fail to gastrulate and thus sarcomere assembly is impossible to examine (Conti et al., 2004). A conditional NMIIA KO mouse was generated using a promoter which is activated after heart formation has begun, and no heart defects were noted (Conti et al., 2015). A germline NMIIB KO mouse formed a functional heart, though most pups died before birth due to heart failure (Tullio et al., 1997). Only one high magnification image of the KO animal was shown, which demonstrated severe sarcomere disorganization (Tullio et al., 1997). Of interest, the NMIIB KO animals also showed highly increased NMIIA protein levels compared to controls (Tullio et al., 1997). Thus, the observed capacity of this animal to form sarcomere like structures could be due to genetic compensation by NMIIA. A conditional KO NMIIB mouse has also been made (Ma et al., 2009). While the authors showed an impressive NMIIB KD in the cerebellum via a neuronal specific driver, there were high levels of NMIIB protein in the heart at the time of analysis in the heart specific KO (Ma et al., 2009). In addition, the heart specific conditional KO is driven off of the alpha myosin heavy chain promoter, which switches on after sarcomere assembly has begun and indeed after the heart fields have begun to beat (Ma et al., 2009; Ng et al., 1991). Complicating the issue further, NMIIB has been difficult to localize in tissue. We believe this to be a result of paraffin embedding and subsequent paraffin removal and rehydration protocols. For example, we successfully localized NMIIB in formalin fixed human and mouse tissue (Figures 3-10 and 3-S15), but failed to localize NMIIB in paraffin embedded tissue.

Future comparisons between *in vivo* and *in vitro* data sets will need to be addressed. Intriguing and unanswered questions also remain to be tested. For example, how are the observed gradients of NMII and βCMII in cardiac myocytes established and maintained? Such questions have been previously difficult to impossible to test due complicated and technically challenging model systems. Importantly, we present a relatively easy to use model system to test these questions. The hiCMs we use in this study are commercially available for purchase. Our Methods outline protocols to transfect with DNA for protein expression and siRNA for protein knockdown, and trypsinization protocols for re-plating. Going forward, we believe studies using the experimental setup we describe here will not only clarify previous models but also reveal new insights into both sarcomere assembly, and cardiac cell biology.

Supplemental figures

Figure 3-S1

A Actin and βCMII at 1.5hrs (top) and 24hrs (bottom) post-plating

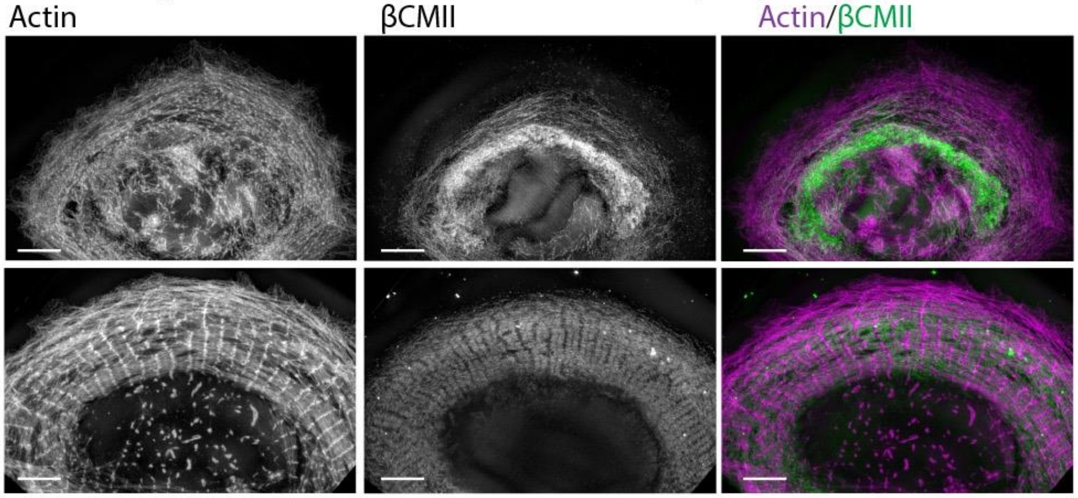

B Actin and α-Actinin 2 at 1.5hrs (top) and 24hrs (bottom) post-plating

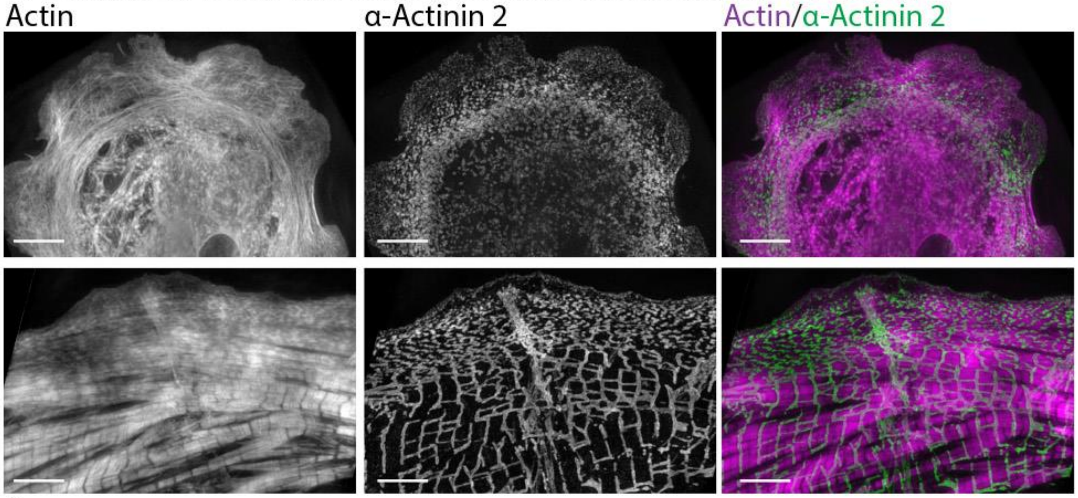

C Actin and TroponinT at 1.5hrs (top) and 24hrs (bottom) post-plating

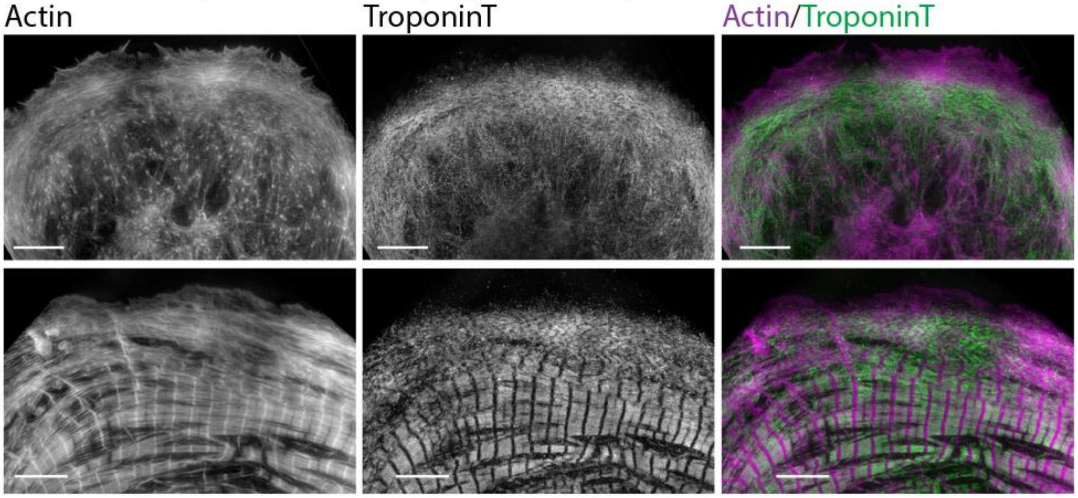

Figure 3-S1: hiCMs don't contain sarcomeres at early time points post plating (A) hiCM stained for actin and βCMII and imaged with SIM at 1.5 hours (top) and 24 hours (bottom) following trypsinization. (B) hiCM stained for actin and α-actinin 2 and imaged with SIM at 1.5 hours (top) and 24 hours (bottom) following trypsinization. (C) hiCM stained for actin and TroponinT and imaged with SIM at 1.5 hours (top) and 24 hours (bottom) following trypsinization. Note how hiCMs at 1.5 hours contain Muscle Stress Fibers (MSFs), but contain neither actin nor βCMII based sarcomeres. hiCMs at 24 hours however contain prominent sarcomere structures. Scale bars, 5 µm.

Figure 3-S2

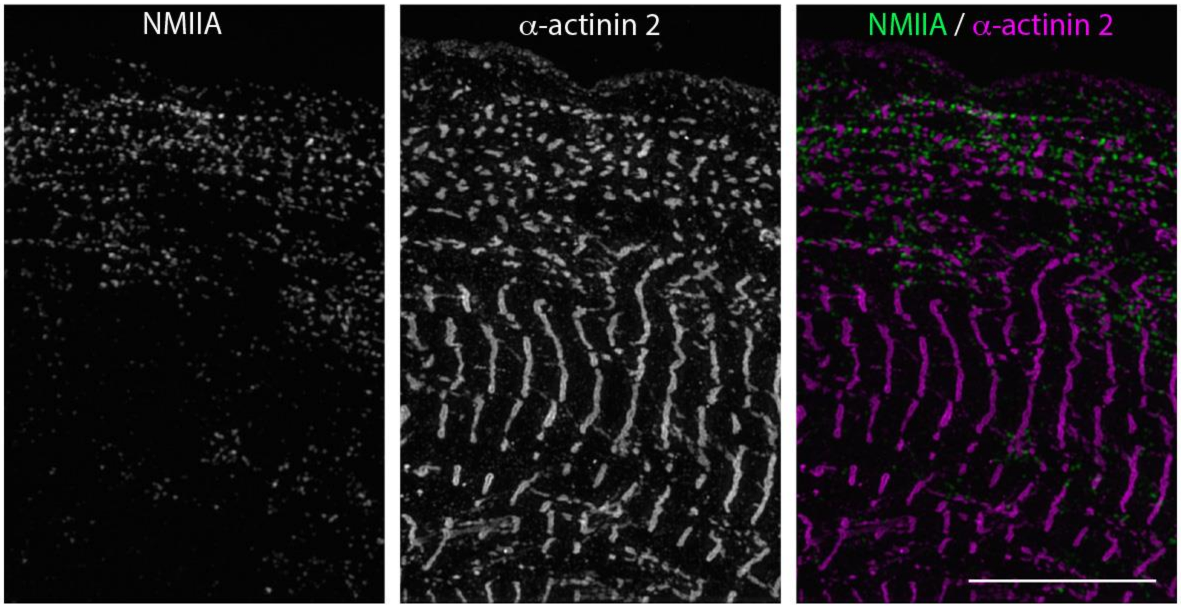

Figure 3-S2: SIM of NMIIA and α-actinin 2 localizations in hiCM
NMIIA localizes to MSFs but is excluded from sarcomeres (see Figure 3-7). NMIIA is found between small α-actinin 2 puncta in MSFs at edge of hiCM (alternating green and magenta in right image), and is excluded from large α-actinin 2 Z-lines in hiCM body. Scale Bar: 10 μm.

Figure 3-S3

Actin filaments in a hiCM spreading in the presence of SMIFH2

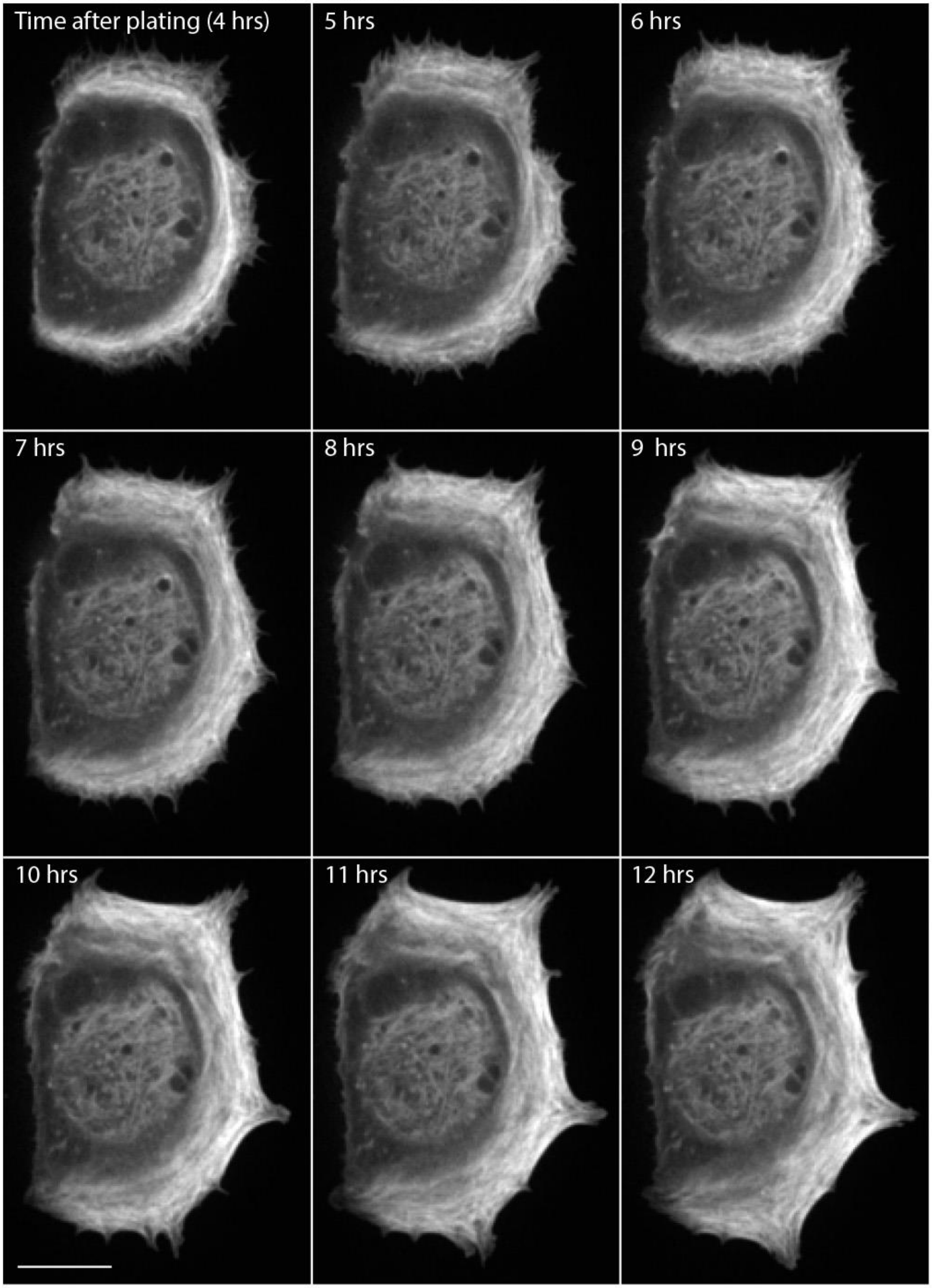

Figure 3-S3: hiCM spreading in the presence of 25 µM SMIFH2
Spinning-disk confocal microscopy of hiCM expressing Lifeact-mApple and spreading in the presence of 25 µM SMIFH2 (added 1.5 hours post plating). Note sarcomeres do not form in the presence of 25 µM SMIFH2. Scale Bar; 20 µm.

Figure 3-S4

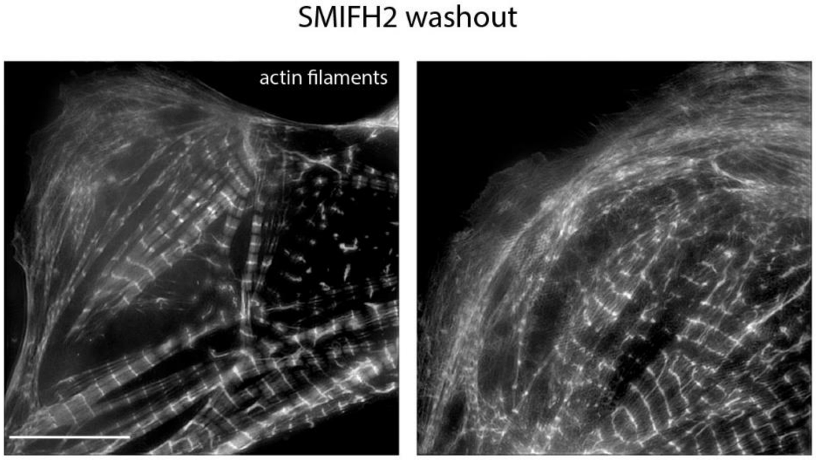

Figure 3-S4: hiCMs assemble sarcomeres following washout of SMIFH2
Examples of two hiCMs containing MSFs and sarcomeres following washout of 25 µM SMIFH2 and imaged with SIM. hiCMs were spread in 25 µM SMIFH2 (as in Figure 3-6) for 24hrs, and fresh media without drug was exchanged. hiCMs were subsequently allowed to spread for an additional 24 hours before fixation. Scale Bar; 10 µm.

Figure 3-S5

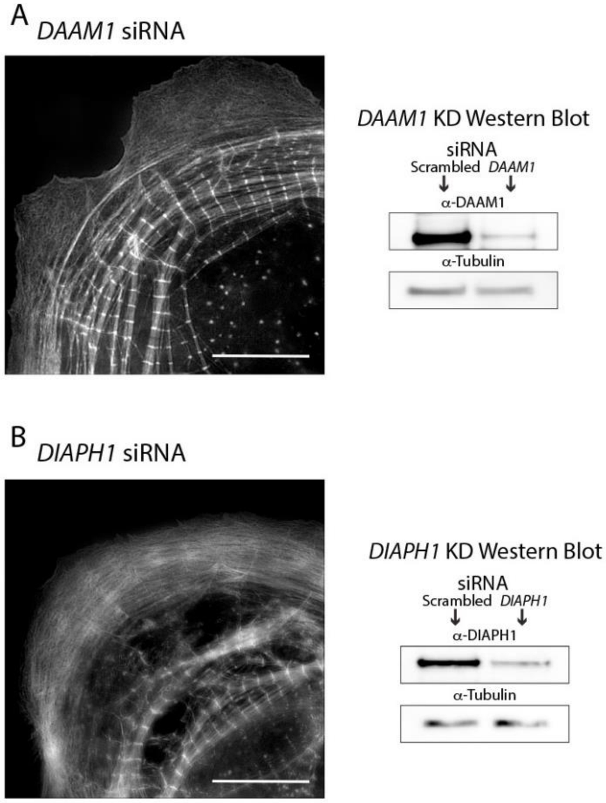

Figure 3-S5: hiCMs assemble sarcomeres following knockdown (KD) of DAAM1 and DIAPH1
(A) siRNA *DAAM1* hiCM spread for 24 hours stained for actin, and imaged with SIM (left). DAAM1 KD hiCMs still assemble sarcomeres, and have extended lamellipodia. Representative western blot showing KD of DAAM1 protein (right). (B) siRNA *DIAPH1* hiCM spread for 24 hours, stained for actin and imaged with SIM (left). DIAPH1 KD hiCMs appear to have fewer sarcomeres than scramble control hiCMs, but still assemble sarcomeres. Representative western blot showing KD of DIAPH1 protein (right). Scale Bars; (A), (B), 10 µm.

Figure 3-S6

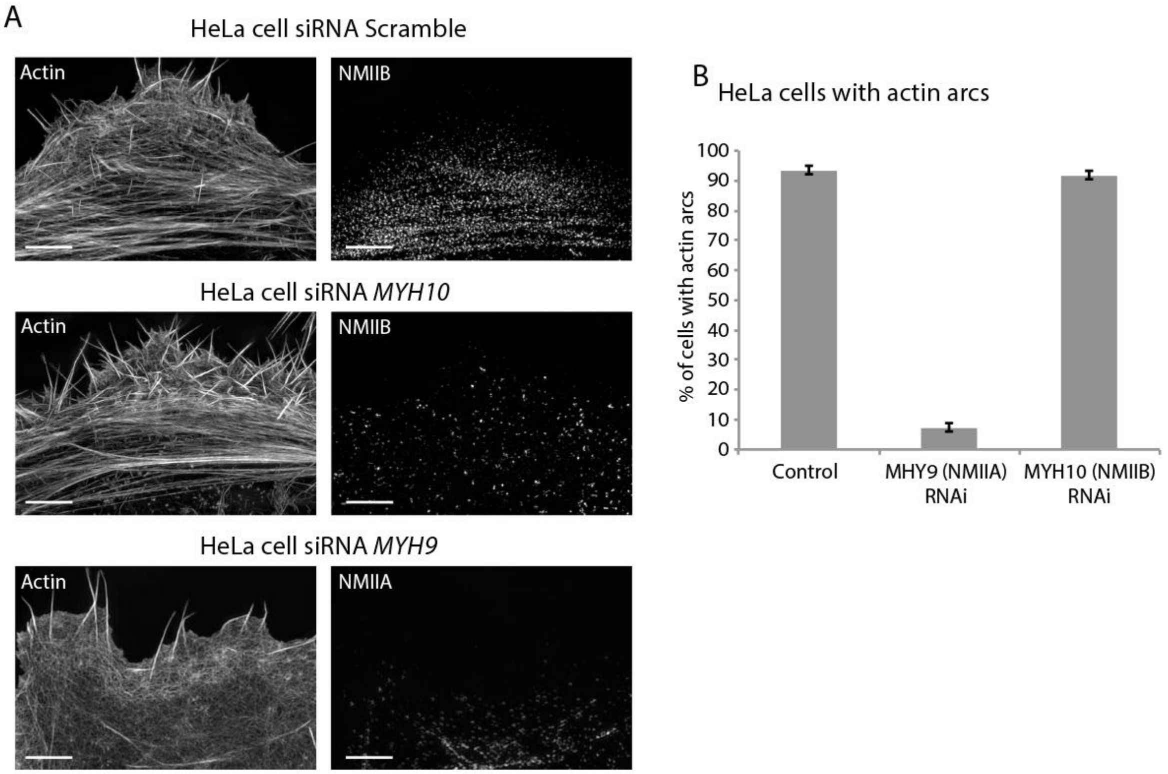

Figure 3-S6: NMIIA but not NMIIB is required for actin arc formation in HeLa cells. (A) HeLa cells treated with control, anti *myh10*, or anti *myh9* (top, middle, bottom, respectively) siRNA, stained for actin, and imaged with SIM. Note how control and NMIIB KD cells display prominent actin arc stress fibers, but NMIIA KD cells contain no actin arcs. (B) Quantification of HeLa cells with actin arc stress fibers in indicated conditions. Scale Bars: 5 µm.

Figure 3-S7

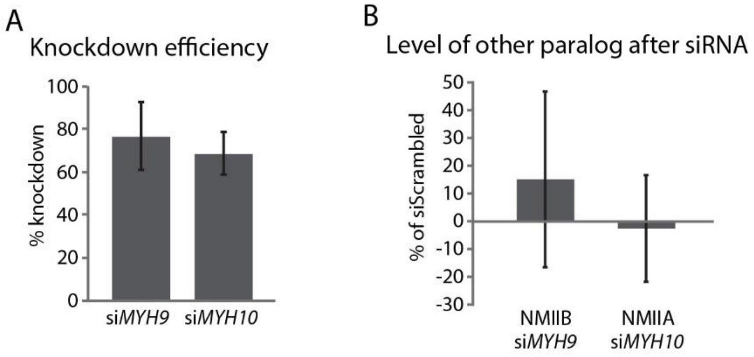

Figure 3-S7: Knockdown of NMIIA and NMIIB in hiCMs
(A) Quantification from western blots showing KD of NMIIA (si*MYH9*) and NMIIB (*siMYH10*) in hiCMs compared to scramble control. N = 3 for each condition. (B) Quantification of NMIIB levels in *siMYH9* hiCMs (left) and NMIIA levels in *siMYH10* hiCMs (right) compared to scramble control. N = 3 for each condition.

Figure 3-S8

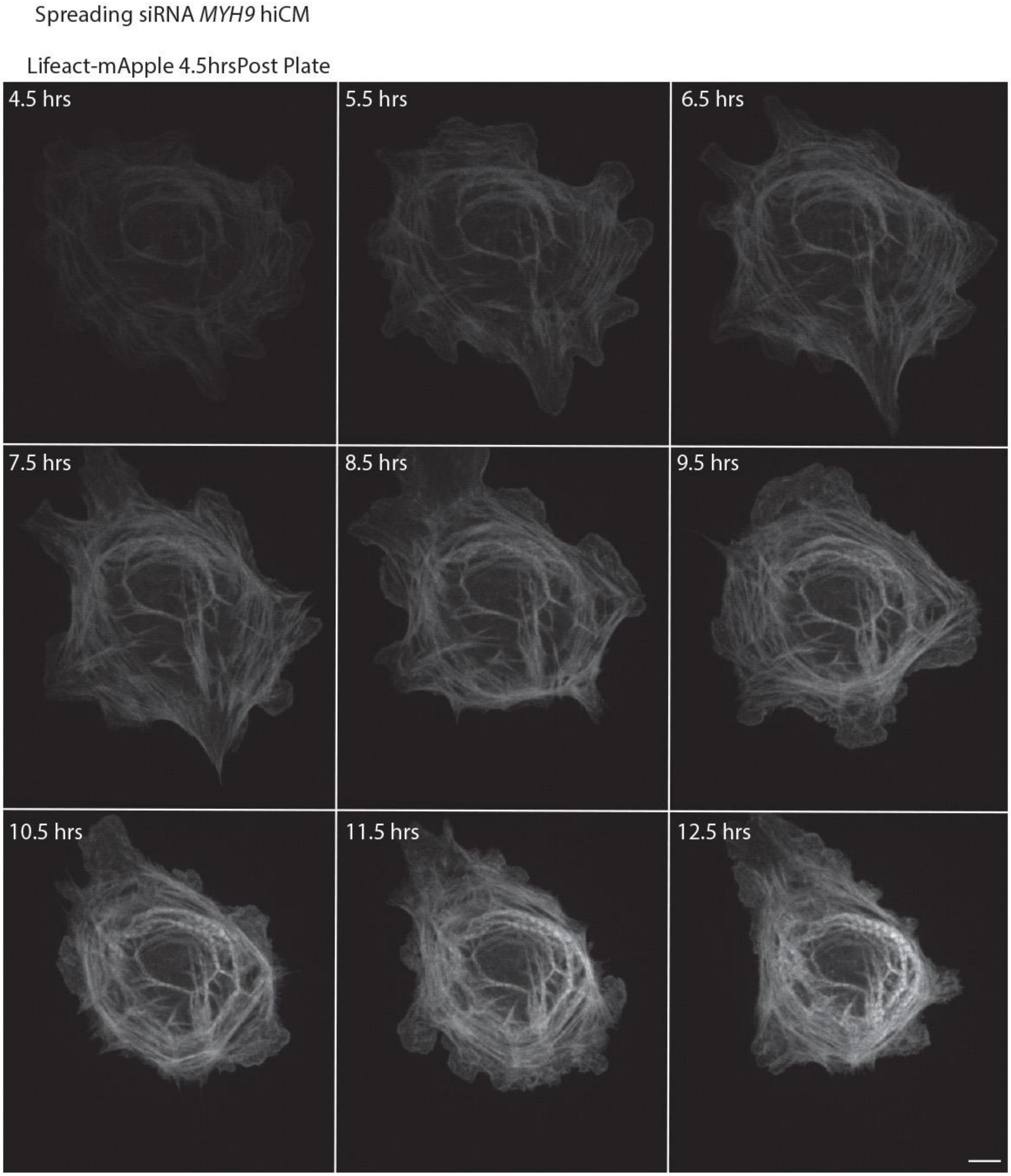

Figure 3-S8: Live montage of spreading NMIIA KD hiCM
Laser-scanning confocal of spreading NMIIA KD hiCM expressing Lifeact-mApple. NMIIA KD hiCM is able to assemble sarcomere structures. Scale Bar; 10 µm.

Figure 3-S9

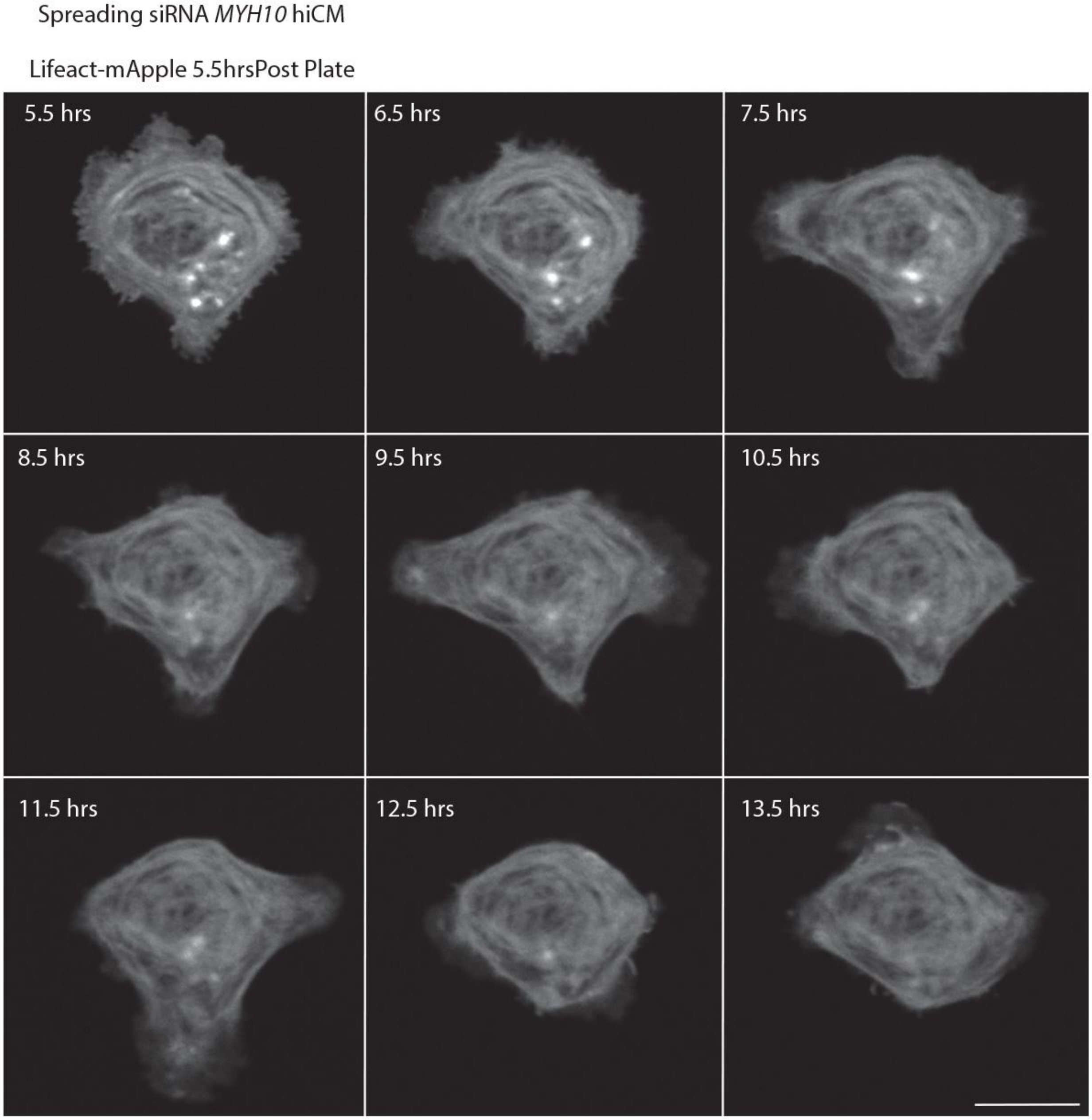

Figure 3-S9: Live montage of spreading NMIIB KD hiCM
Laser-scanning confocal of spreading NMIIB KD hiCM expressing Lifeact-mApple. NMIIB KD hiCM does not form sarcomeres. Scale Bar; 20 µm.

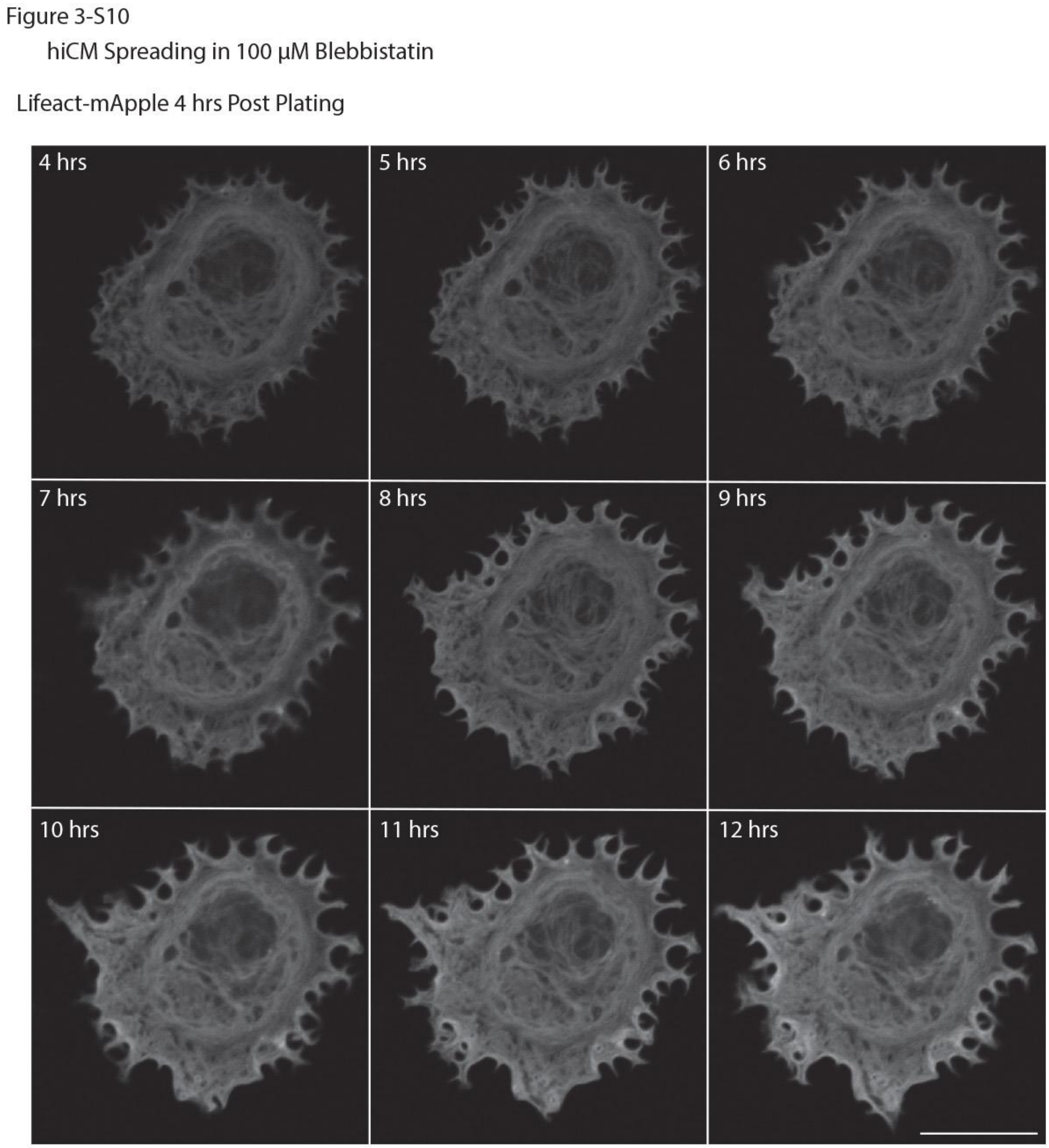

Figure 3-S10: Live montage of hiCM spreading in 100 µM blebbistatin
Laser-scanning confocal of hiCM spreading in the presence of 100 µM blebbistatin added 1.5 hrs post plating. hiCM does not assemble sarcomeres in the presence of 100 µM blebbistatin. Scale Bar; 20 µm.

Figure 3-S11

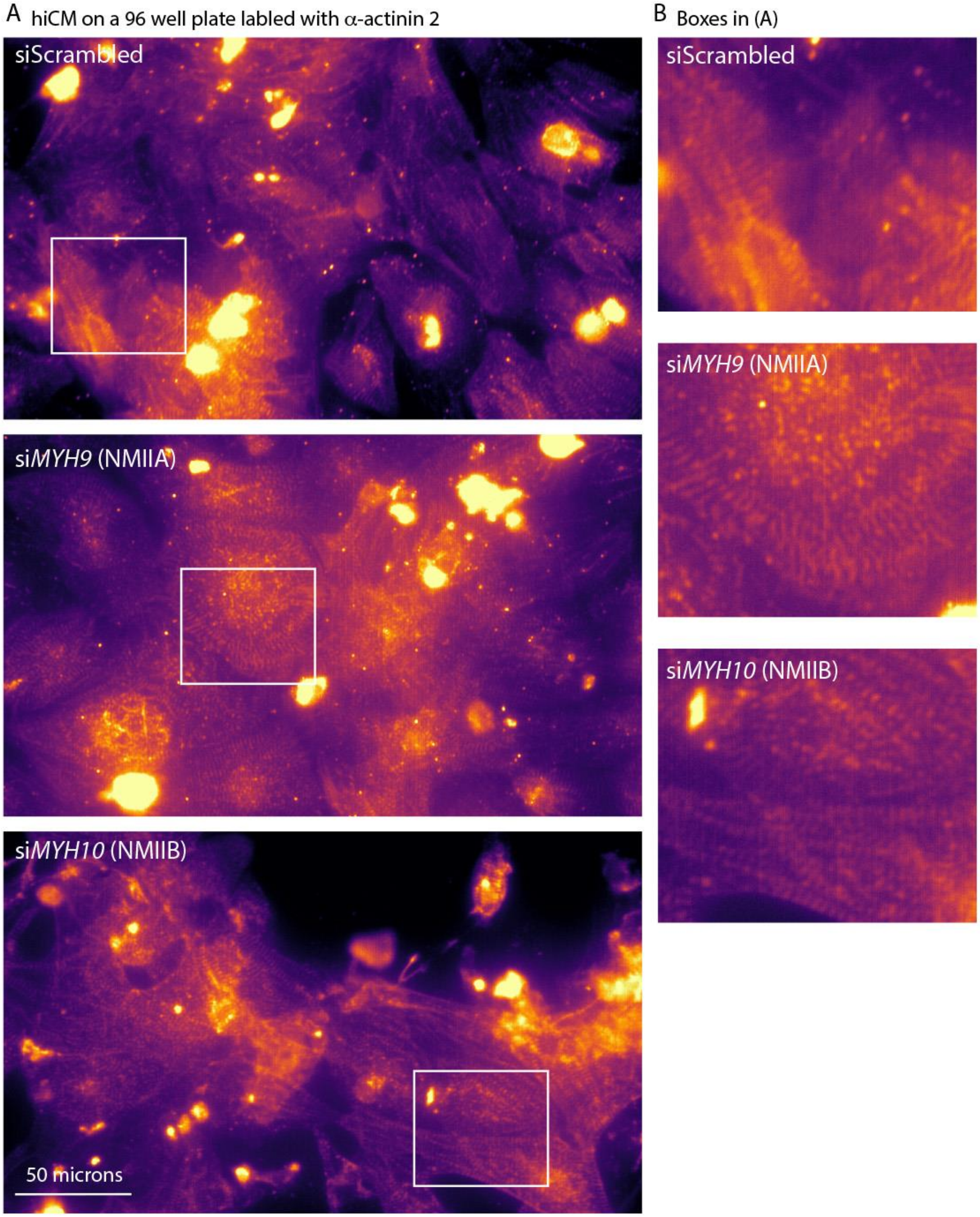

Figure 3-S11: NMIIA KD and NMIIB KD hiCMs contain sarcomeres before plating

(A) siScrambled (top) si*MYH9* (NMIIA KD, middle), and si*MYH10* (NMIIB KD, bottom) hiCMs treated in 96 well plates, fixed, and localized for α-actinin 2 imaged with wide-field microscopy. hiCMs were allowed to attach for 4 days (as per manufacturer's recommendation, see Methods), ensuring robust sarcomere assembly before siRNA treatment began. Note all conditions contain sarcomeric staining of α-actinin 2. Look up table is mpl-magma in (Fiji is Just) ImageJ.

Figure 3-S12

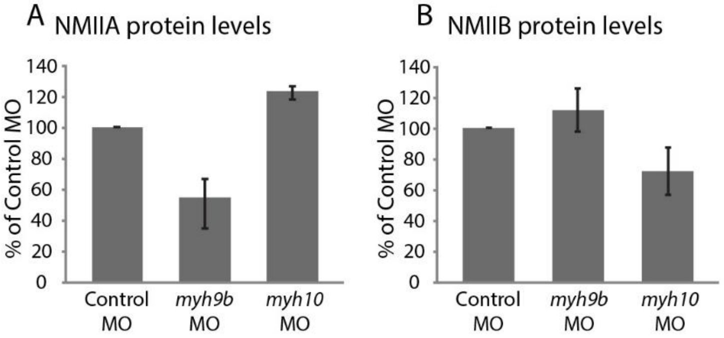

Figure 3-S12: Knockdown of NMIIA and NMIIB in Zebrafish
(A) Quantification from western blots of NMIIA protein levels in indicated condition compared to control MO. N = 3 for each condition. (B) Quantification of NMIIB levels in indicated condition compared to control MO. N = 3 for each condition.

Figure 3-S13

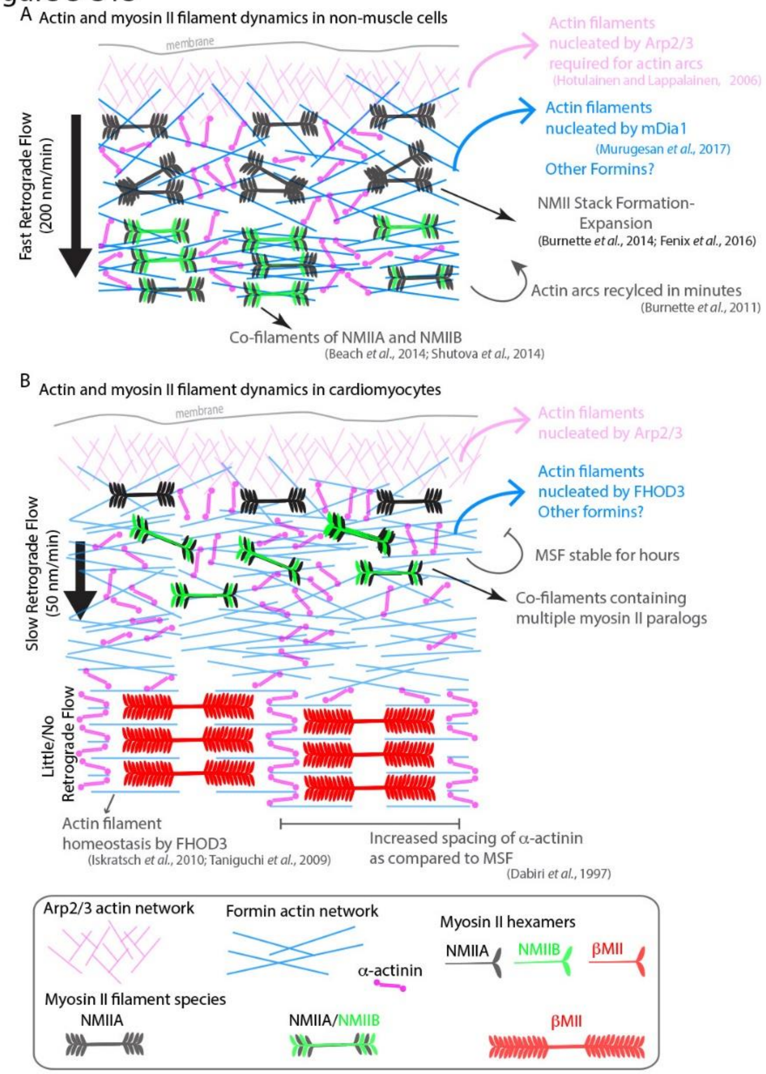

Figure 3-S13: Model of actomyosin stress fiber formation in non-muscle cells and human cardiomyocytes

(A) Actin and myosin II stress fiber formation in non-muscle cells. Actin stress fibers are formed via the Arp2/3 complex and the formin mDia1. NMIIA is the predominant isoform at the leading edge of non-muscle cells, and stress fiber formation is NMIIA dependent. Non-muscle cells display robust retrograde flow of actin stress fibers and display rapid turnover. Large NMIIA stacks are formed via growth and expansion of smaller NMIIA filaments. Citations leading to this model are presented in the cartoon. (B) Model of actin-based stress fiber formation in human cardiomyocytes. Sarcomeres are templated by Muscle Stress Fibers (MSFs). MSFs do not require the Arp2/3 complex, and require the formin FHOD3. MSFs display slow retrograde flow compared with non-muscle stress fibers. Both NMIIA and NMIIB are localized to the edge of hiCMs, and display prominent NMII co-filaments.

Figure 3-S14

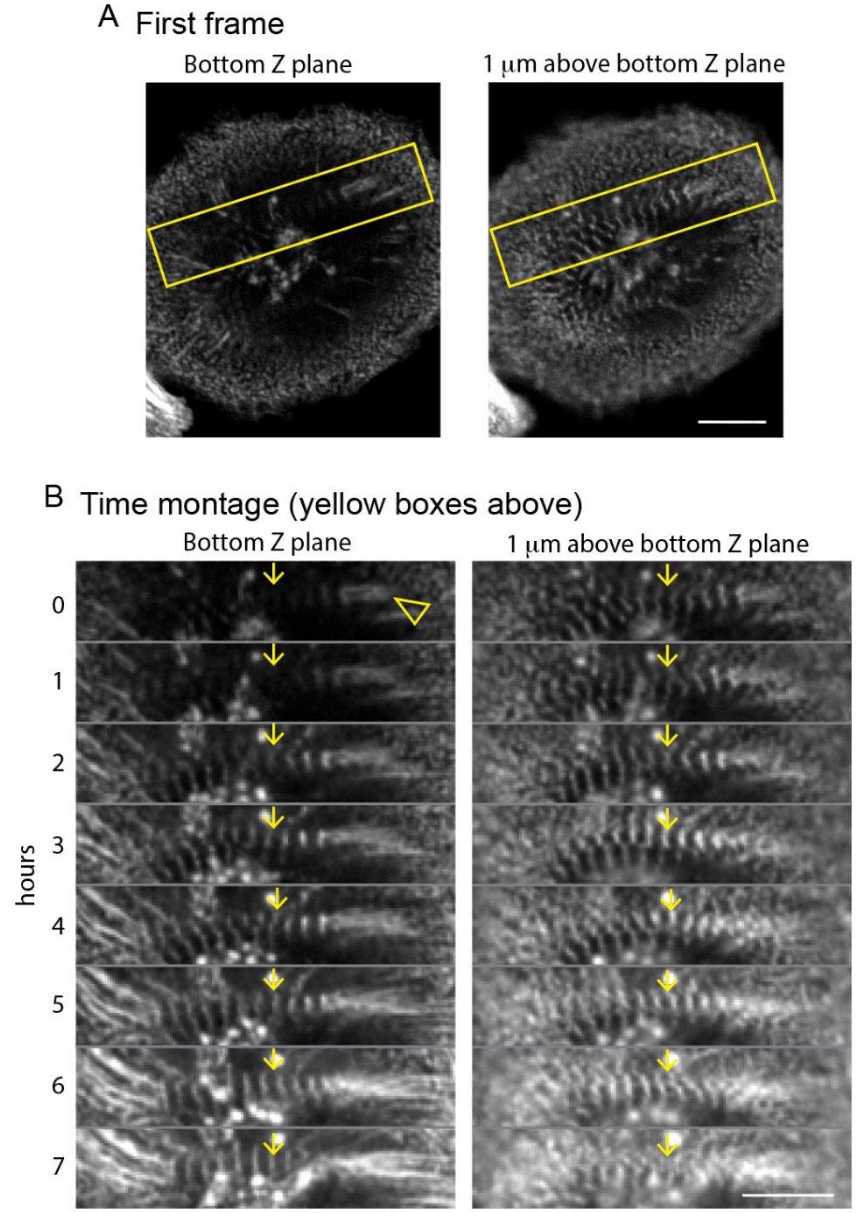

Figure 3-S14: Sarcomeres form on dorsal surface of hiCMs and subsequently move towards ventral surface

(A) hiCM expressing α-actinin 2-mCherry plated for 24 hours and imaged with laser-scanning confocal. Note that when viewing the ventral (bottom) surface (left image), no sarcomeric pattern of α-actinin 2 can be seen. However, when viewing the dorsal (top) surface of the cell (right image), sarcomeres are clearly present. (B) Time montage from yellow box in (A). Myofibril from top of the cell (right montage, yellow arrow) moves towards the bottom of the cell (left image, yellow arrow). Arrow head (left montage) denotes α-actinin 2 containing adhesion.

Figure 3-S15

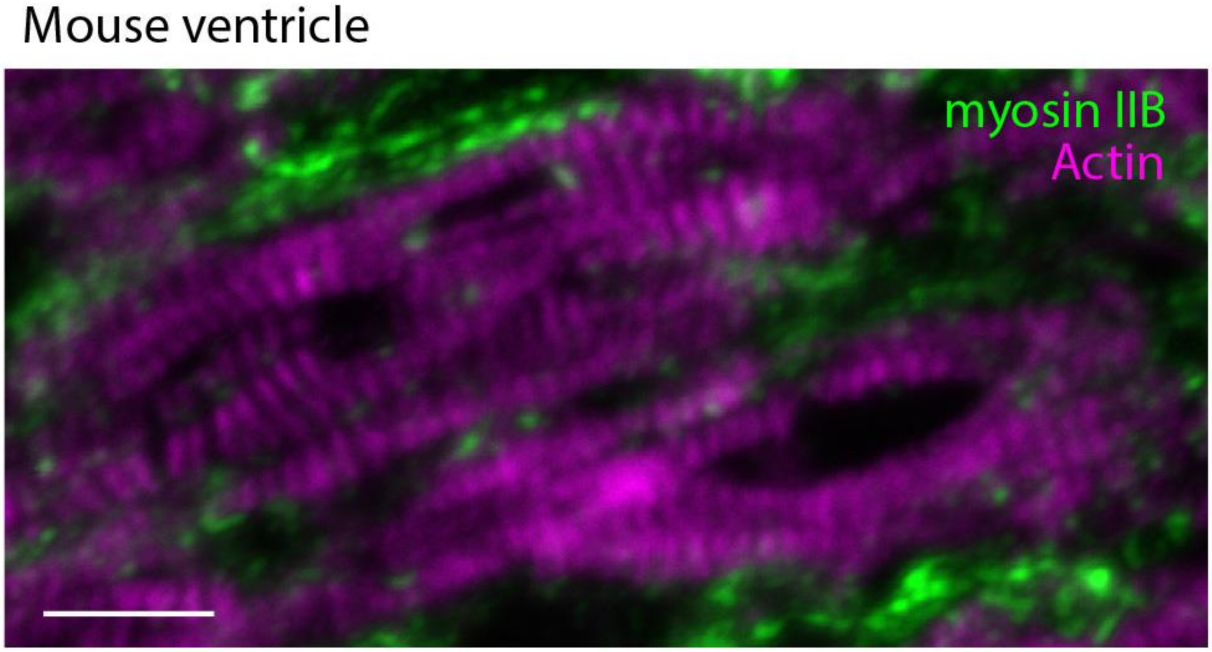

Figure 3-S15: NMIIB localization *in vivo*
Localization of NMIIB and actin in tissue slice from heart ventricle of P3 mouse and imaged with laser-scanning confocal. Green arrows denote strong localization of NMIIB outside of but adjacent to sarcomere structures as in hiCMs (Figures 7A and 10A). Scale Bar: 10 µm.

Chapter IV

Dynamics of A-band assembly in cardiac myocytes

Aidan M. Fenix, Mike R. Visetsouk, Abigail C. Neininger, Nilay Taneja, Ryan J. Garde, Baohong Liu, Benjamin R. Nixon, Annabelle E. Manalo, Jason R. Becker, Scott W. Crawley, David M. Bader, Matthew J. Tyska, Qi Liu, Jennifer H. Gutzman, Dylan T. Burnette

Introduction

Our work in sarcomere assembly thus far has focused on the actin cytoskeleton within cardiac myocytes (Chapter III). However, beta cardiac myosin II (βCMII) filaments also represent a major structural and functional protein within cardiac myocytes. βCMII filaments bind to and pull on actin filaments to generate force within cardiac myocytes, a process referred to as “sarcomere shortening”. On a structural level, we know βCMII filaments form large βCMII filament stacks which make up the core of the sarcomere (FIGURE 3-1). This structure is referred to as the A-band. Despite a wealth of structural and functional data surrounding βCMII filaments, how an organized stack of βCMII filaments (i.e., the A-band) is dynamically assembled is unknown. This information is crucial, as mutations in βCMII are the leading cause of inherited hypertrophic cardiomyopathies (HCM). A more thorough understanding of βCMII filament dynamics during sarcomere assembly would allow for a better understanding of how HCM causing mutations are affecting sarcomere assembly and function. Thus, we sought to utilize our sarcomere assembly assay (presented in Chapter III), and build upon previous work investigating how a similar myosin, non-muscle myosin IIA (NMIIA, presented in

Chapter II), to investigate how βCMII filament stacks are assembled in human cardiac myocytes.

Results

NMII and FHOD3 are required for organized A-band formation

Thus far, our results highlight the importance of formin-mediated actin polymerization and NMII for proper actin filament architecture during sarcomere assembly (Chapter III). We next wanted to address how the thick, β Cardiac Myosin II (βCMII) filaments at the core of the sarcomere (i.e., A-band, Figure 3-1) assemble. Therefore, we started by localizing endogenous βCMII and NMIIB filaments (Figure 4-1). βCMII predominately localized behind NMIIB in organized sarcomere structures and showed a peak localization ~15 microns behind the leading edge of the cell, with a slight area of overlap with NMIIB (Figure 4-1). We noted that the area of overlap contained NMIIB-βCMII co-filaments (Figure 4-1 and 4-S1). In addition, we also found NMIIA-βCMII co-filaments in hiCMs (Figure 4-S2). To our knowledge, this is the first time a myosin II species has been reported that contains a non-muscle and muscle paralog inside cells. Furthermore, we also found NMIIB-βCMII co-filaments in mouse and human heart tissue, indicating NMIIB-βCMII co-filaments are present *in vivo* (Figures 4-1 and 4-S1). The co-filaments containing NMIIB and βCMII were of similar length to NMIIA/B filaments (Figure 4-1). Indeed, we noticed that near the leading edge of the cell, βCMII filaments are typically smaller and not organized into stacks resembling A-bands (Figure 4-1). This suggests βCMII filaments are polymerized at the edge and subsequently grow larger as they move away from the leading edge (Figure 4-1). The presence of NMII before βCMII filaments grow into larger filaments led us to test the hypothesis that NMII would play a role in βCMII filament formation.

To test if NMII was also required for βCMII filament and A-band formation, we depleted hiCMs of NMIIB and localized βCMII 24 hours after plating. Compared to control hiCMs, NMIIB KD hiCMs displayed a significant decrease in the ability to form A-band-like structures and a reduced overall number of βCMII filaments (Figure 4-1). Although βCMII filaments formed, they were highly disorganized compared to control cells, as assessed by Fourier transform (Pasqualini et al., 2015) (Figure 4-1). As NMIIB KD results in highly disorganized actin filament architecture, we asked if βCMII was using residual actin filaments as a template to polymerize.

To test if actin was serving as a template for βCMII filament formation, we sought to remove all the actin filaments in hiCMs. To do so, we allowed hiCMs to form sarcomeres for 18 hours, then treated hiCMs with the actin monomer sequestration agent Latrunculin B for 6 hours in order to disassemble actin filaments acutely before fixation (Spector et al., 1983; Wakatsuki et al., 2001). Latrunculin B-treated hiCMs showed a lack of actin-based sarcomeres, and no βCMII filament stacks, but conspicuous βCMII filament aggregates (Figure 4-1). These results argue that actin filaments are required for the organization of βCMII filaments of the A-band. As both FHOD3 and NMIIA KDs also resulted in disorganized actin filament architecture, we localized βCMII in these conditions. Both conditions also resulted in disorganized βCMII filaments compared to control hiCMs (Figure 4-S3).

Figure 4-1

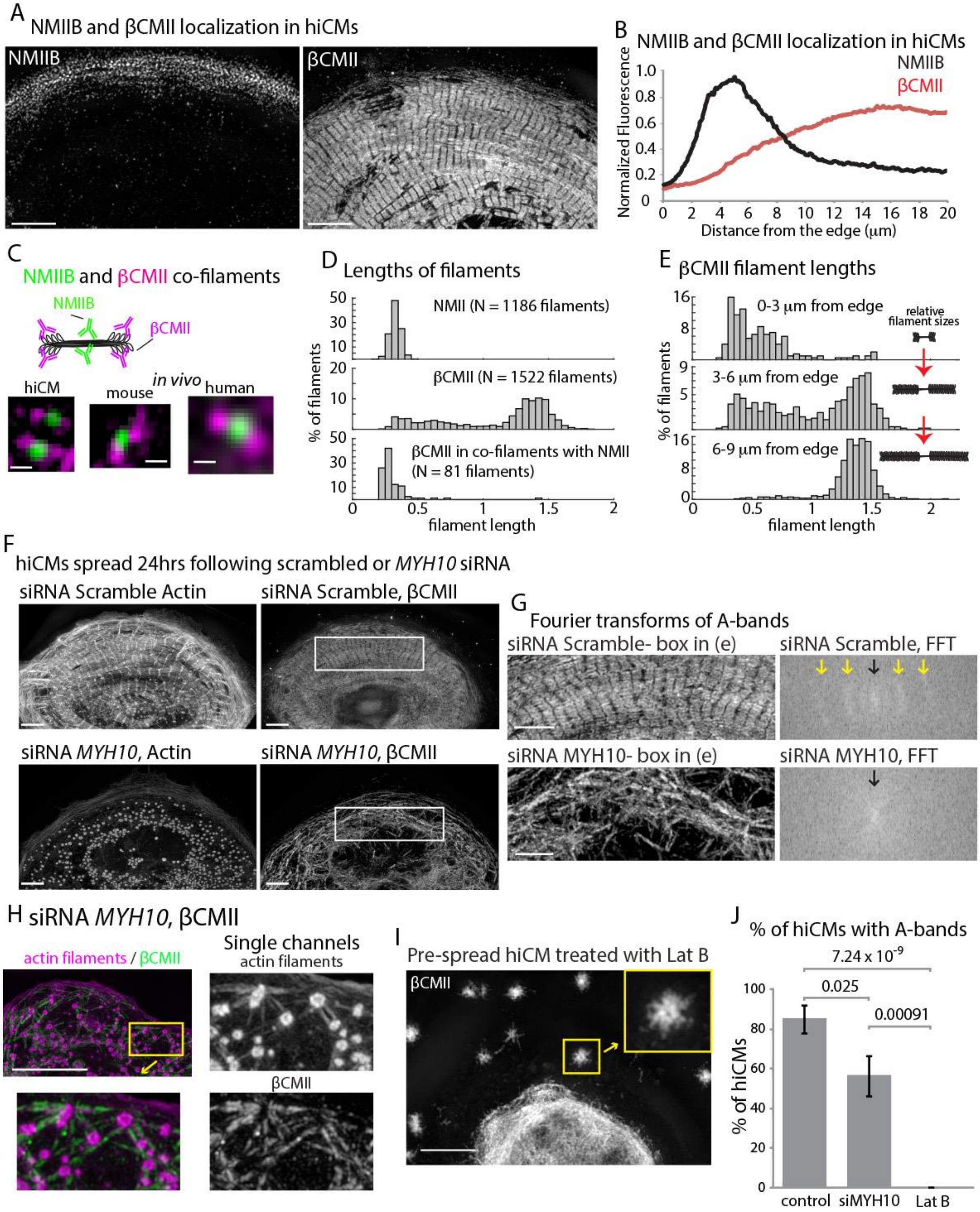
A
NMIIB and βCMII localization in hiCMs
NMIIB
βCMII
B
NMIIB and βCMII localization in hiCMs
NMIIB
βCMII
Normalized Fluorescence
1.0
0.8
0.6
0.4
0.2
0
0 2 4 6 8 10 12 14 16 18 20
Distance from the edge (μm)
C
NMIIB and βCMII co-filaments
NMIIB
βCMII
hiCM
mouse
in vivo
human
D
Lengths of filaments
NMII (N = 1186 filaments)
βCMII (N = 1522 filaments)
βCMII in co-filaments with NMII (N = 81 filaments)
% of filaments
filament length
E
βCMII filament lengths
0-3 μm from edge
3-6 μm from edge
6-9 μm from edge
relative filament sizes
% of filaments
filament length
F
hiCMs spread 24hrs following scrambled or MYH10 siRNA
siRNA Scramble Actin
siRNA Scramble, βCMII
siRNA MYH10, Actin
siRNA MYH10, βCMII
G
Fourier transforms of A-bands
siRNA Scramble- box in (e)
siRNA Scramble, FFT
siRNA MYH10- box in (e)
siRNA MYH10, FFT
H
siRNA MYH10, βCMII
actin filaments / βCMII
Single channels
actin filaments
βCMII
I
Pre-spread hiCM treated with Lat B
βCMII
J
% of hiCMs with A-bands
7.24 x 10^-9
0.025
0.00091
% of hiCMs
100
80
60
40
20
0
control
siMYH10
Lat B

Figure 4-1: β Cardiac Myosin II (βCMII) Filament Assembly in hiCMs
(A) Endogenous localization of NMIIB (left) and βCMII in the same hiCM and imaged with SIM. (B) Averaged line-scans of NMIIB (Figure 3-7 and βCMII localization in hiCMs spread for 24 hours. Note the peak fluorescence of βCMII is more towards the cell body than peak fluorescence of NMIIB. 23 cells from 4 experiments were used for βCMII localization. (C) Schematic (top) of NMIIB-βCMII co-filaments in hiCMs. High-mag views of βCMII-NMIIB co-filaments in hiCMs (left) imaged with SIM. Endogenous staining of hiCM (bottom, left) for βCMII (N-terminal motors) and NMIIB (rod domain). Mouse and human tissue (bottom middle, and bottom right, respectively) stained for βCMII (motors) and NMIIB (rod domain) and imaged using Zeiss 880 with Airyscan. (D) Histograms displaying width of NMII filaments (top), βCMII filaments (middle), and NMIIB-βCMII co-filaments in hiCMs. Measurements made from motor-domain to motor domain as in Figure 3-7. (E) Histograms displaying distribution of βCMII filaments widths with respect to their location in hiCMs. Note βCMII filaments tend to grow larger as they move towards the center of the cell. Measurements were not taken from "mature" sarcomere structures in highly organized A-bands. (F) Actin and βCMII of scramble control hiCM (top) and NMIIB KD (si*MYH10*) hiCM (bottom) spread for 24 hours. Note loss of organized A-bands but presence of βCMII filaments in NMIIB KD hiCM. (G) Fourier transforms of βCMII signal from white boxes in Figure 4-1 from scramble control and NMIIB KD hiCMs (above and below respectively). Yellow arrows indicate sarcomeric periodicity in scramble control hiCMs, which is lacking in NMIIB KD cells. (H) High mag views of actin and βCMII in NMIIB KD (siRNA *MYH10*) hiCM imaged with SIM. βCMII filaments localize to residual actin filaments. (I) βCMII in hiCM spread for total of 24hrs, with final 6 hours in 5 µM Latrunculin B and imaged with SIM. Notice lack of βCMII A-bands, and large βCMII filament aggregates (yellow box). (J) Percentage of scramble control, NMIIB KD (siRNA *MYH10*), and 5 µM Latrunculin B hiCMs with βCMII A-bands. Control: 26 cells, 3 experiments; NMIIB KD: 26 cells, 2 experiments; Latrunculin B: 11 cells, 3 experiments. Scale Bars; (A), (H), (I) 10 µm, (C) 200 nm, (F), (G), 5 µm. P-values denoted in graphs.

Dynamics of A-band assembly

To further investigate the mechanisms of A-band assembly, we created a full length, human βCMII construct containing a mEGFP tag on the motor domain (i.e., N-terminal) (Figure 4-2). This construct properly integrated into both single filaments and more mature myofibrils (Figure 4-2). In non-muscle U2OS cells, A-band-like stacks of NMIIA filaments are often formed through a process called “Expansion” (Fenix et al., 2016). During Expansion, NMIIA filaments that are close to each other (i.e., in a tight bundle) move away from each other in space but remain part of the same ensemble, where they are aligned in a stack similar to muscle myosin II in the A-band. In addition to Expansion, NMIIA filaments also, but more rarely, “Concatenated” (Fenix et al., 2016). Concatenation is defined by spatially separated NMIIA filaments moving towards one another to create a stack. To test how βCMII filament stacks form, we repeated our live-cell sarcomere formation assay using our βCMII-mEGFP construct. In contrast to our previous results with NMIIA, we found the major physical mechanism of βCMII filament stack formation to be concatenation, where pre-existing βCMII filaments ran into one another and stitched together to form the A-band (Figure 4-2). A small percentage of hiCMs showed an expansion event of βCMII-mEGFP, however this was significantly less frequent than in non-muscle cells and did not appear to result in a more organized A-band (Figure 4-2). Indeed, each of the hiCMs quantified in Figure 1 showed only 1 expansion event.

Figure 4-2

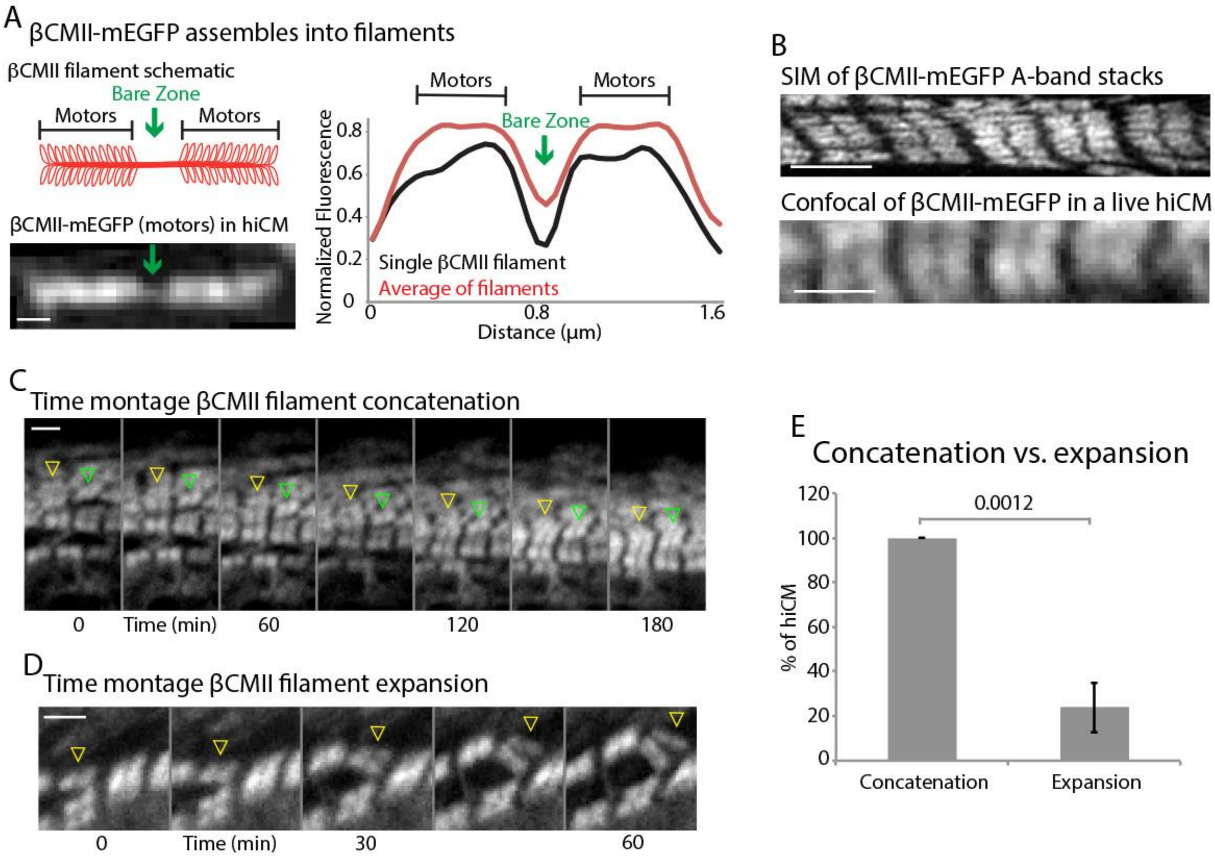

Figure 4-2: βCMII filaments concatenate to form larger A-band structures

(A) Cartoon of βCMII filament (left, above). N-terminal tagged human βCMII-mEGFP filament expressed in hiCM (left, below). Gap in signal represents bare-zone lacking motors (green arrows). βCMII single filament and A-band filament (βCMII filaments found within organized A-bands) widths measured by line scans (right). βCMII Filaments: 16 filaments, 3 experiments. βCMII myofibrils: 28 myofibrils, 3 experiments. Note more level “plateau” of signal from motors in A-band βCMII filaments. (B) SIM of representative βCMII-mEGFP myofibril in hiCM (top) and laser scanning confocal (bottom). (C) Representative montage showing two separate concatenation events. Yellow arrowhead denotes a large stack of βCMII-mEGFP filaments concatenating with a smaller stack of βCMII-mEGFP filaments as they undergo retrograde flow. Green arrowhead denotes smaller βCMII-mEGFP filament concatenating with larger βCMII-mEGFP stack as they undergo retrograde flow. Both events result in larger and more organized βCMII-mEGFP filament stack (i.e. the A-band). (D) Example of βCMII-mEGFP filament splitting event. Note how small βCMII-mEGFP stack splits to create 2 smaller βCMII-mEGFP filaments and does not result in larger or more organized βCMII-mEGFP filament stacks. (E) Quantification of % of hiCMs which display concatenation or expansion events of βCMII filaments. Scale Bars; (A) 200 nm, (B), (C) and (D) 2 µm. P-values denoted in graph.

Discussion

This work is in part, inspired by Chapter II, and builds upon the work in Chapter III to create a fuller pictures of sarcomere assembly. In addition to showing NMIIA and NMIIB were required for sarcomere assembly (Chapter III), we show NMIIA and NMIIB form myosin II co-filaments with βCMII. βCMII filaments found in co-filaments were relatively small, (~300nm), and subsequently grew larger as they transitioned to the larger filaments of the A-band (~1.6 microns), and lost NMII. Furthermore, in support of a Template Model, our data suggests that NMIIA/B filaments could be themselves a template for the addition of βCMII as all three paralogs can be found in co-filaments together in the region where NMIIA/B and βCMII overlap. A-band assembly was perturbed in FHOD3 KD, NMIIA KD, and most strongly in NMIIB KD hiCMs. Complete removal of the actin cytoskeleton resulted in a loss of βCMII filaments.

At the beginning of this work, we expected βCMII filaments to expand to form βCMII filament stacks. Previously, we had shown NMIIA expands to form NMIIA stacks (Chapter II) Surprisingly, we found individual βCMII filaments (or a small bundle below the resolution limit of our imaging modality) concatenate to form the βCMII filament stacks of the A-band. This process requires the presence of actin tracks. This result demands certain aspects of βCMII dynamics warrant comparison to the Stitching Model (reviewed in Introduction and Chapter III). Though we did not detect I-Z-I-Bodies and myosin II filaments stitching together, we found separate βCMII filaments concatenated and “stitched” together to form larger βCMII filament stacks (i.e., the A-band) (Figure 3-11). Thus, we can add βCMII stack assembly to our model of sarcomere assembly presented in Chapter III (Figure 4-S4).

Supplementary figures

Figure 4-S1

A

βCMII (motors) and NMIIB (rods) at the edge of hiCM

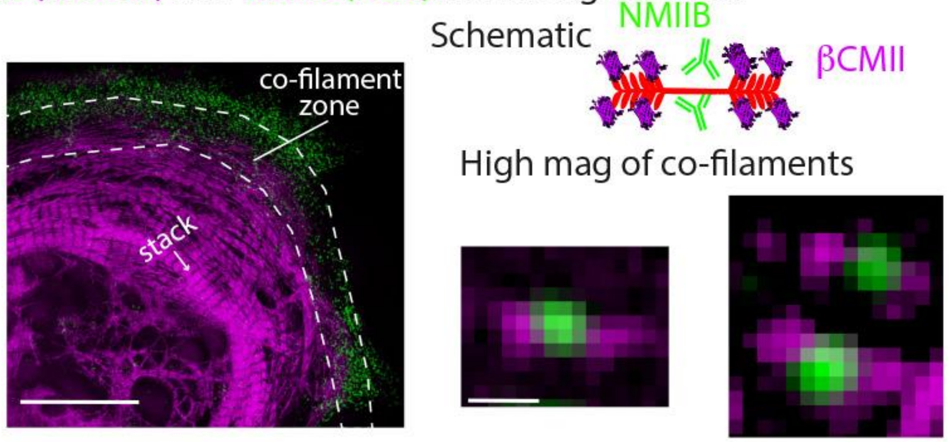

B

βCMII (motors) and NMIIB (rods) *in vivo*

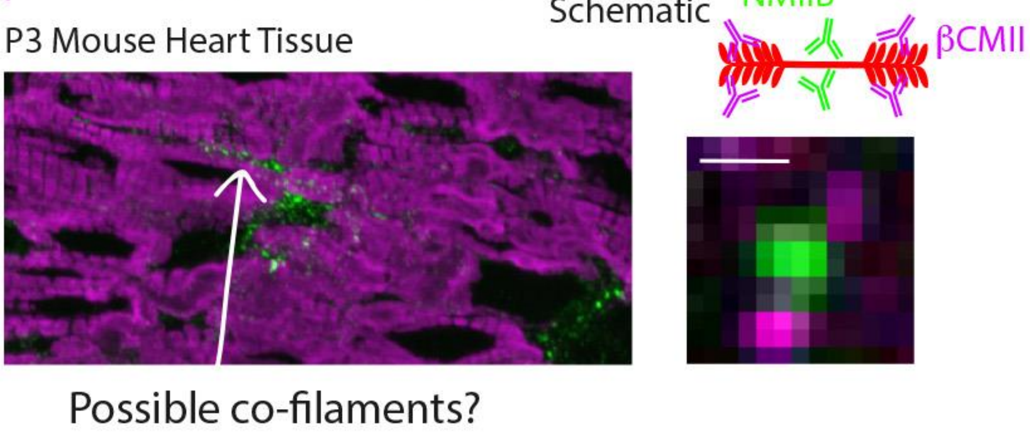

C

Septal muscle from a hypertrophic cardiomyopathy patient

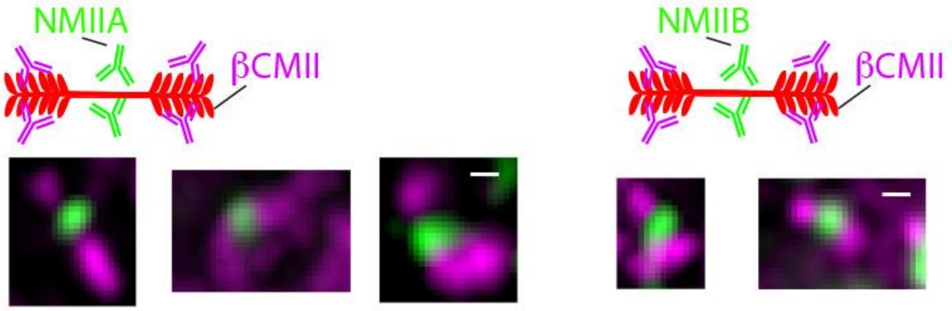

Figure 4-S1: Myosin II co-filaments *in vivo*
(A) hiCM transfected with βCMII-mEGFP (N-terminal motors), stained for endogenous NMIIB rods and imaged with SIM. Schematic depicts visualization strategy. Low mag of hiCM left, and high mag examples bottom right. (B) Low mag view of P3 mouse heart tissue stained for βCMII (motors) and NMIIB (rods), and imaged with laser-scanning confocal. As in hiCMs, NMIIB is restricted from sarcomere structures but is localized adjacently to sarcomeres. Arrow indicates area of possible co-filaments. High mag example shown at right is taken from P3 mouse tissue imaged on Zeiss 880 with AiryScan from similar area indicated by arrow on low mag image. Schematic indicates visualization strategy. (C) High mag examples of NMIIA (left) and NMIIB-βCMII (right) co-filaments from human hypertrophic cardiomyopathy patients imaged on Zeiss 880 with AiryScan. Cartoon schematic indicates imaging strategy. Scale bars: (A, left), 10 μm; (A, right), (B), (C), 200 nm (right).

Figure 4-S2

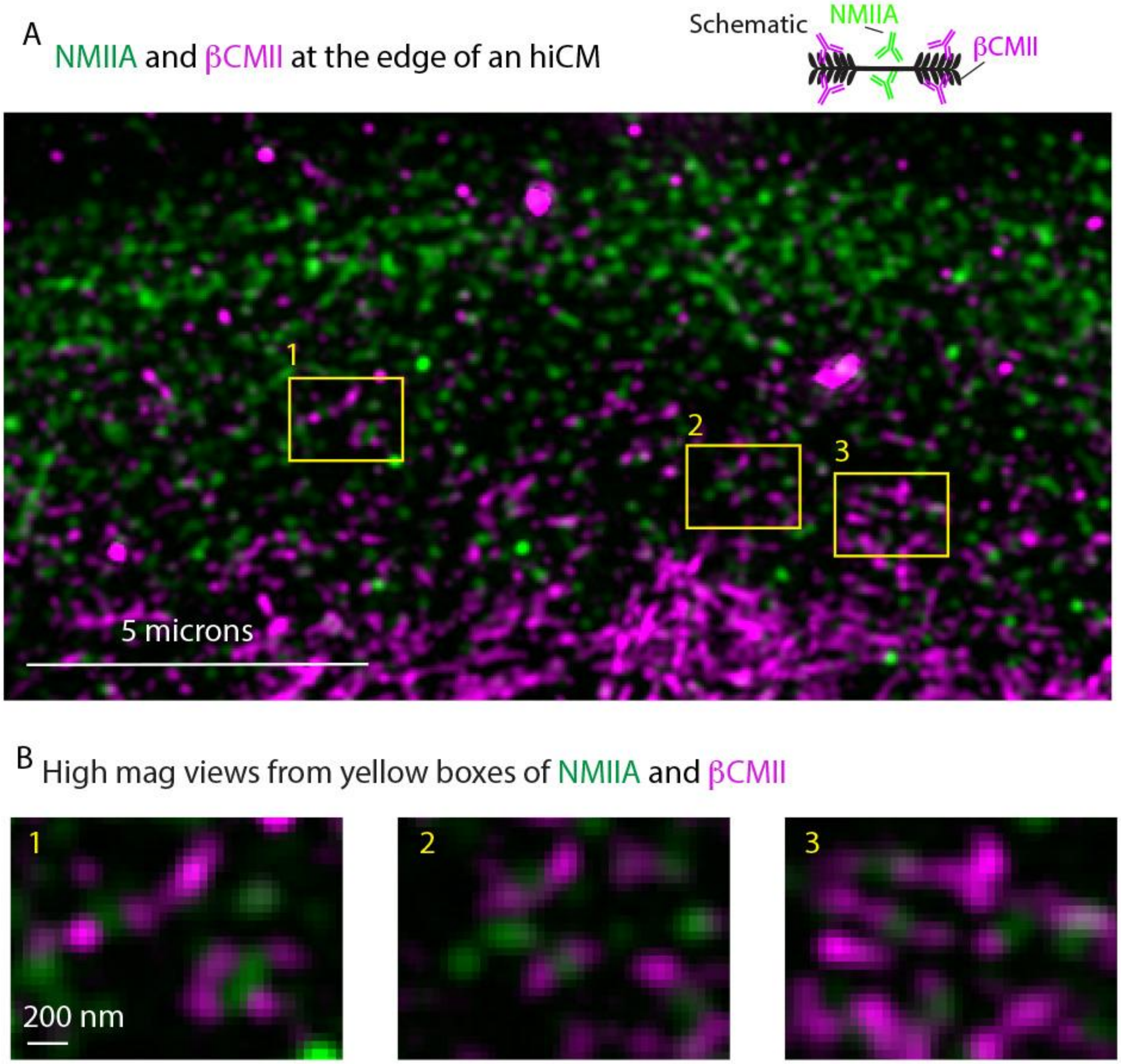

Figure 4-S2: Endogenous localization of NMIIA and βCMII in hiCMs
(A) SIM of endogenous localization of NMIIA (green) and βCMII (magenta) in hiCM. Yellow boxes denote areas of overlap between NMIIA and βCMII. (B) High-mag views of NMIIA-βCMII co-filaments taken from yellow boxes in (A).

Figure 4-S3

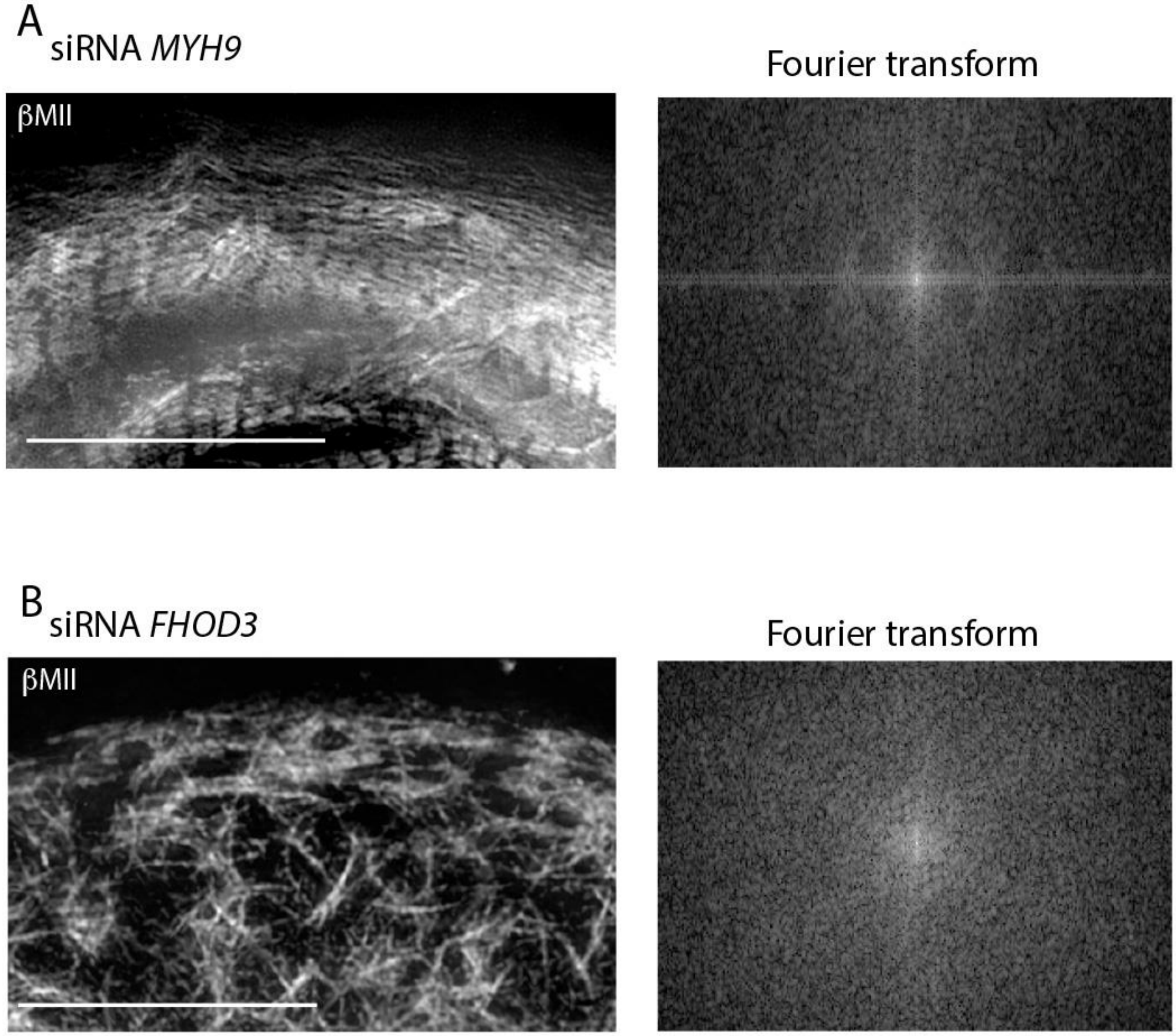

Figure 4-S3: βCMII filament assembly is perturbed in NMIIA and FHOD3 KD hiCMs (A) Endogenous βCMII localized in NMIIA KD (siRNA *MYH9*) hiCMs (left) imaged with SIM. Fourier transform (right) of hiCM shows some periodicity of βCMII which is not as readily apparent compared to scramble control hiCMs (Figure 10G). (B) Endogenous βCMII localized in FHOD3 KD (siRNA *FHOD3*) hiCM (left) imaged with SIM. Note loss of βCMII A-bands. Fourier transforms (right) show loss of sarcomeric periodicity. Scale Bars: 10 μms.

Figure 4-S4

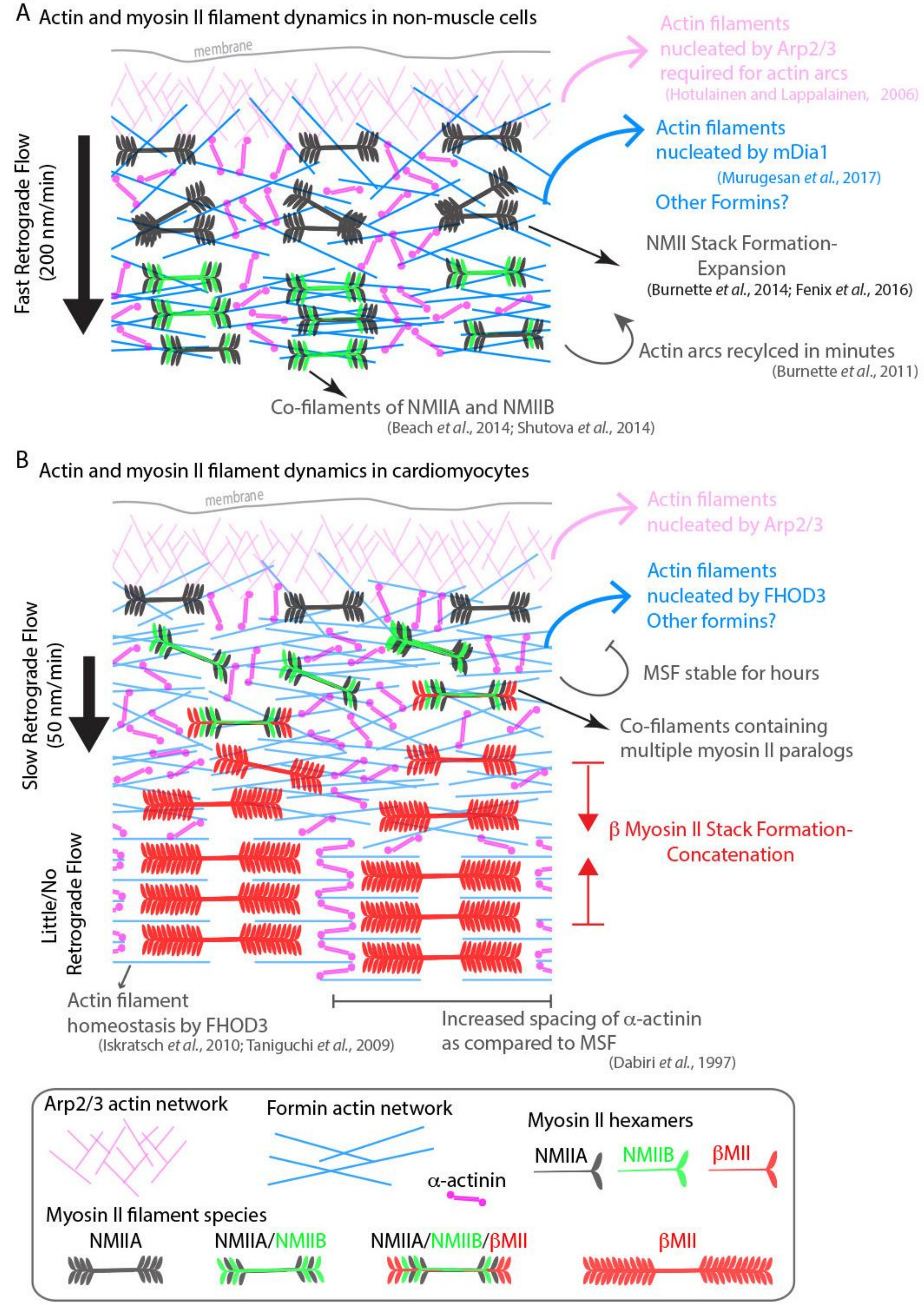
A Actin and myosin II filament dynamics in non-muscle cells
membrane
Fast Retrograde Flow (200 nm/min)
Actin filaments nucleated by Arp2/3 required for actin arcs
(Hotulainen and Lappalainen, 2006)
Actin filaments nucleated by mDia1
(Murugesan et al., 2017)
Other Formins?
NMII Stack Formation-Expansion
(Burnette et al., 2014; Fenix et al., 2016)
Actin arcs recylced in minutes
(Burnette et al., 2011)
Co-filaments of NMIIA and NMIIB
(Beach et al., 2014; Shutova et al., 2014)
B Actin and myosin II filament dynamics in cardiomyocytes
membrane
Slow Retrograde Flow (50 nm/min)
Little/No Retrograde Flow
Actin filaments nucleated by Arp2/3
Actin filaments nucleated by FHOD3
Other formins?
MSF stable for hours
Co-filaments containing multiple myosin II paralogs
β Myosin II Stack Formation-Concatenation
Actin filament homeostasis by FHOD3
(Iskratsch et al., 2010; Taniguchi et al., 2009)
Increased spacing of α-actinin as compared to MSF
(Dabiri et al., 1997)
Arp2/3 actin network
Formin actin network
Myosin II hexamers
NMIIA
NMIIB
βMII
α-actinin
Myosin II filament species
NMIIA
NMIIA/NMIIB
NMIIA/NMIIB/βMII
βMII

Figure 4-S4: Model of actomyosin stress fiber formation in non-muscle cells and human cardiomyocytes

(A) Actin and myosin II stress fiber formation in non-muscle cells. Actin stress fibers are formed via the Arp2/3 complex and the formin mDia1. NMIIA is the predominant isoform at the leading edge of non-muscle cells, and stress fiber formation is NMIIA dependent. Non-muscle cells display robust retrograde flow of actin stress fibers and display rapid turnover. Large NMIIA stacks are formed via growth and expansion of smaller NMIIA filaments. Citations leading to this model are presented in the cartoon. (B) Model of actin and myosin II stress fiber formation in human cardiomyocytes. Sarcomeres are templated by Muscle Stress Fibers (MSFs). MSFs do not require the Arp2/3 complex, and require the formin FHOD3. MSFs display slow retrograde flow compared with non-muscle stress fibers. Both NMIIA and NMIIB are localized to the edge of hiCMs, and display prominent NMII co-filaments. NMIIB-βCMII co-filaments are also present with MSFs. Large βCMII filament stacks form via concatenation and stitching of individual βCMII filaments.

Chapter V

Chapter summaries and future directions

Chapter II summary

In Chapter II, we investigated the mechanisms and dynamics of NMIIA stack formation in non-muscle cells. We used structured illumination microscopy (SIM) to demonstrate a variety of NMIIA filament organizations at the leading edge of crawling cells. Live-cell SIM revealed that smaller NMIIA filaments (i.e., a “2-motor group filament”) expanded into the larger NMIIA stacks via distinct structural steps. NMIIA stack formation could also occur via “concatenation” of distinct NMIIA filaments, though this occurred less often, and was not mutually exclusive from expansion. Through a series of genetic and pharmacological perturbations, we demonstrated NMIIA filament expansion and stack assembly was dependent on NMIIA motor activity and actin filament availability. Interestingly, we also demonstrated that the cleavage furrow of dividing cells was made up of prominent NMIIA stacks which appeared to assemble via similar mechanisms as at the leading edge of crawling cells. We summarized our results in a new model of NMIIA stack assembly we called the Expansion Model of NMIIA Stack Assembly (Fenix and Burnette, 2018; Fenix et al., 2016).

The Expansion Model was in direct contradiction to the major model of NMIIA stack assembly, referred to as the Network Contraction Model (Verkhovsky and Borisy, 1993; Verkhovsky et al., 1999a). This model has been the textbook model of acto-myosin stress fiber assembly for ~20 years. Our work was subsequently reproduced and confirmed in two publications. Though it is possible “network contraction” occurs where myosin II filaments are very dense, our data suggests at the edge of crawling cells and the cleavage furrow of dividing cells, Expansion is the major mechanism. We believe our model of NMIIA stack assembly now provides a framework for future studies to mechanistically parse out the intricate details of NMIIA stack assembly.

Chapter II future directions

Our Expansion Model of NMIIA stack assembly now affords an experimental framework to elucidate the mechanisms regulating NMIIA stack assembly. While we demonstrated that NMIIA motor activity and actin filament availability were important for stack assembly, this is only the tip of the iceberg as far as mechanisms regulating NMIIIA stack assembly are concerned. There are likely inherent modes of regulation (i.e., upon NMIIA itself), and mechanisms acting through the action of actin binding proteins which could affect NMIIA stack assembly.

NMIIA contains numerous phosphorylation sites along both its heavy chain, and light chains (Vicente-Manzanares et al., 2009b). A recent publication demonstrated these phosphorylation sites are critical for the proper localization of NMIIA and NMIIB in crawling cells (Juanes-Garcia et al., 2015). It is highly likely these phosphorylation sites are involved in NMIIA stack formation, and are prime targets for future work. In addition, NMIIA has been shown to form co-filaments with NMIIB and another myosin, myosin 18 (Billington et al., 2015). It is possible that different filament organizations and compositions promote or inhibit stack assembly.

In addition to inherent NMII regulation, actin binding and actin nucleating factors likely affect NMII stack assembly. Indeed, we should inhibiting plus end actin polymerization reduced NMIIA stack assembly (Chapter II). The most obvious candidates are proteins involved in organizing the actin arc stress fibers NMIIA stacks assemble upon. These include the Arp2/3 complex, formins such as dia1/2, tropomyosin IV, and α-actinin 1/4. These proteins have been shown to disrupt actin arc formation and dynamics, but how they affect NMIIA filament assemblies is unknown (Hotulainen and Lappalainen, 2006; Murugesan et al., 2016; Tojkander et al., 2012; Tojkander et al., 2011). Inhibiting or depleting cells of these proteins and investigating both actin architecture and the ability of cells to assemble NMIIA stacks will be fascinating. This is especially important as recent work has suggested increased acto-myosin II based forced generation is critical for cancer metastasis (Derycke et al., 2011; Lopez et al., 2011; Maeda et al., 2008; Paszek et al., 2005; Samuel et al., 2011). An understanding of how cells build the contractile machinery required for metastasis could reveal novel therapeutic targets.

Recent work is revealing the presence of NMII stacks in a variety of cellular contexts (Ebrahim et al., 2013). In these diverse processes, it will be interesting to establish whether Expansion, Network Contraction, or different mechanisms of NMIIA stack assembly is occurring. Future work will determine how well conserved these processes are in different cellular contexts, and with respect to other myosin II paralogs, such as NMIIB. Indeed, this question initially inspired aspects of the work presented in Chapters III and IV.

Chapters III and IV summaries

In Chapter III of this work, we investigated the mechanisms leading to sarcomere assembly in human iPSC-derived cardiac myocytes (hiCMs), with an emphasis on the actin cytoskeleton. To carry out this work, we developed a model system amenable to live-cell imaging and robust quantification of experimental perturbations. Using this system, we described a population of acto-myosin stress fibers in hiCMs we refer to as Muscle Stress Fibers (MSFs). MSFs were structurally similar to actin arcs in non-muscle cells, but displayed significantly slower retrograde flow. Live-cell imaging revealed sarcomeres were directly assembled via a MSF template. This transition from MSF to sarcomeres occurred on the dorsal (top) surface of cell. MSF assembly and subsequent transition to sarcomeres was dependent on formins, and specifically the formin FHOD3. Though the Arp2/3 complex has been shown to be required for actin arc assembly, it was not required for MSF or sarcomere assembly. Both NMIIA and NMIIB were required for sarcomere assembly in hiCMs and Zebrafish, though NMIIB showed the more dramatic phenotype in hiCMs. These results demonstrated sarcomeres are assembled via a template (MSF) structure, and the template – though structurally similar – is regulated differently than actin arcs in non-muscle cells.

In Chapter IV of this work, we investigated the mechanisms leading to β cardiac myosin II (βCMII) filaments stack assembly (i.e., the A-band) in hiCMs. This work was in part inspired and guided by experiments conducted in Chapter II, showing how large, structurally similar NMIIA filament stacks assembled in non-muscle cells. We demonstrated NMIIA and NMIIB localized to MSFs but were restricted from sarcomeres. βCMII localized with a slight overlap to NMIIA and NMIIB but predominately localized behind NMII. βCMII filaments formed co-filaments with NMIIA and NMIIB. βCMII-NMII co-filaments were roughly the size of NMIIA/NMIIB filaments (~250nm). Indeed, βCMII filaments grew progressively larger towards the cell body, suggesting they polymerized at the edge of hiCMs and grew larger over time. Similar to the actin thin filaments, FHOD3, NMIIA, and NMIIB were required for βCMII filament stack assembly, with NMIIB showing the most dramatic effect. Complete removal of the actin cytoskeleton (via Latrunculin B) resulted in a complete loss of βCMII filament stacks, suggesting βCMII filaments require an actin "track". Interestingly, βCMII filament stacks formed almost exclusively via concatenation and "stitching" of distinct βCMII filaments to create a larger ensemble (i.e., the A-band). This is opposed to NMIIA stack assembly which occurs almost exclusively via Expansion of NMIIA filaments (Chapter II).

Collectively, our data led us to propose a new and unifying model of sarcomere assembly. Rather than being mutually exclusive from previous models, our model incorporates aspects from multiple models which our data supports. We believe our unified model of sarcomere assembly, combined with the model system we describe, represents a powerful framework to thoroughly test molecular and dynamic mechanisms of sarcomere assembly and subsequent regulation.

Chapters III and IV future directions

Actin Nucleating and Actin Binding Proteins During Sarcomere Assembly

Much remains to be elucidated in the complex process of sarcomere assembly in hiCMs. One particular area of intrigue concerns actin nucleating factors. FHOD3 was required outright for sarcomere assembly. However, in knockdown experiments of the next two most highly expressed formins in our hiCMs – DAAM1 and DIAPH1 – sarcomeres still formed. However, the DAAM1 and DIAPH1 KD hiCMs displayed MSFs defects and the sarcomeres which formed were disorganized compared to controls. Thus, it is likely formins (of which there are 15 in mammals), have non-redundant roles during sarcomere assembly. Though the Arp2/3 complex did not appear to be important for sarcomere assembly, it is highly expressed in hiCMs, and could have roles we did not observe. For example, the Arp2/3 complex has recently been implicated in chromosome capture during cell division and DNA damage repair (Burdyniuk et al., 2018; Schrank et al., 2018).

In addition to these actin nucleating proteins, there are likely additional actin binding proteins which affect sarcomere assembly. Prime targets include actin bundling/actin organizing proteins such as α-actinin, spectrin, and filamin. As MSFs and sarcomeres have dramatic structural differences, these bundling proteins could be essential for the transition from MSFs to sarcomeres. Other interesting candidates include capping protein and actin severing proteins, which have been shown to be important for regulating thin filament length in assembled sarcomere structures (Gokhin and Fowler, 2013; Kremneva et al., 2014). Furthermore, proteins which regulate actin filament length, potentially control how the spacing of the observed sarcomere structure, both in width from Z-disc to Z-disc, and between actin filaments themselves. Our model system amenable to live-cell experiments will help answer these tantalizing questions.

Non-muscle myosin IIs during sarcomere assembly

Our data showed that NMIIB was required outright for sarcomere assembly, and NMIIA knockdown resulted in fewer and smaller sarcomeres. How these proteins were resulting in sarcomere disruption is still unclear. It is likely both NMIIA and NMIIB are required for both MSF assembly and transition into sarcomeres (MSFs are mostly absent/highly disorganized in NMII knockdown conditions). NMIIA and NMIIB form myosin II co-filaments. One intriguing idea is that NMIIA/NMIIB are serving as bona-fide templates which βCMII filaments are seeded onto and subsequently grow larger. NMIIA and NMIIB are then lost (as our data shows) and exclusive βCMII filaments assemble to form the A-band. This idea needs to be explored in more detail. Alternatively, NMIIA/NMIIB could be creating the proper tension on actin filaments which βCMII "recognizes" and then is loaded on to. *In vitro* experiments have demonstrated load/tension can alter myosin II kinetics and binding (Hundt et al., 2016; Kovacs et al., 2007).

There is also conflicting data surrounding the roles of NMIIA and NMIIB during sarcomere assembly in hiCMs. A paper was recently published using CRISPR/Cas9 NMIIA/NMIIB double knockout hiCMs and proposed NMIIA/NMIIB were not required for sarcomere assembly (Chopra et al., 2018). This data is highly suspect as these hiCMs do not resemble control hiCMs and clearly do not contain sarcomeres. These conflicting data need to be remedied. Furthermore, *in vivo* data regarding the role of NMII during sarcomere assembly is conflicting (see Introduction and Chapter III). A model system which can ensure efficient knockdown of NMIIA and/or NMIIB prior to sarcomere assembly combined with rigorous analysis will be required to answer this question in the *in vivo* context.

Separate or linked mechanisms of thin and thick filament assembly

Certain pieces of our data suggests thin and thick filament assembly are linked. For example, NMIIB KD and Latrunculin B treatment abolished both thin and thick filament assembly. However, on “residual” actin filaments, βCMII filaments were observed to form. Thus it appears that βCMII requires an actin track. However, data not presented in Chapters III and IV would contradict this result. For example, in hiCMs treated with CytochalasinD to prevent actin polymerization, display prominent βCMII filament stacks assembled on actin resembling MSFs, not sarcomeric actin (Figure 5-1). In addition, recent work from Chuck Murry’s lab contradicts (Chopra et al., 2018) and suggests actin thin filaments still form comparable to control cells in βCMII KO hiCMs. This is an intriguing area of research which should be investigated further and has the potential to reveal a wealth of information regarding how cells establish contractile units.

Figure 5-1

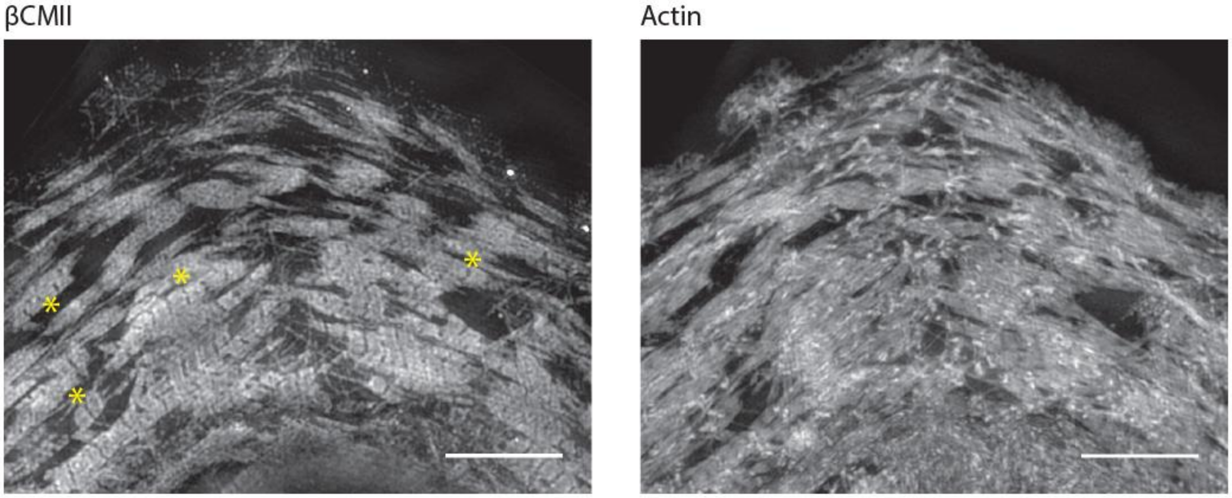

Figure 5-1: hiCMs treated with CytochalasinB display βCMII stacks
hiCM spread for 24 hrs in the presence of 5 μM CytochalasinB display prominent βCMII filament stacks (yellow asterisks). Notably, these βCMII filament stacks localize to actin resembling MSFs not sarcomeric actin.

Myofibril maintenance and turnover

Thus far, our work as solely concerned sarcomere assembly. However, tantalizing pieces of data in the literature suggest sarcomere components turnover at a slow rate (compared to protein turnover in non-muscle cells). How do cells replace the massive proteins of the sarcomere (titin is over 1 mega Dalton, making the relatively large 250kd myosin II seem small) over time? Preliminary data from our lab suggests myofibrils are quite dynamic within the cell, at least at early time points post plating. Longer time-lapse imaging experiments could reveal differing mechanisms between sarcomere assembly and turnover. This is especially relevant during sarcomere “repair”, as it has been shown skeletal muscle can tear and repair itself over the course of a few days (Jarvinen et al., 2013). Indeed, during hypertrophy in multiple cardiac disease states, when cardiomyocytes grow larger, how/do they assemble new myofibrils?

Sarcomere assembly and maintenance with disease causing mutations

Thus far, all our experiments concerning sarcomere assembly were conducted in “wild-type” hiCMs. However, a majority of mutations leading to inherited cardiomyopathies are found within sarcomeric proteins (Konno et al., 2010; Watkins et al., 2011). How do these mutations affect MSFs structure/dynamics and sarcomere assembly? Similar experiments we present in Chapter III should be conducted in the context of relevant mutations leading to cardiomyopathies in humans. This is an intriguing question, as it is currently not understood when the observed post-mortem hallmark of sarcomere disarray is first initiated in patients. A better understanding of sarcomere assembly in disease states could inform therapies aimed at preventing and/or reversing disease states.

Sarcomere assembly in 3-dimensions (3D)

One qualm often directed at studies like those performed in Chapters III and IV is that they are not in a biologically relevant environment. I will spare the reader a historical documentation of this ridiculous reasoning, though even experiments presented in the most recent 2018 Nobel Prize in Physiology or Medicine for targeting immune cells for cancer therapy were conducted in “2D”, but I digress. We must address these criticism as they are, at some level, valid, and will enhance our knowledge of cardiac cell biology. Indeed, *in vivo*, cardiomyocytes are elongated, in a thick layer of cells including cardiomyocytes, fibroblasts, endothelial cells, macrophages, and basement membrane to name a few important factors. Future studies adding increasing layers of complicating have the potential to reveal new mechanisms of sarcomere assembly and the impact of diverse cellular interactions.

MATERIALS AND METHODS

Cell Culture Conditions

Non-muscle cells

U2-OS (ATCC, Manassas, VA, HTB-96,) and HeLa (ATTC, CCL-2) cells were cultured in growth media comprised of DMEM (Mediatech, Inc., Manassas, VA, 10-013-CV) containing 4.5g/L L-glutamine, L-glucose, sodium pyruvate and supplemented with 10% fetal bovine serum (Sigma-Aldrich, St. Louis, MO, F2442). WT HAP1 cells and HAP1 cells with *MYH9* (myosin IIA) knocked out using CRISPR were purchased from Haplogen Genomics (Vienna, Austria). The company confirmed knockout with PCR, and we confirmed using Western blotting (Fig. 3i, S3-3). HAP1 cells were cultured in IMDM (Life Technologies, Grand Island, NY, 12440-053). Cells were kept at 37^o C and 5% CO2. Growth substrates were prepared by coating #1.5 glass coverslips (In Vitro Scientific, D35C4-20-1.5N or D35-20-1.5N) with 25 μg/mL Laminin (Sigma-Aldrich, L2020) in PBS (Mediatech, Inc., 46-013-CM) at 37^o C for 1 hour. Cells were plated on a growth substrate and then experiments were performed the next day. For protein expression experiments, cells were transiently transfected with Fugene 6 (Promega, Madison, WI, E2691) according to the manufacturer's instructions overnight in a 25-cm^2 cell culture flask (Genessee Scientific Corporation, San Diego, CA, 25-207) before plating on a growth substrate.

Human induced pluripotent stem cell derived cardiac myocytes (hiCMs)

hiCMs were purchased from either Axiogenesis (Cor.4u, Ncardia Cologne, Germany) or Cellular Dynamics International (iCell caridomyocytes^2, Madison, WI). Cells were cultured as per manufacturer’s instructions. hiCMs were cultured in 96 well plates and maintained in proprietary manufacturer provided media exchanged every two days until ready for experimental use. Knockdown experiments in hiCMs were started 4 days after the initial thaw.

Live-cell sarcomere assembly visualization assay (chapters III and IV)

To visualize sarcomere formation, we developed a repeatable method, which can be used to visualize any fluorescently tagged protein during sarcomere formation in hiCMs. Prior to performing this assay, cells are maintained in desired culture vessel (our hiCMs were maintained in 96 well plates). In this assay, cells are transiently transfected with desired fluorescently tagged protein, trypsinized, plated on desired imaging dish, and imaged to observe sarcomere formation. A sarcomere assembly assay proceeds as follows. First, hiCMs are transfected with desired fluorescently tagged protein as described below (Viafect, overnight transfection). Transfection mix is washed out with culture media. Cells are then detached from culture vessel using trypsinization method described below. Cells are then plated on a desired culture vessel (in this study, 10mm #1.5 glass bottom dishes were used, CellVis, Mountain View, CA) for live cell imaging. Imaging vessels were pre-coated with 25 µg/mL laminin for 1 hour at 37° C and washed with 1x PBS containing no Mg^{2+}/Ca^{2+}. Cells were allowed to attach for ~1.5 hrs and media was added to fill the glass bottom dish. Cells were then imaged using desired imaging modality at 3-6 hrs post plating. The 3-6 hr time window was optimal, as cells had not yet established sarcomeres, but were healthy enough to tolerate fluorescence imaging. This powerful assay can be adapted to visualize the kinetics during sarcomere formation of any fluorescently tagged protein. We have used this assay to visualize actin (Lifeact), FHOD3, βCMII, α-actinin 2, NMIIA, and NMIIB. The latter two proteins being large (i.e., >250 KD).

Trypsinization of hiCMs (chapters III and IV)

To trypsinize Cellular Dynamics hiCMs, manufacturers recommendations were used, as follows. All volumes apply were modified from 24 well format for 96 well plates. hiCMs were washed 2x with 100uL 1x PBS with no Ca^{2+}/Mg^{2+} (PBS*). PBS* was completely removed from hiCMs and 40uL 0.1% Trypsin-EDTA with no phenol red (Invitrogen) was added to hiCMs and placed at 37° C for 2 minutes. Following incubation, culture dish was washed 3x with trypsin inside well, rotated 180 degrees, and washed another 3x. Trypsinization was then quenched by adding 160 µL of culture media and total cell mixture was placed into a 1.5mL Eppendorf tube. Cells were spun at 1000gs for 5 minutes, and supernatant was aspirated. Cells were then re-suspended in 200uL of culture media and plated on a 10mm glass bottom dish pre-coated with 25 µg/mL laminin for 1 hr. Cells were then allowed to attach for at least 1 hour, and 2-3 mLs of culture media with or without drug was added to cells.

To trypsinize Axiogenesis hiCMs, manufacturers recommendations were used, as follows. Cells were washed 2x with 500µL PBS*. Cells were placed in 37° C incubator for 7 minutes in PBS*. Following 7 minutes, PBS* was aspirated and 40 µL 0.5% Trypsin (Invitrogen) was placed on cells for 3 minutes in 37° C incubator. Following 3 minutes, 160 µL full Cor.4u media was used to quench trypsinization and re-suspend cells. Cells were then plated on pre-coated glass bottom dish and media added 1.5 hrs later to dilute trypsin and fill chamber. Note* this trypsinization protocol has since been modified by Axiogenesis (now Ncardia). See manufacturer for new protocol.

It is important to note that the trypsinization protocol is based off of the hiCMs manufacturers protocols for cell plating, and these hiCMs have been trypsinized prior to functional assays of cardiomyocyte performance and characterization (e.g., drug response, electro-physiology, maturation, etc…) (Fine et al., 2013; Ivashchenko et al., 2013; Mioulane et al., 2012).

Transient transfection of hiCMs (chapters III and IV)

Cellular Dynamics hiCMs were transfected via modification of manufacturer's recommendations as follows. Volumes used are for transfection in 96 well plates. 2 µL of total 200 ng plasmid (containing fluorescently tagged protein of interest, diluted in Opti-MEM) and 2 µL 1:5 diluted Viafect (Promega, E4981, in Opti-MEM) was added to 6 µL Opti-MEM. Entire mixture of 10 µL was added to single 96 well of hiCMs containing freshly exchanged 100 µL full culture media. Transfection was allowed to go overnight (~15 hrs), and washed 2x with full culture media. For transfection of multiple probes, 2 µL of 200ng plasmid was used for each probe together with 4 µL 1:5 diluted Viafect, into 2 µL Opti-MEM and mixture was applied to cells as above.

Axiogenesis hiCMs were transfected via modification of manufacturer's recommendations as follows. A 3.5:1 Fugene to DNA ratio was used to transfect Axiogenesis hiCMs. 1.2 µL Fugene + 0.33 µg DNA per 96 well into 5µL serum free Cor.4u media was incubated for 15 minutes at room temperature. 95 µL full Cor.4u media was added to mixture and entire mixture was added to hiCMs (on top of 100 µL already in well). For transfection of 2 separate plasmids, 3.5:1 ratio was used for both plasmids and additional volume was subtracted from 95 µL dilution. Note* this transfection protocol has since been modified by Axiogenesis. See manufacturer for new protocol.

Protein knockdown (chapters III and IV)

Cellular Dynamics hiCMs were used for knockdown experiments via modification of manufacturers recommendations. Volumes used are for siRNA application in 96 well plates. Dharmacon SmartPool siRNA (GE Dharmacon, Lafayette, CO) targeted to MYH9 (NMIIA), MYH10 (NMIIB), FHOD3, DAAM1, and DIAPH1 were used (E-007668-00-0005, E-023017-00-0010, E-023411-00-0005, E-012925-00-0005, and E-010347-00-0005, respectively). To achieve KD, a master mixture of 100 µl Opti-MEM (ThermoFisher, Waltham, MA) + 4 µl Transkit-TKO (Mirus Bio, Madison WI) + 5.5 µl 10µM siRNA was incubated for 30 min at room temperature. 80 µl of fresh, pre-warmed media was added to hiCMs. Following incubation of siRNA mixture, 8.3 µl of mixture was added to each individual well of 96 well plate. hiCMs were then incubated for 2 days at 37° C. hiCMs were then washed 2x with fresh, pre-warmed media. To achieve KD of NMIIA, NMIIB, FHOD3, DAAM1, and DIAPH1, 3 rounds of siRNA mediated KD described above were necessary. Following 3 rounds of scramble control siRNA treatment, hiCMs still beat and maintained sarcomere structure (see Figure S11).

Western blotting

Gel samples were prepared by mixing cell lysates with LDS sample buffer (Life Technologies, #NP0007) and Sample Reducing Buffer (Life Technologies, #NP00009) and boiled at 95°C for 5 minutes. Samples were resolved on Bolt 4-12% gradient Bis-Tris gels (Life Technologies, #NW04120BOX). Protein bands were blotted onto a nylon membrane (Millipore). Blots were blocked using 5% NFDM (Research Products International Corp, Mt. Prospect, IL, #33368) in TBST. Antibody incubations were also performed in 5% NFDM in TBST. Blots were developed using the Immobilon Chemiluminescence Kit (Millipore, #WBKLS0500).

Fixation and immunohistochemistry

U2-OS cells, HeLa cells, and hiCMs were fixed with 4% paraformaldehyde (PFA) in PBS at room temperature for 20 min and then extracted for 5 min with 1% Triton X-100 and 4% PFA in PBS as previously described (Burnette et al., 2014). Cells were washed three times in 1× PBS. To reduce background for transfected proteins in fixed cells, cells were live-cell extracted before fixation as described previously to reduce background and non-cytoskeletal myosin II filaments (i.e., the soluble pool). Briefly, a cytoskeleton-stabilizing live-cell extraction buffer was made fresh containing 2 ml of stock solution (500 mM 1,4-piperazinediethanesulfonic acid, 25 mM ethylene glycol tetraacetic acid, 25 mM MgCl2), 4 ml of 10% polyoxyethylene glycol (PEG; 35,000 molecular weight), 4 ml H_2O, and 100 µl of Triton X-100, 10 µM paclitaxel, and 10 µM phalloidin. Cells were treated with this extraction buffer for 1 min, followed by a 1-min wash with wash buffer (extraction buffer without PEG or Triton X-100). Cells were then fixed with 4% PFA for 20 min. After fixation, the following labeling procedures were used: for actin visualization, phalloidin-488 in 1× PBS (15 µl of stock phalloidin per 200 µl of PBS) was used for 3 h at room temperature. For immunofluorescence experiments, cells were blocked in 10% bovine serum albumin (BSA) in PBS. Primary antibodies were diluted in 10% BSA. RLC antibody was used at 1:200. NMIIA antibody (BioLegend, P909801) was used at 1:1000. NMIIB antibody (Cell Signaling, 3404S and BioLegend 909901) were used at 1:200. βCMII antibody (Iowa Hybridoma Bank, A4.1025) was used undiluted from serum. α-actinin 2 (Sigma-Aldrich, clone EA-53) antibody was used at 1:200. FHOD3 antibody (Santa Cruz Biotechnology, G-5, sc-374601) was used at 1:100. Arp2/3 antibody (Anti-p34-Arc/ARPC2, Millipore Sigma, 07-227) was used at 1:100. DAAM1 antibody (Bethyl Laboratories, A300-078A) was used at 1:100. DIAPH1 antibody (Sigma-Aldrich, HPA026605) was used at 1:100. Cardiac Troponin T antibody (Santa Cruz Biotechnology, CT3, sc-20025) was used at 200 µg/ml. Secondary antibodies were diluted in 10% BSA at 1:100 and centrifuged at 13,000 rpm for 10 min before use. Cells were imaged in VECTASHIELD Antifade Mounting Media with DAPI (H-1200, VECTOR LABORATORIES, Burlingame, CA, USA). To label both NMIIA and NMIIB in the same sample (as in Figure 7A), NMIIA primary antibody was directly labeled using a primary antibody labeling kit from Biotium (Mix-n-Stain CF Antibody Labeling Kits, Biotium, Inc. Fremont, CA). Following manufacturers protocol, NMIIA was primary labeled, and stain was visually compared to standard immunofluorescence protocol to validate localization pattern.

Pharmacological treatments

Growth media was equilibrated at 37^{o} C and 5% CO_2 for 1 hour before adding drugs. For Blebbistatin, Cytochalasin B, and Y-27632 in Chapter II experiments, drugs were diluted in media and cells were treated for 1 hour at 37^{o} C and 5% CO_2 followed by immediate fixation (see “Fixation and Immunohistochemistry”). For cell division studies, plates were treated with RO-3306 to catch more cells in telophase (Vassilev et al., 2006). RO-3306 was used as described (Vassilev et al., 2006). Briefly, following plating on growth substrate and attachment, cells were incubated with 9 μM RO-3306 for 12 hours and washed out two times with pre-equilibrated media. Cells were fixed 45 minutes after washout. For sarcomere assembly assay (Chapter III), hiCMs were allowed to attach for ~1.5 hours and media containing CK666 or SMIFH2 was added. For live-cell acute drug treatments, equilibrated media containing either CK666 or SMIFH2 was exchanged on the microscope so the same cells could be visualized. For Latrunclin B experiments (Chapter IV), cells were cultured in glass-bottom dishes in incubator and equilibrated media containing Latrunculin B was exchanged and administered for 6 hours before fixation.

Plasmids (chapters II, III, and IV)

Plasmids encoding NMIIA-(N-terminal)-mEGFP (11347; Addgene, Cambridge, MA) with mEGFP on the N-terminus of NMIIA heavy chain were used as described previously (Chua et al., 2009). Plasmid encoding Lifeact-mEmerald and Lifeact-mApple were gifts from Michael Davidson. Plasmid encoding NMIIB-(N-terminal)-mEmerald was purchased from Addgene (54192; Addgene, Cambridge, MA). Plasmid encoding human βCMII was synthesized by Genscript (Piscataway, NJ, USA). Briefly, the wild-type human MYH7 (βCMII) sequence from the National Center for Biotechnology Information (NCBI, Bethesda, MD, USA) was cloned into a pUC57 along with Gateway DNA recombination sequences in order to facilitate rapid fluorescent protein integration and swapping (Gateway Technology, ThermoFisher Scientific, Waltham, MA). mEGFP containing a previously published linker sequence was added to the βCMII plasmid using Gateway Vector Conversion System with One Shot *ccdB* Survival Cells (ThermoFisher Scientific, Waltham, MA) for the βCMII-(N-terminal)-mEGFP construct used in this study. FHOD3-mEGFP plasmid lacking the T(D/E)5XE exon was a gift from Elizabeth Ehler. This construct has previously been shown to localize to sarcomeres in neonatal rat cardiomyocytes (Iskratsch et al., 2010) (see top left panel of Figure 2A in reference). The plasmids encoding mEmerald-MyosinIIA-C-18 (i.e., NMIIA-(N-terminal)-mEmerald)

(Addgene, #54190) or mEos2-MyosinIIA-C-18 (i.e., NMIIA-(N-terminal)-mEOS2) (Addgene #57403) with mEmerald or mEOS2 on the N-terminus of NMIIA heavy chain were used as described previously(Burnette et al., 2014b). Briefly, cDNA (Blue Heron) was ligated into a mEmerald-C1 or mEOS2 cloning vector (Clontech-style). The plasmid encoding mEmerald-C-16-mApple-N-14-MyosinIIA (i.e., NMIIA-(N-terminal)-mEmerald/(C-terminal)-mApple) with mEmerald and mApple on the N and C-termini of NMIIA heavy chain, respectively, was used as described previously(Burnette et al., 2014b). Briefly, mEmerald was PCR amplified and ligated into a mApple-MyosinIIA-N-14. The plasmid encoding NMIIA-N93K-mEGFP (Vicente-Manzanares et al., 2007) was a generous gift from Dr. Alan "Rick" Horwitz.

RNA-seq data analysis (chapter III)

RNA-seq reads were aligned to the human reference genome hg19 using STAR (Dobin et al., 2013) and quantified by featureCounts (Liao et al., 2014). Read counts were normalized by the Relative Log Expression (RLE) method and FPKM values for each sample were generated by DESeq2 (Love et al., 2014).

Zebrafish maintenance and husbandry (chapter III)

Standard procedures were used to raise and maintain zebrafish (Kimmel et al., 1995; Monte Westerfield, 2007). All experiments were conducted using the wild-type AB strain zebrafish in accordance with the University of Wisconsin-Milwaukee Institutional Animal Care and Use Committee.

Antisense morpholino oligonucleotide injections

For zebrafish morpholino knockdown experiments, splice-blocking antisense morpholinos (MO) oligonucleotides were injected into singe-cell wild-type embryos. Morpholino sequences used:

myh10 MO (5’–CTTCACAAATGTGGTCT- TACCTTGA-3’; Gene Tools).

myh9b MO (5’ - AGCAAGAGAGACTTACAAATCGAGA-3’; Gene Tools).

Standard control MO (5’–CCTCTTACCTCAGTTACAATTTATA-3’; Gene Tools).

Zebrafish p53 MO (5’ –GCGCCATTGCTTTGCAA- GAATTG-3’; Gene Tools).

Control experiments have been previously published to confirm morpholino efficacy and specificity including; examination of the morpholino effect on the *myh10* and *myh9b* transcripts using RT-PCR, rescue of the *myh10* and *myh9b* morpholino knockdown phenotype with expression of human *MYH10* or *MYH9* mRNA, and Western blot analysis of morpholino effects on NMIIB protein levels (Gutzman et al., 2015). Additional morpholino controls are presented here to further confirm knockdown protein levels and to evaluate compensatory effects for both *myh10* MO and *myh9b* MO.

3 ng of each morpholino was used for all experiments. p53 MO was used in conjunction with either standard control MO, *myh9b* MO or *myh10* MO. 25 pg of membrane Cherry mRNA was co-injected with each condition to screen for injection efficiency. For heart experiments, embryos were allowed to develop until 48 hours post fertilization (hpf) and then fixed for analysis. For Western analyses, 24 somite stage embryos were dechorionated and deyolked to remove interfering yolk sac proteins (Link et al., 2006). Deyolked, whole embryo tissue was collected in 1X lysis buffer containing 5 mMTris, 400 mM EDTA, 2% Glycerol, and 0.2% Triton X, with cOmplete Protease inhibitor (4693124001, Sigma-Aldrich) and Phosphatase inhibitor (88667, Thermo). 20 mg of

protein was analyzed for each sample. Primary antibodies: NMIIA (ab55456; Abcam) at 1:1000, NMIIB (sc-376942; SCBT) at 1:500, and α-tubulin (T6199; Sigma-Aldrich) at 1:2000. Secondary antibody: anti-mouse HRP (7076; Cell Signaling Technology) at 1:2000. Blots were imaged on a Syngene G-BOX Chemi XRQ imaging system. Blots were quantified using Photoshop (Adobe).

Microscopy methods (chapters II, III, and IV)

Structured illumination microscopy

Two SIM imaging modalities were used in this study (individual experiments were always imaged using the same modality). SIM imaging and processing was performed on a GE Healthcare DeltaVision OMX equipped with a 60×/1.42 NA oil objective and sCMOS camera at room temperature. SIM imaging and processing was also performed on a Nikon N-SIM structured illumination platform equipped with an Andor DU-897 EMCCD camera and a SR Apo TIRF (oil) 100x 1.49 NA WD 0.12 objective at room temperature.

Spinning disk microscopy

Spinning disk confocal images were taken on a Nikon Spinning Disk equipped with a Yokogawa CSU-X1 spinning disk head, Andor DU-897 EMCCD camera and 100x Apo TIRF (oil) 1.49 NA WD 0.12mm objective at 37 degrees C and 5%CO_2.

Laser-scanning confocal microscopy

Laser-scanning confocal images were taken on a Nikon A1R laser scanning equipped with a 60x/1.40 Plan Apo Oil objective at 37 degrees C and 5%CO_2. Confocal images for Figure 6E (*in vivo*, right) and Figure S13C were taken on a Zeiss 880 with AiryScan equipped with a 63x/1.40 Plan-Apochromat Oil objective at room temperature.

Wide-field microscopy

Wide-field images were taken on a high-resolution wide-field Nikon Eclipse Ti equipped with a Nikon 100x Plan Apo 1.45 NA oil objective and a Nikon DS-Qi2 CMOS camera. Figure 5 Chapter II montages were taken on a Leica DMIL cell culture microscope equipped with a N PLAN L 40x/0.55 CORR PH2 at room temperature. Data presented in Figure 7H was acquired on an Incucyte S3 (Ann Arbor, MI) Live-Cell Analysis system with the 20x objective. Photo-conversion experiments were performed as previously described (Fenix et al., 2016).

Live-cell photo-activated localization microscopy (PALM)

Live-cell PALM imaging was performed as previously described(Manley et al., 2008). Total internal reflection microscopy was performed with a Nikon N-STORM microscope using a Nikon 100x Plan Apo 1.49 NA objective and an Andor iXon Ultra EMCCD camera. An image of the unconverted green channel (excited with 488 nm) and converted red channel (excited with 561 nm) was acquired every 5 seconds. Integration times for the green channel varied between 100-150 ms and the red channel integration time was 150 ms. Camera gain was set to 400. We did not use the 405 nm laser as imaging the green channel with the 488 nm laser alone was sufficient to convert enough molecules for analysis as previously described (Sengupta et al., 2011). The precise localization of single converted NMIIA-mEOS2 molecules was determined with the ThunderSTORM ImageJ plugin as previously described (Ovesny et al., 2014). The average localization precision for the NMIIA-mEOS2 molecules analyzed was 24.6 +/- 4.0 nm.

Three-dimensional photo-activated localization microscopy (3D-PALM)

3D-PALM measurements were performed as previously described (Betzig et al., 2006; Brown et al., 2011; Xu et al., 2012). Briefly, U2OS cells expressing NMIIA-mEOS2 were fixed with 4% paraformaldehyde and .25% glutaraldehyde and imaged with a custom-built dual objective (4Pi; Nikon 1.49 NA TIRF objectives; Melville,NY) epifluorescence microscope. Astigmatism was introduced on both objective images using deformable mirrors (Brown et al., 2011) and were collected on separate EM-CCD cameras (Andor iXon Ultra, DU-897; Belfast, UK). Z-coordinate parameters were extracted using the ellipticity of image localizations for multiple gold fiducials embedded in the coverslip (Hestzig, Leesburg, VA). Images from each objective were independently drift corrected in all dimensions and registered with one another using gold fiducials (typically, less than 10-20 nm of residual error persisted after these corrections). Localization pairs were spatially correlated in each image frame and those with less than 0.3 pixel (133.3 nm pixels) deviations were used to recalculate the number of photons collected for each localization. Those localizations which did not display a correlating image from the other objective were discarded (typically 10-20% of the total localizations). All images were rendered using custom Matlab software (Natick, MA) using the positional uncertainty as a probability distribution for each localization dimension (Betzig et al., 2006). Using our imaging approach, discrete clusters of NMIIA-mEOS2 localizations yielded 30-40 nm and 60-90 nm Full-Width at Half-Maximum in the X/Y and Z dimensions, respectively.

Data quantification

ImageJ, Slidebook 6 (Intelligent Imaging Innovations, Denver, CO), and Nikon Elements software were used for data quantification. For 2-3-4 and stack length quantification, regions of interests (ROIs) were used and placed at the leading edge of a migrating cell. For 2-3-4 and filament density quantification, a region of interest extending 1.5 μm from the leading edge was defined (Fig. S3-1), and every discrete myosin II ensemble that could be quantified as a 2, 3, 4, or >4-motor-group in this region was counted. Increasing the distance from the edge of the region of interest further increased the number of overlapping NMIIA-Fs, whose structures could not be defined. For stack length quantification in U2OS cells, a 15x7 μm box (determined empirically as the best size for all cells measured) was placed starting with the first NMIIA-F in the protrusive area of a migrating cell, and all NMIIA-Fs were measured (Fig. S3-2). For stack length quantification in cleavage furrow of HeLa cells, an 8x6 micron box (determined empirically as the best size for all cells measured) was placed in the middle of the cleavage furrow and every NMIIA-F was measured. For actin filament intensities, all cells were imaged with the same laser intensity and exposure, and maximum projections of the cells were analyzed. Three, 1x1 μm boxes were used per cell and averaged to measure intensity. Boxes were placed 2 μm behind cell edge in between the dorsal stress fibers, which do not contain myosin II(Hotulainen and Lappalainen, 2006) and were unchanged by cytochalasin B treatment (Fig. 4). P-values from student T-tests and standard error of the mean (SEM) were calculated using Microsoft Excel.

QUANTIFICATION AND STATISTICAL ANALYSIS (chapters III and IV)

Data quantification

To quantify percent of hiCMs with sarcomeres (i.e., Figure 4B), the actin cytoskeleton (via fluorescently labeled phalloidin) was imaged using structured illumination microscopy.

hiCMs were quantified as containing sarcomere structures if they contained at least 1 myofibril containing at least 3 Z-discs (bright phalloidin staining which overlaps with α-actinin 2 staining as in Figure 4A) spaced ~1.5-2 μm apart. By these metrics our quantification of sarcomere formation is not a measure of sarcomere maturity or alignment, but a measure of the hiCMs ability to assemble the building blocks of the sarcomere (i.e., the thin actin filaments) in response to a perturbation. Thus, while NMIIA KD hiCMs clearly form unaligned, disorganized, and fewer sarcomeres and myofibrils than control hiCMs, they still maintain the ability to assemble sarcomere structures, which is reflected in our quantification (Figures 8A and 8C). In the same vein, we realize our quantification is a very liberal quantification of sarcomere assembly. While we don't expect a small array of sarcomeres to represent a functionally capable cardiomyocyte, we are investigating the early steps of sarcomere assembly and the ability of hiCMs to form the basic actin-myosin structure of the sarcomere. A similar methodology was used to quantify βCMII A-band filament stacks in Figure 10, using endogenous βCMII staining and SIM instead of the actin cytoskeleton. hiCMs were quantified as containing βCMII A-band filament stacks if they contained even one βCMII filament stack, comparable to the smallest βCMII filament stacks found in control hiCMs. A βCMII filament stack is a βCMII filament ensemble which is thicker (i.e., contains more SIM resolve-able βCMII filaments) than a single βCMII filament. Sarcomere formation in Zebrafish experiments is described below.

For actin arc and MSF retrograde flow rates (as in Figure 3), 3 regions of interest (ROIs) were used per cell. ROIs were drawn using the line tool in FIJI starting from in front of the leading edge (to ensure new MSF formation was captured) to the cell body where sarcomere structures were localized. ROIs were then used to measure MSF translocation rates using the kymograph tool (line width = 3) on hiCMs which had been aligned using StackReg function. Kymographs generated in this manner were then manually measured by counting pixels on the X axis (distance) and the Y axis (time) for a distance/time measurement resulting in translocation rates. This method is similar to previously described methods of actin arc translocation in non-muscle cells.

To measure distance between α-actinin 2 structures, the line tool and measure tool in FIJI (Fiji is Just ImageJ) was used. Lines were drawn, positions recorded (using ROI tool), and distances measured between α-actinin 2 structures. Multiple regions per cell for α-actinin 2 in MSFs, and whole cells for distances between sarcomeres were used.

To measure Z-line sizes in hiCMs, the line tool and measure tool in FIJI was used. Lines were drawn on individual Z-lines and their positions were recorded using the ROI tool. This gave a measurement of Z-line size and position within the cell. For Z-line measurements, such as Figure 8E, all Z-lines which could be reliably measured were measured.

Actin staining and sarcomere quantification in zebrafish ventricles

48 hours post fertilization (hpf), embryos were fixed in 4% paraformaldehyde in PBT for 2 hours or overnight at 4°C. Embryos were then washed three times in PBT. To visualize actin, embryos were incubated in Alexa Fluor 488 phalloidin (Invitrogen A12379) at a ratio of 1:40 in PBT at 4°C for 2 days. Next, embryos were washed five times in PBT. For imaging, embryos were manually deyolked and heart tissue dissected. Heart tissue was mounted on a microscope slide in 100% glycerol for imaging. Imaging was conducted using a Nikon CS2 laser-scanning confocal microscope with NIS Elements software.

Maximum projections were created by the last author of each ventricle and each image file was labeled by a random number. The first author then measured each Z line in a blinded fashion using FIJI. The bright actin staining representing Z-discs was used to count all Z-discs present in all conditions. The number of Z-discs per image were divided by the size in microns of that individual animal heart for the Z-disc/μm measurement in Figure 9. Z lines were also measured from “top” to “bottom” of the long axis of every Z line for each condition for sarcomere size measurements. This gave number of Z lines and size (length) of each Z line. For persistence measurements, the number of sarcomeres in every myofibril for each image were counted (thus if a myofibril contained 4 sarcomeres, it had a persistence of 4).

Immunofluorescence localization quantification

To quantify localization of NMIIA, NMIIB, and βCMII, line scans starting from the edge of the cell were taken for every cell and the normalized average localizations were used to average the number of indicated experiments for the final localization patterns depicted in the graph (as in Figure 7B).

To quantify Arp2/3 intensity, a similar but altered strategy was taken. 4 separate boxes for each cell were placed along the edge of the cell (i.e., the lamellipodium) using the actin channel for guidance. These boxes were then used to measure average intensity of the anti-p34 channel (i.e., the Arp2/3 complex). Background subtracted averages for each cell in control and CK666 treated hiCMs were used to quantify percent decrease as depicted in Figure 4F.

Statistics

Statistical significance was calculated using 2-tailed, unpaired Students T-tests performed in Excel. All independent experiments represent biological replicates. Error bars in all graphs represent standard error of the mean (SEM). For all graphs depicting % of cells (for example, Figure 1D), number of cells and experiments is indicated in figure legend. Percents displayed represent the average of the averages of the all experiments performed. For example, if controls cells displayed 95%, 90%, and 100% of all cells displaying actin arcs in 3 separate experiments, the represented percentage in the graph would be 95%. SEM was calculated by dividing the standard deviation by the square root of the number of separate experiments. For actin translocation rates at least 3 measurements per cell were used to calculate the average translocation rates per cell. Translocation rates were then calculated in same manner as described above. Line-scan graphs represent normalized relative fluorescence.

Selection of cells used for chapter II

Polarized migrating U2-OS cells were chosen for this study by finding cells that had a curved leading edge and characteristic protrusive elements (i.e., lamellipodium), as described previously (Burnette et al., 2014b). HeLa cells in telophase were chosen based on chromosome position/morphology and having an ingressed furrow but not a midbody.

Selection of cells used for chapter III and IV

In order to have comparable results, cells used for this study were standardized based on morphology. Specifically, spread non-muscle cells and hiCMs with a broad leading edge and lamella were chosen as previously shown in studies of both non-muscle and muscle contractile system formation (Burnette et al., 2014a; Rhee et al., 1994). This also facilitated the ability to observe the MSF to sarcomere transition in live hiCMs, and is recommended for future studies investigating sarcomere assembly. All experiments measuring sarcomere assembly were conducted at least 3 times, separately, and cells were imaged using SIM. Though this results in a relatively small number of cells for some of the experiments, we believe super-resolution imaging modalities such as SIM offer invaluable insight into sarcomere assembly (Gustafsson, 2005). Indeed, sub-diffraction imaging is required to reliably localize myosin II co-filaments both *in vitro* and *in vivo*. Furthermore, as has been seen in *Drosophila*, even high-resolution imaging modalities such as laser-scanning confocal microscopy are not sufficient to detect subtle, yet important, structural changes in response to perturbation (Fernandes and Schock, 2014).

REFERENCES

Adelstein, R.S., T.D. Pollard, and W.M. Kuehl. 1971. Isolation and characterization of myosin and two myosin fragments from human blood platelets. *Proceedings of the National Academy of Sciences of the United States of America*. 68:2703-2707.

Almenar-Queralt, A., C.C. Gregorio, and V.M. Fowler. 1999. Tropomodulin assembles early in myofibrillogenesis in chick skeletal muscle: evidence that thin filaments rearrange to form striated myofibrils. *Journal of cell science*. 112 (Pt 8):1111-1123.

Au, Y. 2004. The muscle ultrastructure: a structural perspective of the sarcomere. *Cellular and molecular life sciences : CMLS*. 61:3016-3033.

Babbin, B.A., S. Koch, M. Bachar, M.A. Conti, C.A. Parkos, R.S. Adelstein, A. Nusrat, and A.I. Ivanov. 2009. Non-muscle myosin IIA differentially regulates intestinal epithelial cell restitution and matrix invasion. *Am J Pathol*. 174:436-448.

Beach, J.R., G.S. Hussey, T.E. Miller, A. Chaudhury, P. Patel, J. Monslow, Q. Zheng, R.A. Keri, O. Reizes, A.R. Bresnick, P.H. Howe, and T.T. Egelhoff. 2011. Myosin II isoform switching mediates invasiveness after TGF-beta-induced epithelial-mesenchymal transition. *Proceedings of the National Academy of Sciences of the United States of America*. 108:17991-17996.

Beach, J.R., L. Shao, K. Remmert, D. Li, E. Betzig, and J.A. Hammer, 3rd. 2014. Nonmuscle myosin II isoforms coassemble in living cells. *Current biology : CB*. 24:1160-1166.

Betzig, E., G.H. Patterson, R. Sougrat, O.W. Lindwasser, S. Olenych, J.S. Bonifacino, M.W. Davidson, J. Lippincott-Schwartz, and H.F. Hess. 2006. Imaging intracellular fluorescent proteins at nanometer resolution. *Science*. 313:1642-1645.

Billington, N., J.R. Beach, S.M. Heissler, K. Remmert, S. Guzik-Lendrum, A. Nagy, Y. Takagi, L. Shao, D. Li, Y. Yang, Y. Zhang, M. Barzik, E. Betzig, J.A. Hammer, 3rd, and J.R. Sellers. 2015. Myosin 18A coassembles with nonmuscle myosin 2 to form mixed bipolar filaments. *Current biology : CB*. 25:942-948.

Billington, N., A. Wang, J. Mao, R.S. Adelstein, and J.R. Sellers. 2013. Characterization of three full-length human nonmuscle myosin II paralogs. *The Journal of biological chemistry*. 288:33398-33410.

Breckenridge, M.T., N.G. Dulyaninova, and T.T. Egelhoff. 2009. Multiple regulatory steps control mammalian nonmuscle myosin II assembly in live cells. *Molecular biology of the cell*. 20:338-347.

Breitsprecher, D., and B.L. Goode. 2013. Formins at a glance. *Journal of cell science*. 126:1-7.

Brown, T.A., A.N. Tkachuk, G. Shtengel, B.G. Kopek, D.F. Bogenhagen, H.F. Hess, and D.A. Clayton. 2011. Superresolution fluorescence imaging of mitochondrial nucleoids reveals their spatial range, limits, and membrane interaction. *Molecular and cellular biology*. 31:4994-5010.

Bryce, N.S., G. Schevzov, V. Ferguson, J.M. Percival, J.J. Lin, F. Matsumura, J.R. Bamburg, P.L. Jeffrey, E.C. Hardeman, P. Gunning, and R.P. Weinberger. 2003.

Specification of actin filament function and molecular composition by tropomyosin isoforms. *Mol Biol Cell*. 14:1002-1016.

Burdyniuk, M., A. Callegari, M. Mori, F. Nedelec, and P. Lenart. 2018. F-Actin nucleated on chromosomes coordinates their capture by microtubules in oocyte meiosis. *J Cell Biol*. 217:2661-2674.

Burnette, D.T., S. Manley, P. Sengupta, R. Sougrat, M.W. Davidson, B. Kachar, and J. Lippincott-Schwartz. 2011. A role for actin arcs in the leading-edge advance of migrating cells. *Nature cell biology*. 13:371-381.

Burnette, D.T., A.W. Schaefer, L. Ji, G. Danuser, and P. Forscher. 2007. Filopodial actin bundles are not necessary for microtubule advance into the peripheral domain of Aplysia neuronal growth cones. *Nat Cell Biol*. 9:1360-1369.

Burnette, D.T., L. Shao, C. Ott, A.M. Pasapera, R.S. Fischer, M.A. Baird, C. Der Loughian, H. Delanoe-Ayari, M.J. Paszek, M.W. Davidson, E. Betzig, and J. Lippincott-Schwartz. 2014a. A contractile and counterbalancing adhesion system controls the 3D shape of crawling cells. *J Cell Biol*. 205:83-96.

Burnette, D.T., L. Shao, C. Ott, A.M. Pasapera, R.S. Fischer, M.A. Baird, C. Der Loughian, H. Delanoe-Ayari, M.J. Paszek, M.W. Davidson, E. Betzig, and J. Lippincott-Schwartz. 2014b. A contractile and counterbalancing adhesion system controls the 3D shape of crawling cells. *The Journal of cell biology*.

Chen, B.C., W.R. Legant, K. Wang, L. Shao, D.E. Milkie, M.W. Davidson, C. Janetopoulos, X.S. Wu, J.A. Hammer, 3rd, Z. Liu, B.P. English, Y. Mimori-Kiyosue, D.P. Romero, A.T. Ritter, J. Lippincott-Schwartz, L. Fritz-Laylin, R.D. Mullins, D.M. Mitchell, J.N. Bembenek, A.C. Reymann, R. Bohme, S.W. Grill, J.T. Wang, G. Seydoux, U.S. Tulu, D.P. Kiehart, and E. Betzig. 2014. Lattice light-sheet microscopy: imaging molecules to embryos at high spatiotemporal resolution. *Science*. 346:1257998.

Chopra, A., M.L. Kutys, K. Zhang, W.J. Polacheck, C.C. Sheng, R.J. Luu, J. Eyckmans, J.T. Hinson, J.G. Seidman, C.E. Seidman, and C.S. Chen. 2018. Force Generation via beta-Cardiac Myosin, Titin, and alpha-Actinin Drives Cardiac Sarcomere Assembly from Cell-Matrix Adhesions. *Dev Cell*. 44:87-96 e85.

Chua, J., R. Rikhy, and J. Lippincott-Schwartz. 2009. Dynamin 2 orchestrates the global actomyosin cytoskeleton for epithelial maintenance and apical constriction. *Proceedings of the National Academy of Sciences of the United States of America*. 106:20770-20775.

Colpan, M., N.A. Moroz, and A.S. Kostyukova. 2013. Tropomodulins and tropomyosins: working as a team. *Journal of muscle research and cell motility*. 34:247-260.

Conti, M.A., S. Even-Ram, C. Liu, K.M. Yamada, and R.S. Adelstein. 2004. Defects in cell adhesion and the visceral endoderm following ablation of nonmuscle myosin heavy chain II-A in mice. *The Journal of biological chemistry*. 279:41263-41266.

Conti, M.A., A.D. Saleh, L.R. Brinster, H. Cheng, Z. Chen, S. Cornelius, C. Liu, X. Ma, C. Van Waes, and R.S. Adelstein. 2015. Conditional deletion of nonmuscle myosin II-A in mouse tongue epithelium results in squamous cell carcinoma. *Sci Rep*. 5:14068.

Costa, M., M. Fava, M. Seri, R. Cusano, M. Sancandi, P. Forabosco, M. Lerone, G. Martucciello, G. Romeo, and I. Ceccherini. 2000. Evaluation of the HOX11L1 gene as a candidate for congenital disorders of intestinal innervation. *J Med Genet*. 37:E9.

Cote, G.P. 1983. Structural and functional properties of the non-muscle tropomyosins. *Mol Cell Biochem*. 57:127-146.

Craig, R., R. Smith, and J. Kendrick-Jones. 1983. Light-chain phosphorylation controls the conformation of vertebrate non-muscle and smooth muscle myosin molecules. *Nature*. 302:436-439.

Dabiri, G.A., K.K. Turnacioglu, J.M. Sanger, and J.W. Sanger. 1997. Myofibrillogenesis visualized in living embryonic cardiomyocytes. *Proceedings of the National Academy of Sciences of the United States of America*. 94:9493-9498.

De Pascalis, C., and S. Etienne-Manneville. 2017. Single and collective cell migration: the mechanics of adhesions. *Mol Biol Cell*. 28:1833-1846.

Derycke, L., C. Stove, A.S. Vercoutter-Edouart, O. De Wever, L. Dolle, N. Colpaert, H. Depypere, J.C. Michalski, and M. Bracke. 2011. The role of non-muscle myosin IIA in aggregation and invasion of human MCF-7 breast cancer cells. *Int J Dev Biol*. 55:835-840.

Dlugosz, A.A., P.B. Antin, V.T. Nachmias, and H. Holtzer. 1984. The relationship between stress fiber-like structures and nascent myofibrils in cultured cardiac myocytes. *J Cell Biol*. 99:2268-2278.

Dobin, A., C.A. Davis, F. Schlesinger, J. Drenkow, C. Zaleski, S. Jha, P. Batut, M. Chaisson, and T.R. Gingeras. 2013. STAR: ultrafast universal RNA-seq aligner. *Bioinformatics*. 29:15-21.

Dominguez, R., and K.C. Holmes. 2011. Actin structure and function. *Annu Rev Biophys*. 40:169-186.

Du, A., J.M. Sanger, and J.W. Sanger. 2008. Cardiac myofibrillogenesis inside intact embryonic hearts. *Developmental biology*. 318:236-246.

Ebrahim, S., T. Fujita, B.A. Millis, E. Kozin, X. Ma, S. Kawamoto, M.A. Baird, M. Davidson, S. Yonemura, Y. Hisa, M.A. Conti, R.S. Adelstein, H. Sakaguchi, and B. Kachar. 2013. NMII forms a contractile transcellular sarcomeric network to regulate apical cell junctions and tissue geometry. *Current biology : CB*. 23:731-736.

Eddinger, T.J., and D.P. Meer. 2007. Myosin II isoforms in smooth muscle: heterogeneity and function. *American journal of physiology. Cell physiology*. 293:C493-508.

Eggert, U.S., T.J. Mitchison, and C.M. Field. 2006. Animal cytokinesis: from parts list to mechanisms. *Annual review of biochemistry*. 75:543-566.

Ehler, E., B.M. Rothen, S.P. Hammerle, M. Komiyama, and J.C. Perriard. 1999. Myofibrillogenesis in the developing chicken heart: assembly of Z-disk, M-line and the thick filaments. *Journal of cell science*. 112 (Pt 10):1529-1539.

Even-Ram, S., A.D. Doyle, M.A. Conti, K. Matsumoto, R.S. Adelstein, and K.M. Yamada. 2007. Myosin IIA regulates cell motility and actomyosin-microtubule crosstalk. *Nature cell biology*. 9:299-309.

Fenix, A.M., and D.T. Burnette. 2018. Assembly of Myosin II Filament Arrays: Network Contraction vs. Expansion. *Cytoskeleton (Hoboken)*.

Fenix, A.M., N. Taneja, C.A. Buttler, J. Lewis, S.B. Van Engelenburg, R. Ohi, and D.T. Burnette. 2016. Expansion and concatenation of non-muscle myosin IIA filaments drive cellular contractile system formation during interphase and mitosis. *Mol Biol Cell*.

Fernandes, I., and F. Schock. 2014. The nebulin repeat protein Lasp regulates I-band architecture and filament spacing in myofibrils. *J Cell Biol*. 206:559-572.

Fine, M., F.M. Lu, M.J. Lin, O. Moe, H.R. Wang, and D.W. Hilgemann. 2013. Human-induced pluripotent stem cell-derived cardiomyocytes for studies of cardiac ion transporters. *American journal of physiology. Cell physiology*. 305:C481-491.

Forscher, P., and S.J. Smith. 1988. Actions of cytochalasins on the organization of actin filaments and microtubules in a neuronal growth cone. *J Cell Biol*. 107:1505-1516.

Gao, L., L. Shao, C.D. Higgins, J.S. Poulton, M. Peifer, M.W. Davidson, X. Wu, B. Goldstein, and E. Betzig. 2012. Noninvasive imaging beyond the diffraction limit of 3D dynamics in thickly fluorescent specimens. *Cell*. 151:1370-1385.

Gardel, M.L., I.C. Schneider, Y. Aratyn-Schaus, and C.M. Waterman. 2010. Mechanical integration of actin and adhesion dynamics in cell migration. *Annu Rev Cell Dev Biol*. 26:315-333.

Gokhin, D.S., and V.M. Fowler. 2013. A two-segment model for thin filament architecture in skeletal muscle. *Nature reviews. Molecular cell biology*. 14:113-119.

Gunning, P.W., E.C. Hardeman, P. Lappalainen, and D.P. Mulvihill. 2015. Tropomyosin - master regulator of actin filament function in the cytoskeleton. *Journal of cell science*. 128:2965-2974.

Gupton, S.L., and C.M. Waterman-Storer. 2006. Spatiotemporal feedback between actomyosin and focal-adhesion systems optimizes rapid cell migration. *Cell*. 125:1361-1374.

Gustafsson, M.G. 2005. Nonlinear structured-illumination microscopy: wide-field fluorescence imaging with theoretically unlimited resolution. *Proceedings of the National Academy of Sciences of the United States of America*. 102:13081-13086.

Gustafsson, M.G., L. Shao, P.M. Carlton, C.J. Wang, I.N. Golubovskaya, W.Z. Cande, D.A. Agard, and J.W. Sedat. 2008. Three-dimensional resolution doubling in wide-field fluorescence microscopy by structured illumination. *Biophys J*. 94:4957-4970.

Gutzman, J.H., S.U. Sahu, and C. Kwas. 2015. Non-muscle myosin IIA and IIB differentially regulate cell shape changes during zebrafish brain morphogenesis. *Developmental biology*. 397:103-115.

Hamdan, F.F., M. Srour, J.M. Capo-Chichi, H. Daoud, C. Nassif, L. Patry, C. Massicotte, A. Ambalavanan, D. Spiegelman, O. Diallo, E. Henrion, A. Dionne-Laporte, A. Fougerat, A.V. Pshezhetsky, S. Venkateswaran, G.A. Rouleau, and J.L. Michaud. 2014. De novo mutations in moderate or severe intellectual disability. *PLoS genetics*. 10:e1004772.

Hartman, M.A., and J.A. Spudich. 2012. The myosin superfamily at a glance. *Journal of cell science*. 125:1627-1632.

Harunaga, J.S., and K.M. Yamada. 2011. Cell-matrix adhesions in 3D. *Matrix Biol*. 30:363-368.

Harvey, P.A., and L.A. Leinwand. 2011. The cell biology of disease: cellular mechanisms of cardiomyopathy. *The Journal of cell biology*. 194:355-365.

Heath, J.P. 1983. Behaviour and structure of the leading lamella in moving fibroblasts. I. Occurrence and centripetal movement of arc-shaped microfilament bundles beneath the dorsal cell surface. *Journal of cell science*. 60:331-354.

Henson, J.H., M. Yeterian, R.M. Weeks, A.E. Medrano, B.L. Brown, H.L. Geist, M.D. Pais, R. Oldenbourg, and C.B. Shuster. 2015. Arp2/3 complex inhibition radically alters lamellipodial actin architecture, suspended cell shape, and the cell spreading process. *Mol Biol Cell*. 26:887-900.

Hill, J.A.O., E.N. 2012. Muscle Fundamental Biology and Mechanisms of Disease. ELSEVIER.

Ho, C.Y. 2010. Hypertrophic cardiomyopathy. *Heart failure clinics*. 6:141-159.

Holtzer, H., T. Hijikata, Z.X. Lin, Z.Q. Zhang, S. Holtzer, F. Protasi, C. Franzini-Armstrong, and H.L. Sweeney. 1997. Independent assembly of 1.6 microns long bipolar MHC filaments and I-Z-I bodies. *Cell Struct Funct*. 22:83-93.

Hotulainen, P., and P. Lappalainen. 2006. Stress fibers are generated by two distinct actin assembly mechanisms in motile cells. *J Cell Biol*. 173:383-394.

Hu, A., F. Wang, and J.R. Sellers. 2002. Mutations in human nonmuscle myosin IIA found in patients with May-Hegglin anomaly and Fechtner syndrome result in impaired enzymatic function. *The Journal of biological chemistry*. 277:46512-46517.

Hughes, S.E. 2004. The pathology of hypertrophic cardiomyopathy. *Histopathology*. 44:412-427.

Hughes, S.E., and W.J. McKenna. 2005. New insights into the pathology of inherited cardiomyopathy. *Heart*. 91:257-264.

Hundt, N., W. Steffen, S. Pathan-Chhatbar, M.H. Taft, and D.J. Manstein. 2016. Load-dependent modulation of non-muscle myosin-2A function by tropomyosin 4.2. *Sci Rep*. 6:20554.

Hussein, B.A., K. Gomez, and R.A. Kadir. 2013. May-Hegglin anomaly and pregnancy: a systematic review. *Blood Coagul Fibrinolysis*. 24:554-561.

Huxley, A.F., and R. Niedergerke. 1954a. Measurement of muscle striations in stretch and contraction. *J Physiol*. 124:46-47P.

Huxley, A.F., and R. Niedergerke. 1954b. Structural changes in muscle during contraction; interference microscopy of living muscle fibres. *Nature*. 173:971-973.

Huxley, H.E. 1969. The mechanism of muscular contraction. *Science*. 164:1356-1365.

Iskratsch, T., S. Lange, J. Dwyer, A.L. Kho, C. dos Remedios, and E. Ehler. 2010. Formin follows function: a muscle-specific isoform of FHOD3 is regulated by CK2 phosphorylation and promotes myofibril maintenance. *J Cell Biol*. 191:1159-1172.

Ivashchenko, C.Y., G.C. Pipes, I.M. Lozinskaya, Z. Lin, X. Xiaoping, S. Needle, E.T. Grygielko, E. Hu, J.R. Toomey, J.J. Lepore, and R.N. Willette. 2013. Human-induced pluripotent stem cell-derived cardiomyocytes exhibit temporal changes in phenotype. *American journal of physiology. Heart and circulatory physiology*. 305:H913-922.

Jarvinen, T.A., M. Jarvinen, and H. Kalimo. 2013. Regeneration of injured skeletal muscle after the injury. *Muscles Ligaments Tendons J*. 3:337-345.

Juanes-Garcia, A., J.R. Chapman, R. Aguilar-Cuenca, C. Delgado-Arevalo, J. Hodges, L.A. Whitmore, J. Shabanowitz, D.F. Hunt, A.R. Horwitz, and M. Vicente-Manzanares. 2015. A regulatory motif in nonmuscle myosin II-B regulates its role in migratory front-back polarity. *J Cell Biol*. 209:23-32.

Kamasaki, T., M. Osumi, and I. Mabuchi. 2007. Three-dimensional arrangement of F-actin in the contractile ring of fission yeast. *The Journal of cell biology*. 178:765-771.

Kan, O.M., R. Takeya, T. Abe, N. Kitajima, M. Nishida, R. Tominaga, H. Kurose, and H. Sumimoto. 2012. Mammalian formin Fhod3 plays an essential role in cardiogenesis by organizing myofibrillogenesis. *Biol Open*. 1:889-896.

Kelley, M.J., W. Jawien, T.L. Ortel, and J.F. Korczak. 2000. Mutation of MYH9, encoding non-muscle myosin heavy chain A, in May-Hegglin anomaly. *Nature genetics*. 26:106-108.

Kimmel, C.B., W.W. Ballard, S.R. Kimmel, B. Ullmann, and T.F. Schilling. 1995. Stages of embryonic development of the zebrafish. *Dev Dyn*. 203:253-310.

Kolega, J. 1998. Cytoplasmic dynamics of myosin IIA and IIB: spatial 'sorting' of isoforms in locomoting cells. *Journal of cell science*. 111 (Pt 15):2085-2095.

Konno, T., S. Chang, J.G. Seidman, and C.E. Seidman. 2010. Genetics of hypertrophic cardiomyopathy. *Current opinion in cardiology*. 25:205-209.

Kovacs, M., K. Thirumurugan, P.J. Knight, and J.R. Sellers. 2007. Load-dependent mechanism of nonmuscle myosin 2. *Proceedings of the National Academy of Sciences of the United States of America*. 104:9994-9999.

Krause, M., and A. Gautreau. 2014. Steering cell migration: lamellipodium dynamics and the regulation of directional persistence. *Nature reviews. Molecular cell biology*. 15:577-590.

Kremneva, E., M.H. Makkonen, A. Skwarek-Maruszewska, G. Gateva, A. Michelot, R. Dominguez, and P. Lappalainen. 2014. Cofilin-2 controls actin filament length in muscle sarcomeres. *Dev Cell*. 31:215-226.

Kuhne, W. 1864. Untersuchungen uber das Protoplasma und die Contractilitat. *W. Engelmann, Leipzig*.

Kuragano, M., T.Q.P. Uyeda, K. Kamijo, Y. Murakami, and M. Takahashi. 2018. Different contributions of nonmuscle myosin IIA and IIB to the organization of stress fiber subtypes in fibroblasts. *Mol Biol Cell*. 29:911-922.

Liao, Y., G.K. Smyth, and W. Shi. 2014. featureCounts: an efficient general purpose program for assigning sequence reads to genomic features. *Bioinformatics*. 30:923-930.

Lim, S.S., G.E. Hering, and G.G. Borisy. 1986. Widespread occurrence of anti-troponin T crossreactive components in non-muscle cells. *Journal of cell science*. 85:1-19.

Lin, Z., M.H. Lu, T. Schultheiss, J. Choi, S. Holtzer, C. DiLullo, D.A. Fischman, and H. Holtzer. 1994. Sequential appearance of muscle-specific proteins in myoblasts as a function of time after cell division: evidence for a conserved myoblast differentiation program in skeletal muscle. *Cell motility and the cytoskeleton*. 29:1-19.

Link, V., A. Shevchenko, and C.P. Heisenberg. 2006. Proteomics of early zebrafish embryos. *BMC Dev Biol*. 6:1.

Liu, T.L., S. Upadhyayula, D.E. Milkie, V. Singh, K. Wang, I.A. Swinburne, K.R. Mosaliganti, Z.M. Collins, T.W. Hiscock, J. Shea, A.Q. Kohrman, T.N. Medwig, D. Dambournet, R. Forster, B. Cunniff, Y. Ruan, H. Yashiro, S. Scholpp, E.M. Meyerowitz, D. Hockemeyer, D.G. Drubin, B.L. Martin, D.Q. Matus, M. Koyama, S.G. Megason, T. Kirchhausen, and E. Betzig. 2018. Observing the cell in its native state: Imaging subcellular dynamics in multicellular organisms. *Science*. 360.

Lopez, J.I., I. Kang, W.K. You, D.M. McDonald, and V.M. Weaver. 2011. In situ force mapping of mammary gland transformation. *Integr Biol (Camb)*. 3:910-921.

Love, M.I., W. Huber, and S. Anders. 2014. Moderated estimation of fold change and dispersion for RNA-seq data with DESeq2. *Genome Biol*. 15:550.

Lu, M.H., C. DiLullo, T. Schultheiss, S. Holtzer, J.M. Murray, J. Choi, D.A. Fischman, and H. Holtzer. 1992. The vinculin/sarcomeric-alpha-actinin/alpha-actin nexus in cultured cardiac myocytes. *J Cell Biol*. 117:1007-1022.

Luther, P.K. 2009. The vertebrate muscle Z-disc: sarcomere anchor for structure and signalling. *Journal of muscle research and cell motility*. 30:171-185.

Ma, X., and R.S. Adelstein. 2014a. A point mutation in Myh10 causes major defects in heart development and body wall closure. *Circulation. Cardiovascular genetics*. 7:257-265.

Ma, X., and R.S. Adelstein. 2014b. The role of vertebrate nonmuscle Myosin II in development and human disease. *Bioarchitecture*. 4:88-102.

Ma, X., M. Kovacs, M.A. Conti, A. Wang, Y. Zhang, J.R. Sellers, and R.S. Adelstein. 2012. Nonmuscle myosin II exerts tension but does not translocate actin in vertebrate cytokinesis. *Proceedings of the National Academy of Sciences of the United States of America*. 109:4509-4514.

Ma, X., K. Takeda, A. Singh, Z.X. Yu, P. Zerfas, A. Blount, C. Liu, J.A. Towbin, M.D. Schneider, R.S. Adelstein, and Q. Wei. 2009. Conditional ablation of nonmuscle myosin II-B delineates heart defects in adult mice. *Circulation research*. 105:1102-1109.

Ma, X.J., R. Salunga, J.T. Tuggle, J. Gaudet, E. Enright, P. McQuary, T. Payette, M. Pistone, K. Stecker, B.M. Zhang, Y.X. Zhou, H. Varnholt, B. Smith, M. Gadd, E. Chatfield, J. Kessler, T.M. Baer, M.G. Erlander, and D.C. Sgroi. 2003. Gene expression profiles of human breast cancer progression. *Proceedings of the National Academy of Sciences of the United States of America*. 100:5974-5979.

Mabuchi, I., and M. Okuno. 1977. The effect of myosin antibody on the division of starfish blastomeres. *J Cell Biol*. 74:251-263.

MacLean-Fletcher, S., and T.D. Pollard. 1980. Mechanism of action of cytochalasin B on actin. *Cell*. 20:329-341.

Maeda, J., T. Hirano, A. Ogiwara, S. Akimoto, T. Kawakami, Y. Fukui, T. Oka, Y. Gong, R. Guo, H. Inada, K. Nawa, M. Kojika, Y. Suga, T. Ohira, K. Mukai, and H. Kato. 2008. Proteomic analysis of stage I primary lung adenocarcinoma aimed at individualisation of postoperative therapy. *Br J Cancer*. 98:596-603.

Manley, S., J.M. Gillette, G.H. Patterson, H. Shroff, H.F. Hess, E. Betzig, and J. Lippincott-Schwartz. 2008. High-density mapping of single-molecule trajectories with photoactivated localization microscopy. *Nature methods*. 5:155-157.

Matsumura, F., S. Ono, Y. Yamakita, G. Totsukawa, and S. Yamashiro. 1998. Specific localization of serine 19 phosphorylated myosin II during cell locomotion and mitosis of cultured cells. *The Journal of cell biology*. 140:119-129.

Mayor, R., and S. Etienne-Manneville. 2016. The front and rear of collective cell migration. *Nature reviews. Molecular cell biology*. 17:97-109.

Miller, DM., Ortiz, I., Berliner, GC., Epstein, HF. 1983. Differential localization of two moysins within nematode thick filaments. *Cell*. 34(2):477-90

McKenna, N.M., C.S. Johnson, and Y.L. Wang. 1986. Formation and alignment of Z lines in living chick myotubes microinjected with rhodamine-labeled alpha-actinin. *J Cell Biol*. 103:2163-2171.

McKinney, S.A., C.S. Murphy, K.L. Hazelwood, M.W. Davidson, and L.L. Looger. 2009. A bright and photostable photoconvertible fluorescent protein. *Nature methods*. 6:131-133.

Medeiros, N.A., D.T. Burnette, and P. Forscher. 2006. Myosin II functions in actin-bundle turnover in neuronal growth cones. *Nat Cell Biol*. 8:215-226.

Mioulane, M., G. Foldes, N.N. Ali, M.D. Schneider, and S.E. Harding. 2012. Development of high content imaging methods for cell death detection in human pluripotent stem cell-derived cardiomyocytes. *J Cardiovasc Transl Res*. 5:593-604.

Monte Westerfield, I.o.N., University of Oregon. 2007. A Guide for the Laboratory Use of Zebrafish *Danio (Brachydanio) rerio*. University of Oregon.

Murugesan, S., J. Hong, J. Yi, D. Li, J.R. Beach, L. Shao, J. Meinhardt, G. Madison, X. Wu, E. Betzig, and J.A. Hammer. 2016. Formin-generated actomyosin arcs propel T cell receptor microcluster movement at the immune synapse. *J Cell Biol*. 215:383-399.

Nagy, A., Y. Takagi, N. Billington, S.A. Sun, D.K. Hong, E. Homsher, A. Wang, and J.R. Sellers. 2013. Kinetic characterization of nonmuscle myosin IIb at the single molecule level. *The Journal of biological chemistry*. 288:709-722.

Ng, W.A., I.L. Grupp, A. Subramaniam, and J. Robbins. 1991. Cardiac myosin heavy chain mRNA expression and myocardial function in the mouse heart. *Circulation research*. 68:1742-1750.

Niederman, R., and T.D. Pollard. 1975. Human platelet myosin. II. In vitro assembly and structure of myosin filaments. *The Journal of cell biology*. 67:72-92.

Nolen, B.J., N. Tomasevic, A. Russell, D.W. Pierce, Z. Jia, C.D. McCormick, J. Hartman, R. Sakowicz, and T.D. Pollard. 2009. Characterization of two classes of small molecule inhibitors of Arp2/3 complex. *Nature*. 460:1031-1034.

Norstrom, M.F., P.A. Smithback, and R.S. Rock. 2010. Unconventional processive mechanics of non-muscle myosin IIB. *The Journal of biological chemistry*. 285:26326-26334.

Ong, K., C. Wloka, S. Okada, T. Svitkina, and E. Bi. 2014. Architecture and dynamic remodelling of the septin cytoskeleton during the cell cycle. *Nature communications*. 5:5698.

Ovesny, M., P. Krizek, J. Borkovec, Z. Svindrych, and G.M. Hagen. 2014. ThunderSTORM: a comprehensive ImageJ plug-in for PALM and STORM data analysis and super-resolution imaging. *Bioinformatics*. 30:2389-2390.

Pasqualini, F.S., S.P. Sheehy, A. Agarwal, Y. Aratyn-Schaus, and K.K. Parker. 2015. Structural phenotyping of stem cell-derived cardiomyocytes. *Stem Cell Reports*. 4:340-347.

Paszek, M.J., N. Zahir, K.R. Johnson, J.N. Lakins, G.I. Rozenberg, A. Gefen, C.A. Reinhart-King, S.S. Margulies, M. Dembo, D. Boettiger, D.A. Hammer, and V.M. Weaver. 2005. Tensional homeostasis and the malignant phenotype. *Cancer Cell*. 8:241-254.

Petrie, R.J., and K.M. Yamada. 2012. At the leading edge of three-dimensional cell migration. *Journal of cell science*. 125:5917-5926.

Pollard, T.D. 1975. Electron microscopy of synthetic myosin filaments. Evidence for cross-bridge. Flexibility and copolymer formation. *J Cell Biol*. 67:93-104.

Pollard, T.D. 2007. Regulation of actin filament assembly by Arp2/3 complex and formins. *Annu Rev Biophys Biomol Struct*. 36:451-477.

Pollard, T.D. 2016. Actin and Actin-Binding Proteins. *Cold Spring Harb Perspect Biol*. 8.

Pollard, T.D., and G.G. Borisy. 2003. Cellular motility driven by assembly and disassembly of actin filaments. *Cell*. 112:453-465.

Ponti, A., M. Machacek, S.L. Gupton, C.M. Waterman-Storer, and G. Danuser. 2004. Two distinct actin networks drive the protrusion of migrating cells. *Science*. 305:1782-1786.

Resnicow, D.I., J.C. Deacon, H.M. Warrick, J.A. Spudich, and L.A. Leinwand. 2010. Functional diversity among a family of human skeletal muscle myosin motors. *Proceedings of the National Academy of Sciences of the United States of America*. 107:1053-1058.

Rhee, D., J.M. Sanger, and J.W. Sanger. 1994. The premyofibril: evidence for its role in myofibrillogenesis. *Cell motility and the cytoskeleton*. 28:1-24.

Ribeiro, A.J., Y.S. Ang, J.D. Fu, R.N. Rivas, T.M. Mohamed, G.C. Higgs, D. Srivastava, and B.L. Pruitt. 2015. Contractility of single cardiomyocytes differentiated from pluripotent stem cells depends on physiological shape and substrate stiffness. *Proceedings of the National Academy of Sciences of the United States of America*. 112:12705-12710.

Ricketson, D., C.A. Johnston, and K.E. Prehoda. 2010. Multiple tail domain interactions stabilize nonmuscle myosin II bipolar filaments. *Proceedings of the National Academy of Sciences of the United States of America*. 107:20964-20969.

Riedl, J., A.H. Crevenna, K. Kessenbrock, J.H. Yu, D. Neukirchen, M. Bista, F. Bradke, D. Jenne, T.A. Holak, Z. Werb, M. Sixt, and R. Wedlich-Soldner. 2008. Lifeact: a versatile marker to visualize F-actin. *Nature methods*. 5:605-607.

Rizvi, S.A., E.M. Neidt, J. Cui, Z. Feiger, C.T. Skau, M.L. Gardel, S.A. Kozmin, and D.R. Kovar. 2009. Identification and characterization of a small molecule inhibitor of formin-mediated actin assembly. *Chem Biol*. 16:1158-1168.

Rosado, M., C.F. Barber, C. Berciu, S. Feldman, S.J. Birren, D. Nicastro, and B.L. Goode. 2014. Critical roles for multiple formins during cardiac myofibril development and repair. *Mol Biol Cell*. 25:811-827.

Rossi, A., Z. Kontarakis, C. Gerri, H. Nolte, S. Holper, M. Kruger, and D.Y. Stainier. 2015. Genetic compensation induced by deleterious mutations but not gene knockdowns. *Nature*. 524:230-233.

Rui, Y., J. Bai, and N. Perrimon. 2010. Sarcomere formation occurs by the assembly of multiple latent protein complexes. *PLoS Genet*. 6:e1001208.

Samuel, M.S., J.I. Lopez, E.J. McGhee, D.R. Croft, D. Strachan, P. Timpson, J. Munro, E. Schroder, J. Zhou, V.G. Brunton, N. Barker, H. Clevers, O.J. Sansom, K.I. Anderson, V.M. Weaver, and M.F. Olson. 2011. Actomyosin-mediated cellular tension drives increased tissue stiffness and beta-catenin activation to induce epidermal hyperplasia and tumor growth. *Cancer Cell*. 19:776-791.

Sandquist, J.C., K.I. Swenson, K.A. Demali, K. Burridge, and A.R. Means. 2006. Rho kinase differentially regulates phosphorylation of nonmuscle myosin II isoforms A and B during cell rounding and migration. *The Journal of biological chemistry*. 281:35873-35883.

Sanger, J.M., and J.W. Sanger. 1980. Banding and polarity of actin filaments in interphase and cleaving cells. *The Journal of cell biology*. 86:568-575.

Sanger, J.W., S. Kang, C.C. Siebrands, N. Freeman, A. Du, J. Wang, A.L. Stout, and J.M. Sanger. 2005. How to build a myofibril. *Journal of muscle research and cell motility*. 26:343-354.

Schrank, B.R., T. Aparicio, Y. Li, W. Chang, B.T. Chait, G.G. Gundersen, M.E. Gottesman, and J. Gautier. 2018. Nuclear ARP2/3 drives DNA break clustering for homology-directed repair. *Nature*. 559:61-66.

Sengupta, P., T. Jovanovic-Talisman, D. Skoko, M. Renz, S.L. Veatch, and J. Lippincott-Schwartz. 2011. Probing protein heterogeneity in the plasma membrane using PALM and pair correlation analysis. *Nature methods*. 8:969-975.

Seri, M., R. Cusano, S. Gangarossa, G. Caridi, D. Bordo, C. Lo Nigro, G.M. Ghiggeri, R. Ravazzolo, M. Savino, M. Del Vecchio, M. d'Apolito, A. Iolascon, L.L. Zelante, A. Savoia, C.L. Balduini, P. Noris, U. Magrini, S. Belletti, K.E. Heath, M. Babcock, M.J. Glucksman, E. Aliprandis, N. Bizzaro, R.J. Desnick, and J.A. Martignetti. 2000. Mutations in MYH9 result in the May-Hegglin anomaly, and Fechtner and Sebastian syndromes. The May-Heggllin/Fechtner Syndrome Consortium. *Nature genetics*. 26:103-105.

Shutova, M., C. Yang, J.M. Vasiliev, and T. Svitkina. 2012. Functions of nonmuscle myosin II in assembly of the cellular contractile system. *PLoS One*. 7:e40814.

Shutova, M.S., S.B. Asokan, S. Talwar, R.K. Assoian, J.E. Bear, and T.M. Svitkina. 2017. Self-sorting of nonmuscle myosins IIA and IIB polarizes the cytoskeleton and modulates cell motility. *J Cell Biol*. 216:2877-2889.

Shutova, M.S., W.A. Spessott, C.G. Giraudo, and T. Svitkina. 2014. Endogenous species of mammalian nonmuscle myosin IIA and IIB include activated monomers and heteropolymers. *Current biology : CB*. 24:1958-1968.

Sjoblom, B., A. Salmazo, and K. Djinovic-Carugo. 2008. Alpha-actinin structure and regulation. *Cellular and molecular life sciences : CMLS*. 65:2688-2701.

Small, V.J.R., K.; Kaverina, I.; Anderson, K.I. 1998. Assembling an actin cytoskeleton for cell attachment and movement. *BBA Molecular Cell Research*. 1404:271-281.

Smith, G.F., M.A. Ridler, and J.A. Faunch. 1967. Action of cytochalasin B on cultured human lymphocytes. *Nature*. 216:1134-1135.

Sparrow, J.C., and F. Schock. 2009. The initial steps of myofibril assembly: integrins pave the way. *Nature reviews. Molecular cell biology*. 10:293-298.

Spector, I., N.R. Shochet, Y. Kashman, and A. Groweiss. 1983. Latrunculins: novel marine toxins that disrupt microfilament organization in cultured cells. *Science*. 219:493-495.

Spudich, J.A. 2014. Hypertrophic and dilated cardiomyopathy: four decades of basic research on muscle lead to potential therapeutic approaches to these devastating genetic diseases. *Biophysical journal*. 106:1236-1249.

Stachowiak, M.R., P.M. McCall, T. Thoresen, H.E. Balcioglu, L. Kasiewicz, M.L. Gardel, and B. O'Shaughnessy. 2012. Self-organization of myosin II in reconstituted actomyosin bundles. *Biophysical journal*. 103:1265-1274.

Straight, A.F., A. Cheung, J. Limouze, I. Chen, N.J. Westwood, J.R. Sellers, and T.J. Mitchison. 2003. Dissecting temporal and spatial control of cytokinesis with a myosin II Inhibitor. *Science*. 299:1743-1747.

Svitkina, T.M. 2018. Ultrastructure of the actin cytoskeleton. *Curr Opin Cell Biol*. 54:1-8.

Svitkina, T.M., A.B. Verkhovsky, K.M. McQuade, and G.G. Borisy. 1997. Analysis of the actin-myosin II system in fish epidermal keratocytes: mechanism of cell body translocation. *J Cell Biol*. 139:397-415.

Swaminathan, V., and C.M. Waterman. 2016. The molecular clutch model for mechanotransduction evolves. *Nature cell biology*. 18:459-461.

Szent-Gyorgyi, A. 1943a. The crystallization of myosin and some of its properties and reactions. *Stud. Inst. Med. Chem. Univ. Szeged.* III:76-85.

Szent-Gyorgyi, A. 1943b. Observations on actomyosin. *Stud. Inst. Med. Chem. Univ. Szeged.* III:86-92.

Szent-Gyorgyi, A. 1963. Lost in the Twentieth Century. *Annu Rev Biochem*. 32:1-14.

Takahashi, K., K. Tanabe, M. Ohnuki, M. Narita, T. Ichisaka, K. Tomoda, and S. Yamanaka. 2007. Induction of pluripotent stem cells from adult human fibroblasts by defined factors. *Cell*. 131:861-872.

Taniguchi, K., R. Takeya, S. Suetsugu, O.M. Kan, M. Narusawa, A. Shiose, R. Tominaga, and H. Sumimoto. 2009. Mammalian formin fhod3 regulates actin assembly and sarcomere organization in striated muscles. *The Journal of biological chemistry*. 284:29873-29881.

Tojkander, S., G. Gateva, and P. Lappalainen. 2012. Actin stress fibers--assembly, dynamics and biological roles. *Journal of cell science*. 125:1855-1864.

Tojkander, S., G. Gateva, G. Schevzov, P. Hotulainen, P. Naumanen, C. Martin, P.W. Gunning, and P. Lappalainen. 2011. A molecular pathway for myosin II recruitment to stress fibers. *Current biology : CB*. 21:539-550.

Tullio, A.N., D. Accili, V.J. Ferrans, Z.X. Yu, K. Takeda, A. Grinberg, H. Westphal, Y.A. Preston, and R.S. Adelstein. 1997. Nonmuscle myosin II-B is required for normal development of the mouse heart. *Proceedings of the National Academy of Sciences of the United States of America*. 94:12407-12412.

Tuzovic, L., L. Yu, W. Zeng, X. Li, H. Lu, H.M. Lu, K.D. Gonzalez, and W.K. Chung. 2013. A human de novo mutation in MYH10 phenocopies the loss of function mutation in mice. *Rare Dis*. 1:e26144.

Uehata, M., T. Ishizaki, H. Satoh, T. Ono, T. Kawahara, T. Morishita, H. Tamakawa, K. Yamagami, J. Inui, M. Maekawa, and S. Narumiya. 1997. Calcium sensitization of smooth muscle mediated by a Rho-associated protein kinase in hypertension. *Nature*. 389:990-994.

Vallenius, T. 2013. Actin stress fibre subtypes in mesenchymal-migrating cells. *Open Biol*. 3:130001.

Vasquez, C.G., M. Tworoger, and A.C. Martin. 2014. Dynamic myosin phosphorylation regulates contractile pulses and tissue integrity during epithelial morphogenesis. *The Journal of cell biology*. 206:435-450.

Vassilev, L.T., C. Tovar, S. Chen, D. Knezevic, X. Zhao, H. Sun, D.C. Heimbrook, and L. Chen. 2006. Selective small-molecule inhibitor reveals critical mitotic functions of human CDK1. *Proceedings of the National Academy of Sciences of the United States of America*. 103:10660-10665.

Verkhovsky, A.B., and G.G. Borisy. 1993. Non-sarcomeric mode of myosin II organization in the fibroblast lamellum. *J Cell Biol*. 123:637-652.

Verkhovsky, A.B., T.M. Svitkina, and G.G. Borisy. 1995. Myosin II filament assemblies in the active lamella of fibroblasts: their morphogenesis and role in the formation of actin filament bundles. *J Cell Biol*. 131:989-1002.

Verkhovsky, A.B., T.M. Svitkina, and G.G. Borisy. 1999a. Network contraction model for cell translocation and retrograde flow. *Biochem Soc Symp*. 65:207-222.

Verkhovsky, A.B., T.M. Svitkina, and G.G. Borisy. 1999b. Network contraction model for cell translocation and retrograde flow. *Biochem Soc Symp*. 65:207-222.

Vicente-Manzanares, M., X. Ma, R.S. Adelstein, and A.R. Horwitz. 2009a. Non-muscle myosin II takes centre stage in cell adhesion and migration. *Nat Rev Mol Cell Biol*. 10:778-790.

Vicente-Manzanares, M., X. Ma, R.S. Adelstein, and A.R. Horwitz. 2009b. Non-muscle myosin II takes centre stage in cell adhesion and migration. *Nature reviews. Molecular cell biology*. 10:778-790.

Vicente-Manzanares, M., J. Zareno, L. Whitmore, C.K. Choi, and A.F. Horwitz. 2007. Regulation of protrusion, adhesion dynamics, and polarity by myosins IIA and IIB in migrating cells. *J Cell Biol*. 176:573-580.

Wakatsuki, T., B. Schwab, N.C. Thompson, and E.L. Elson. 2001. Effects of cytochalasin D and latrunculin B on mechanical properties of cells. *Journal of cell science*. 114:1025-1036.

Wang, Y.L. 2005. The mechanism of cortical ingression during early cytokinesis: thinking beyond the contractile ring hypothesis. *Trends in cell biology*. 15:581-588.

Watkins, H., H. Ashrafian, and C. Redwood. 2011. Inherited cardiomyopathies. *The New England journal of medicine*. 364:1643-1656.

Wiedenmann, J., S. Ivanchenko, F. Oswald, F. Schmitt, C. Rocker, A. Salih, K.D. Spindler, and G.U. Nienhaus. 2004. EosFP, a fluorescent marker protein with UV-inducible green-to-red fluorescence conversion. *Proceedings of the National Academy of Sciences of the United States of America*. 101:15905-15910.

Wilson, C.A., M.A. Tsuchida, G.M. Allen, E.L. Barnhart, K.T. Applegate, P.T. Yam, L. Ji, K. Keren, G. Danuser, and J.A. Theriot. 2010. Myosin II contributes to cell-scale actin network treadmilling through network disassembly. *Nature*. 465:373-377.

Xia, Z.K., Y.C. Yuan, N. Yin, B.L. Yin, Z.P. Tan, and Y.R. Hu. 2012. Nonmuscle myosin IIA is associated with poor prognosis of esophageal squamous cancer. *Dis Esophagus*. 25:427-436.

Xu, K., H.P. Babcock, and X. Zhuang. 2012. Dual-objective STORM reveals three-dimensional filament organization in the actin cytoskeleton. *Nature methods*. 9:185-188.

Yamauchi-Takihara, K., M.J. Sole, J. Liew, D. Ing, and C.C. Liew. 1989. Characterization of human cardiac myosin heavy chain genes. *Proceedings of the National Academy of Sciences of the United States of America*. 86:3504-3508.